

**MICROSTRUCTURAL EVOLUTION IN NiO-MgO: LINKING
EQUILIBRIUM CRYSTAL SHAPE AND GRAIN GROWTH**

by

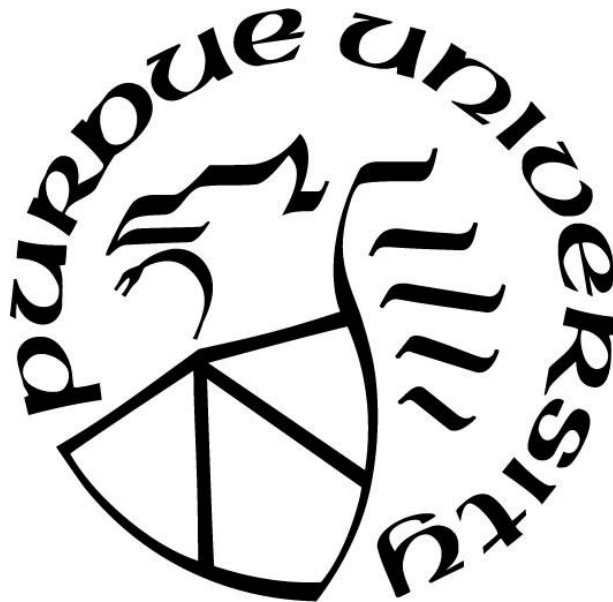
David A. Lowing

A Dissertation

Submitted to the Faculty of Purdue University

In Partial Fulfillment of the Requirements for the degree of

Doctor of Philosophy



School of Materials Engineering

West Lafayette, Indiana

December 2018

**THE PURDUE UNIVERSITY GRADUATE SCHOOL
STATEMENT OF COMMITTEE APPROVAL**

Dr. John Blendell, Chair

Department of Materials Engineering

Dr. Wolfgang Rheinheimer

Department of Materials Engineering

Dr. Eric Kvam

Department of Materials Engineering

Dr. Rodney Trice

Department of Materials Engineering

Approved by:

Dr. David Bahr

Head of the Graduate Program

To my ghost, may you find peace in life.

ACKNOWLEDGMENTS

I wish to acknowledge my family, friends, research group members, and advisor/mentor for all the support they have provided over the last five years. Your support made this possible.

TABLE OF CONTENTS

LIST OF TABLES	8
LIST OF FIGURES	9
ABSTRACT	15
1. INTRODUCTION	18
1.1 Ceramics Past and Future Development	18
1.2 Fundamentals of Ceramic Processing and Characterization	20
1.2.1 Ceramic Processing, Microstructure-Property-Processing Relationship	20
1.2.2 Ceramic Raw Materials and Precursor Powders	20
1.2.2.1 Natural Raw Materials	20
1.2.2.2 Synthetic Raw Materials	21
1.2.3 Ceramic Forming	22
1.2.3.1 Dry Forming Techniques	22
1.2.3.2 Wet Forming Techniques	24
1.2.4 Ceramic Firing and Sintering	26
1.2.4.1 Sintering Driving Force and Basic Phenomena	26
1.2.4.2 Three Stages of Sintering and the Two Particle Model	29
1.2.4.3 Sintering Variables	33
1.2.5 Ceramic Microstructure Characterization	34
1.2.5.1 Grain Growth: Normal and Abnormal	34
1.2.5.2 Role of Grain Boundary in Grain Growth	36
1.3 Classical Isotropic Grain Boundary Structure and Migration	36
1.3.1 Grain Boundary Formation and Structure	36
1.3.2 Isotropic Grain Boundary Migration	39
1.3.3 Grain Boundary Drag Forces	40
1.3.3.1 Solute Drag	40
1.3.3.2 Smith-Zener Particle Pinning and Pore Drag	44
1.4 Grain Boundary Energy Anisotropy	48
1.4.1 Anisotropic Grain Boundary Structure and Migration	48
1.4.2 Linking Equilibrium Crystal Shape to Grain Growth Via Grain Boundaries	51

1.4.2.1	Wulff Shape and Equilibrium Crystal Shape	51
1.4.2.2	The Grain Boundary Plane Distribution	55
1.4.2.3	The Hypothesis: Linking the Equilibrium Crystal Shape to Grain Growth	59
1.5	The NiO-MgO System	59
1.5.1	Equilibrium Crystal Shape of NiO-MgO Alloys	60
1.5.2	Other Characteristics of NiO-MgO System	62
2.	NiO-MgO POWDER PRODUCTION AND CHARACTERIZATION	64
2.1	Introduction	64
2.2	Mechanical Alloying	64
2.2.1	NiO-MgO Mechanical Alloying Process	64
2.2.2	Mechanical Alloyed Powder Characterization	67
2.2.2.1	Mechanical Alloyed Powder Compositional Homogeneity	67
2.2.2.2	Mechanical Alloyed Powder Impurity Level Characterization	68
2.3	Amorphous Citrate Chemical Production	68
2.3.1	Amorphous Citrate Production Process	68
2.3.2	Amorphous Citrate Powder Characterization	69
2.3.2.1	Compositional Homogeneity	70
2.3.2.2	Particle size and Morphology	71
2.4	Powder Morphology and Size Distribution Alteration	73
2.5	Final Comments on NiO-MgO Powder Production	74
3.	SINTERING AND DENSIFICATION OF NiO-MgO ALLOYS	75
3.1	Introduction	75
3.2	Ceramic Powder Formation	75
3.3	Sintering and Densification	77
3.3.1	Conventional Sintering	77
3.3.1.1	Conventional Sintering Optimization	78
3.3.1.2	Investigation of Particle Size and Morphology	80
3.3.2	Spark Plasma Sintering	80
3.4	Hot Pressing	83
3.5	Final Comments on Sintering and Densification of NiO-MgO Powders	86
4.	GRAIN GROWTH	88

4.1	Introduction.....	88
4.2	Experimental.....	91
4.2.1	NiO:MgO Alloy Production	91
4.2.2	Characterization.....	91
4.3	Results.....	91
4.3.1	Base Powder Characterization.....	91
4.3.2	Grain Growth Agglomerate Selection	93
4.3.3	Grain Growth.....	95
4.4	Discussion.....	97
4.4.1	Isolating the Effect of Changing Surface Anisotropy.....	98
4.5	Conclusion	99
5.	LINKING SURFACE MICROSTRUCTURE AND EQUILIBRIUM CRYSTAL SHAPE WITH EBSD AND AFM.....	100
5.1	Equilibrium Crystal Shapes and N-Diagrams.....	100
5.2	Electron Back Scatter Diffraction and Atomic Force Microscopy Analysis	103
5.3	Surface Faceting Behavior Characterization Preliminary Work	105
5.4	Final Comments and Future Work.....	110
	APPENDIX A: EBSD-AFM SURFACE FACETING MICROSTRUCTURE ANALYSIS SCRIPT.....	112
	APPENDIX B: NiO-MgO PROCESSING DATA.....	119
	REFERENCES	123

LIST OF TABLES

Table 1-1: Diffusion Mechanism and Pathways During Sintering [50]	31
Table 2-1: Calculated Scherrer Crystallite Size.....	72
Table 3-1: NiO-MgO Calculated Theoretical Density.....	78
Table 4-1: Calculated Scherrer Crystallite Size.....	93
Table 4-2: Grain Growth Rates for NiO-MgO Alloys.....	96

LIST OF FIGURES

Figure 1-1: Material science paradigm tetrahedron, structure-processing-property-performance relationship demonstrating the interconnectedness of material science and engineering[10].	20
Figure 1-2: Dry pressing process schematic, showing compaction profile for single-ended dies and double-ended dies. The pressure is greater closer to the plungers and reduces with distance. [20]	22
Figure 1-3: Ceramic injection molding schematic showing the process steps. Complex shapes can be formed using injection molding with sufficiently fluid powder mixtures and a uniform pressure application. [22]	23
Figure 1-4: Schematic overview of slip casting process. Micro-porous mold is filled with ceramic slurry, liquid is absorbed into porous mold coating the mold with ceramic powders. Excess liquid is removed from the mold leaving the cast part of the perimeter of the mold. [23]	24
Figure 1-5: Schematic diagram showing overview of tape casting process. Ceramic slurry is spread across a substrate, while excess slurry is scraped away by a doctor blade, setting the desired height. Slurry layer is dried forming a ceramic green body sheet. [25]	25
Figure 1-6: Schematic overview of ceramic extrusion processing apparatus. Ceramic powder mixed with polymer pellets are added to the hopper. Powder mixture is heated, forming a paste and extruded through a die by a screw forming the desired green body ceramic. [27]	26
Figure 1-7: Schematic showing densification and coarsening of circular particles. Densification occurs via solid-vapor interfaces becoming solid-solid interfaces. Coarsening occurs with some particles growing at the expense of other reducing in number[28].	27
Figure 1-8: Schematic of a solid-vapor interface showing the migration path of atoms and vacancies driving by pressure differences in region I and II resulting from curvature. [28]	28
Figure 1-9: Graph of relative density as a function of sintering time showing increasing density with time broken into the three stages of sintering. [28]	29

Figure 1-10: Diagram of simple two particle model (a) showing coarsening with neck formation and growth from surface atoms (b) showing densification with neck formation and growth from grain boundary atoms moving the two particles closer. [28]	30
Figure 1-11: Diagram of the two-particle model showing mass transport pathways described in Table 1-1. [28]	31
Figure 1-12: Schematic showing (a) network of connected pores during intermediate sintering stage and (b) isolated pores formed shrunk during the final stage of sintering. [28]	32
Figure 1-13: Schematic showing the formation of isolated pores and shrinkage during final stage sintering until an equilibrium pressure is reached. [28]	33
Figure 1-14: Optical images of AISI 304L stainless steel showing normal and abnormal grain growth microstructures that develop at different annealing times at 900°C. Corresponding grain size distributions are shown. [39]	35
Figure 1-15: Schematic showing the structure of tilt (a) and twist (b) boundaries. Tilt boundaries are rotated parallel to the grain boundary and twist are rotated perpendicular to the grain boundary[42].	37
Figure 1-16: Schematic showing Read and Shockley dislocation model for grain boundaries where misorientations corresponds to dislocations. [44]	38
Figure 1-17: Schematic showing (a) Σ 25 at 16" rotation, (b) Σ 13 at 22" rotation, (c) Σ 17 at 28" rotation, and (d) Σ 5 at 36" rotation. The black boxes show the repeating CSL cell for each Σ boundary. [44]	39
Figure 1-18: Graph showing attractive solute concentration profiles at increasing velocities from a-e. [48]	42
Figure 1-19: Graph showing repelled solute concentration profiles at increasing velocities from a-c [48]	43
Figure 1-20: Graphs showing the driving force as a function of velocity for (a) intrinsic drag, (b) solute drag, (c) total drag. [48]	44
Figure 1-21: Schematic showing particle-grain boundary attachment. Theta increases as boundary moves away from the particle leading to an eventual break away event. [50]	45
Figure 1-22: Schematic of pore attached to a grain boundary. Diffusion pathways are indicated along the surface and across the pore tracing allowing the pore to move. [50]	46

Figure 1-23: : Schematic of pore shape as a function of grain boundary velocity increasing from a-d. Increasing velocity increases the lag of the trailing edge of the pore distending the pore. [50]	47
Figure 1-24: Schematic showing increasing grain boundary curvature near pore interface increasing boundary energy eventually leading to break away. [50]	48
Figure 1-25: Schematic showing a faceted grain boundary conforming to macroscopic curvature and step nucleation and growth resulting in grain boundary migration. [51]	49
Figure 1-26: Graph of grain boundary energy as a function of misorientation for copper for the (100) and (111). [44]	50
Figure 1-27: Images showing SrTiO ₃ single crystals growing into polycrystals. Single crystal interfaces of {100}, {110}, {111} and {310} annealed for 6 minutes and 115 hours. Grain boundary structure changes with single crystal orientation showing both faceted and non-faceted grain boundaries[53].	51
Figure 1-28: Schematic of (a) Wulff construction and (b) Wulff shape or equilibrium crystal shape[55].	52
Figure 1-29: Schematic for elongated equilibrium crystal shape of aluminum sample showing unstable orientations devolving into stable boundary orientations[55].....	53
Figure 1-30: Schematic showing (a-b) first order transitions between faceted and rough regions resulting in missing orientations and (c) a second order transition between facet and rough regions with no missing orientations[54]......	54
Figure 1-31: Schematic showing increasing rough surface area of an equilibrium crystal shape with increasing temperature for two equilibrium shapes[56]......	54
Figure 1-32: Schematic showing grain boundary trace segment formation until tolerance is complete[59]......	56
Figure 1-33: Schematic showing (a) grain boundary trace, (b) possible orientations of the grain boundary of a single trace and (c) grain boundary trace and possible grain boundary orientations plotted on a stereographic projects[59].	57
Figure 1-34: Schematic demonstrating the identification of the grain boundary orientation by the accumulation of trace orientations intersecting at a single orientation[59]......	57
Figure 1-35: Inverse pole figures for Ni showing the grain boundary plane distribution and grain boundary energy distribution having an inverse relationship. [57]	58

Figure 1-36: Pole figures for MgO showing surface energy and grain boundary energy distribution having an inverse relationship [58].....	58
Figure 1-37: Schematic of equilibrium crystal shape of NiO-MgO alloys (a) in 3D, (b) cross section along (100) axis and (c) (110) axis. [60].....	61
Figure 1-38: Schematic showing NiO-MgO 3D equilibrium crystal shapes extrapolated from SEM images. Recreated from[60].	61
Figure 1-39: Phase diagram for NiO-MgO system. [60].....	62
Figure 2-1: Schematic drawing showing powder welding and fracturing experienced during mechanical alloying. The schematic shows a powder mixture of two distinct chemical compositions [62].....	65
Figure 2-2: Graphical figure showing particle size increases initially during mechanically alloying as small particles weld together. As particles continue to grow and shear forces increase, they will reach a critical mass a fracture. During mechanical milling as, small particles weld and grow, large particles fracture and a stable intermediate particle size is reached. [62]	66
Figure 2-3: Images taken of powder before (left) and after (right) 1000°C step showing the color transition from black to green with the restoration of oxygen in the powder to stoichiometric levels.....	70
Figure 2-4: X-ray diffraction patterns (a) five compositions of NiO-MgO with Ni to Mg ratios of 100:0, 75:25, 50:50, 25:75, 0:100, (b) (220) peak highlighting formation of distinct peaks for each alloy, ranging from pure NiO to pure MgO, following a linear extrapolation of the peak position.	71
Figure 2-5: SEM micrograph of particle plate like morphology large agglomerate forming from amorphous citrate process with sizes greater than 300µms in a 75:25 Ni:Mg powder.	72
Figure 2-6: Sem micrographs of multigrain, multilayer agglomerate structures resulting from amorphous citrate process in a) 75:25 Ni:Mg powder, b) 50:50 Ni:Mg powder.	73
Figure 3-1:Relative density and open porosity as a function of time for 75:25 Ni:Mg powder. Relative density increases over time where open porosity, inversely, decreases.....	79
Figure 3-2: SEM micrographs for a) 75:25, b) 50:50 and c) 25:75 Ni:Mg powders. All micrographs show extensive inter- and intra-granular porosity.	80

- Figure 3-3: Diagram of spark plasma sintering apparatus. Powder is inserted into a double-ended die in a vacuum chamber and pressed with hydraulic rams. Resistive heating occurs by the application of an DC current through the die and powder[76]..... 81
- Figure 3-4: Diagram of spark plasma sintering double-ended die. Powder is compressed in the die between two plungers while a DC electric current is applied shown in the diagram as light blue arrows. Resistive heating heats the powder and die[76]..... 82
- Figure 3-5: SEM micrographs of a) oxygen-depleted and b) oxygen-rich regions of a 50:50 Ni:Mg spark plasma sintered sample. Oxygen depleted and oxygen rich regions showing distinct microstructures after thermal etching at 1150°C. Oxygen depleted regions showing significant surface roughening by comparison. 83
- Figure 3-6: Diagram of a general hot press double-ended die. Uniaxial pressure is applied through plungers while the die is heated by the surrounding furnace under vacuum[76]..... 84
- Figure 3-7: Diagram of graphite double-ended die used. Powder is packed in graphite foil to prevent die contamination. Graphite foil is inserted at the top and bottom to align the plunger rods with the furnace hydraulic rods of the furnace reducing risk of fracture. 84
- Figure 3-8: SEM micrograph of hot pressed 50:50 Ni:Mg powder. Microstructure exhibits minimal porosity appearing fully dense. Small impurities are observed at grain boundaries showing evidence of some pinning with changing boundary curvature. 86
- Figure 3-9: Schematic cross section of a NiO-MgO sample showing the reduction of the outer shell occurring first with the development of Pure Ni particles. The extent of the reduced section will expand with time in a reducing atmosphere[71]. 86
- Figure 4-1: X-ray diffraction patterns (a) five compositions of NiO-MgO, (b) (220) peak highlighting formation of distinct peaks for each alloy ranging from pure NiO to pure MgO..... 92
- Figure 4-2: SEM micrograph of large agglomerates forming from amorphous citrate process with sizes greater than 100µms. 94
- Figure 4-3: Sem micrograph of multigrain, multilayer agglomerate structures resulting from amorphous citrate process 94

Figure 4-4: Temperature dependence of average grain size after zero hours annealing at temperatures from 1000°C to 1500°C.....	95
Figure 4-5: Dependence of average grain size on time held at 1500°C from 1-100 hours	96
Figure 4-6: SEM micrographs of 75:25 NiO:MgO samples at (a) 750°C (b) 1000°C (c) 1250°C (d) 1500°C. Average grain size increased with increasing temperature	97
Figure 5-1: Four simple crystal shapes ranging from a cube to a octahedron with corresponding n-diagrams with sharp edges, showing how simple n-diagrams contain information which can be used to construct the equilibrium crystal shapes of materials. Recreated from[54].....	101
Figure 5-2: SEM images of low (a) and high (b) nickel content samples with corresponding equilibrium crystal shape determined from the image. N-diagrams for each equilibrium crystal shape is shown in (c) for low nickel concentrations and (d) for high concentrations[54].	103
Figure 5-3: Stereographic projections for the upper and lower hemisphere for the rock salt crystal structure highlighting the position of the suspected stable facets in NiO-MgO the{111}, {100} and {110}.....	105
Figure 5-4: Stereographic projection for NiO-MgO showing the symmetry of the rock salt structure for {111}, {100} and {110} having three-fold symmetry, four-fold symmetry and two-fold symmetry respectively.	106
Figure 5-5: Inverse pole figures showing a randomly selected grain's orientation when view from the x, y, z laboratory axis frame of reference.	107
Figure 5-6: Scatter and contour plots showing the local crystallographic topography with an overlay of the stereographic projection. The plots show the formation of a single peak with an orientation closely corresponding to that of the grain measured with EBSD.....	108
Figure 5-7: Inverse pole figures showing a randomly selected grain's orientation when view from the x, y, z laboratory axis frame of reference.	109
Figure 5-8: Scatter and contour plots showing the local crystallographic topography with an overlay of the stereographic projection. The plots show the formation of a single peak with an orientation closely corresponding to that of the grain measured with EBSD.....	110

ABSTRACT

Author: Lowing, David, A. PhD

Institution: Purdue University

Degree Received: December 2018

Title: Microstructural Evolution in NiO-MgO: Linking Equilibrium Crystal Shape and Grain Growth

Committee Chair: John Blendell

Ceramic materials are natural or synthetic, inorganic, non-metallic materials incorporating ionic and covalent bonding. Most ceramics in use are polycrystalline materials where grains are connected by a network of solid-solid interfaces called grain boundaries. The structure of the grain boundaries and their arrangement play a key role in determining materials properties. Developing a fundamental understanding of the formation, structure, migration and methods of control grain boundaries have drawn the interest of scientists for over a century.

While grain boundaries were initially treated as isotropic, advances in materials science has expanded to include energetically anisotropic boundaries. The orientation and structure of a grain boundary, determined by this anisotropy, controls the mobility of a grain boundary. The mobility is the controlling factor during grain growth impacting the microstructural evolution of a material.

This thesis covers fundamental research to model how a materials' equilibrium crystal shape can be used as a grain growth control mechanism. First an overview of ceramic processing and microstructural development is presented with a focus on the role of grain boundaries in determining the properties of a material. The role of anisotropy and related recent work is highlighted setting the foundation for the link between the equilibrium crystal shape and grain growth. A discussion on the selection of the NiO-MgO system for all experimental work is included.

A novel production and processing route for NiO-MgO was developed. Mechanical alloying and milling resulted in significant impurity contamination therefore a chemical production route was used. A modified amorphous citrate process was developed where metal salts containing Ni and Mg were mixed with a polyfunctional organic acid. Rapid dehydration

and calcination at 500°C resulted in chemically homogeneous powders. The amorphous citrate production route produced powder with crystallites ranging from 244-393 nm and agglomerates ranging from 20-300 µm with plate-like morphology.

NiO-MgO powders produced via the amorphous citrate method were sintered using various techniques. Conventional sintering was unable to produce fully dense samples peaking with relative densities from 95-96%. The introduction of pressure through spark plasma sintering and hot pressing improved the relative sample density to 97-100%. It was discovered that exposure to the vacuum required for spark plasma sintering and hot pressing resulted in the reduction of NiO. Spark plasma sintering created oxygen depleted regions and hot pressing further reduced NiO to pure nickel metal which precipitated out at the grain boundaries.

Due to the poor sintering behavior of NiO-MgO grain growth experiments were carried out on the large agglomerates formed during the amorphous citrate process. Agglomerates with more than 50 grains with a thickness of at least 1 µm were selected. Grain growth was measured across five compositions with Ni:Mg ratios of 100:0, 75:25, 50:50, 25:75, 0:100. The average grain size and growth rate increased with increasing nickel content with a significant jump between 50% and 75%. Increasing nickel content was also observed to correspond with a higher number of grains exhibiting surface faceting.

The NiO-MgO equilibrium crystal shape as a function of composition was measured previously. To make the equilibrium crystal shape a more viable control for grain growth a quantitative microstructural characterization technique was developed to measure a materials equilibrium crystal shape. Topographic surface information (surface facets measured by atomic force microscopy, AFM) and grain crystallographic orientation (measured by electron back-scattered diffraction, EBSD) were combined to produce the crystallographic topography of a sample surface. Surface crystallographic topography was used to identify the faceting behavior of grains with a range of orientations. Using the combined data, facet stability maps (n-diagrams) for NiO-MgO were developed.

Controlling grain growth via the equilibrium crystal shape offers the potential to produce microstructures with a high frequency of desirable grain boundaries (grain boundary engineering) and therefore properties. The combination of using AFM and EBSD to create crystallographic topographical surface data and n-diagrams has been demonstrated. N-diagrams for most materials

do not exist, but the technique used here can be applied to a wide range of materials and will expand the ability to control microstructures of ceramic materials.

1. INTRODUCTION

This thesis document contains a review of the literature relating to the understanding of the link between the equilibrium crystal shape and grain growth in ceramic materials as well as contributing original content. Chapter 1 discusses the body of literature involving the structure-property relationship in ceramics as well as key concepts in ceramic processing and microstructure evolution highlighting deficiencies in our current understanding. Opportunities to investigate the link between the equilibrium crystal shape and grain growth are discussed. Chapter 2 discusses original work producing ideal NiO-MgO alloy ceramic precursor powders. Mechanical alloying and amorphous citrate production routes are compared and resulting powders characterized. Precursor powder post production alteration through mechanical milling is discussed as well. Chapter 3 discusses original work optimizing sintering and densification of NiO-MgO powder to achieve fully dense samples. Literature of Competing sintering techniques and sintering process variables is covered. Experimental work sintering NiO-MgO alloy compacts is reported along with characterization of final samples. Chapter 4 discusses original work measuring grain growth in the NiO-MgO alloy system. Using the information framework from chapter 1, powders produced in chapter 2 and samples produced in chapter 3 the effect of a changing equilibrium shape on grain growth is investigated. The implications of the experimental work on linking the equilibrium crystal shape to grain growth is discussed. Chapter 5 discusses original work in developing a novel characterization method to measure the equilibrium crystal shape from the materials surface microstructure. Work combining AFM topological and EBSD crystallographic data to create n-diagrams is presented. The preliminary viability of the characterization method and future work is discussed.

1.1 Ceramics Past and Future Development

Ceramic materials are natural or synthetic, inorganic, non-metallic materials incorporating ionic and covalent bonding [1]. Ceramics come in crystalline forms such as oxides or carbides and in non-crystalline or amorphous forms like glass. Ceramics are well known for their positive properties such as high melting points, hardness, reasonable chemical stability and

low thermal expansion. Ceramics are also known for their characteristic weakness being brittle [2].

Ceramics share a long history with humanity with the oldest documented ceramic statue the Venus of Dolní Věstonice being dated around 28,000 BCE in the late Paleolithic period [3]. Simple ceramic pottery was developed between 18,000-17,000 BCE and spread rapidly with the development of agriculture-based societies [4]. Early pottery was commonly used to store water and food only later becoming adorned with paintings. The first glass objects were discovered around 3,500 BCE in Mesopotamia with glassware factories operating in Egypt around 1,500 BCE [5]. The advancement of kiln technology saw the development of porcelain by the Chinese around 600 CE which spread to Europe during the middle ages by way of the Silk Road [6]. The development of blast furnace and refractory materials in the 16th century ushered in the industrial revolution [7].

The era of modern ceramics or technical ceramics arrived with the introduction of the porcelain electrical insulators in the 1850's [8]. World War II saw significant innovations in ceramic processing and characterization techniques. Post-World War II new ceramics were now being produced with tailored properties enabling entry into new fields such as electronics, medical, automotive and space exploration. Most recently nanotechnology and processing has enabled the production of novel ceramic materials such as transparent and ductile ceramics [9].

History has shown that the development of new ceramic materials and novel properties to meet new performance needs comes from a fundamental understanding of ceramics. Material science has a commonly referred to paradigm called the structure-processing-property-performance tetrahedron, Figure 1-1. This paradigm represents the interdependence of multiple facets of material science and engineering. It is well established in ceramic literature that the properties of a material are dependent on the materials microstructure and processing. The microstructure in turn is dependent on the processing the material has undergone and resulting microstructural evolution altering its structure. The processing is selected to create the properties to produce the desired performance from the materials structure. Understanding these fundamental structure-processing-property-performance relationships in ceramics are critical to the continued development and innovation of modern technical ceramics.

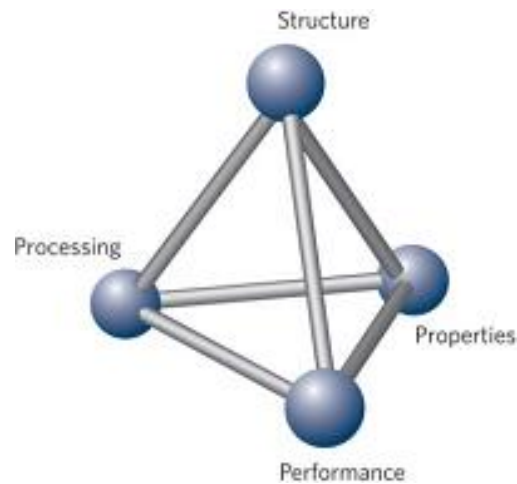


Figure 1-1: Material science paradigm tetrahedron, structure-processing-property-performance relationship demonstrating the interconnectedness of material science and engineering[10].

1.2 Fundamentals of Ceramic Processing and Characterization

1.2.1 Ceramic Processing, Microstructure-Property-Processing Relationship

As discussed previously ceramic properties result from their ionic and covalent bonding as well as their microstructure formed during processing. Material science literature contains numerous studies linking the microstructure of a material to that of its properties. For example, the mechanical properties of a material are strongly dependent on the grain size of a material. Decreasing grain size will increase a materials hardness, tensile strength and impact strength up to a limit[2]. Grain boundaries are well known to pin defects within materials [11], inhibit crack growth [11] and induce directional anisotropy in electrical properties [12]. It has also been observed that different grain boundaries have different resistances to corrosion [13]. Tailoring a materials microstructure to obtain specific properties therefore, requires careful control of the materials microstructure through raw material selection, shape forming and sintering.

1.2.2 Ceramic Raw Materials and Precursor Powders

1.2.2.1 Natural Raw Materials

Natural raw materials and minerals used in the production of ceramics characteristically undergoing minimal processing and purification steps [14]. The materials are excavated from deposits, formed, and fired. This subset of ceramic raw materials is commonly used to produce traditional ceramics such as refractories, cement, glass, pottery and porcelain. Each of the natural

materials has grades based upon the chemistry of the deposit where it was extracted. Small chemical changes across grades result in ceramic products made from the same raw material but with a range of properties. Ceramics produced from raw materials take on many aspects of the raw material such as impurities and are greatly influence by powder characteristics such as particle size and morphology which is not changed with processing [15].

Natural raw materials for ceramic production commonly take on the form of clays. Fire clay is selected for high temperature applications such as fire bricks and refractory materials. Fire clay with a general composition of $\text{Al}_2\text{O}_3 \cdot 2\text{SiO}_2 \cdot 2\text{H}_2\text{O}$ can withstand temperatures in excess of 1700°C [16]. Kaolinite or china clay is a layered silicate with a general composition of $\text{Al}_2\text{Si}_2\text{O}_5(\text{OH})_4$. Kaolinite is used to produce porcelain, and more generally is used to form glosses on paper and in paint glazes [17]. Ball clay is a kaolinitic sediment including kaolinite, mica and quartz [18]. Ball clay is used to produce high quality white ceramics. It is a common choice for artistic pottery as well as floor and wall tiles in houses.

1.2.2.2 Synthetic Raw Materials

Synthetic ceramic raw materials are characterized by the process of extracting the desired components out of natural materials prior to producing ceramics [14]. Synthetic raw materials are combined to meet the desired chemistry for the ceramic then formed and fired. Synthetic raw materials are commonly used in the formation of fine or technical ceramics which are used in electronics, medical, automotive, aerospace and space exploration industries. Ceramics produced from synthetic raw materials have great compositional flexibility giving the ability to tailor the resulting microstructure and properties of the ceramic produced. Synthetic raw materials offer better property control over raw materials [15] as they are produced and not subject compositional gradients in deposits like natural raw materials. Synthetic raw materials often undergo powder processing to alter particulate characteristics such as particle size and geometry prior to forming and sintering. This minimizes the negative effects of powder characteristics from raw materials later in processing. Common synthetic raw materials include: alumina, carbides, nitrides and borides.

1.2.3 Ceramic Forming

1.2.3.1 Dry Forming Techniques

Ceramic forming techniques that operate in the absence of a liquid are known as dry forming techniques. Dry pressing or dry compaction is a simple process where ceramic powder is poured into a die and pressure is applied via a plunger rod [19]. The pressure is applied in a uniaxial direction from either the one end of the die or both ends of the die. The powder compaction profile during the application of pressure is dependent upon the geometry of the die and the application of the pressure. Figure 1-2 illustrates the changing packing profile of a ceramic powder for a single-ended die and double-ended die. The grey scale indicates the packing density of the powder with dark grey being the most compact. In a single-ended die the pressure is applied only from one side causing the powder nearest to the plunger to compact first and as more pressure is applied the compacted region expands into the die. Double-ended dies apply pressure from both ends of the die. This results in the ceramic powder being compacted in the region around both plungers simultaneously and as pressure is applied the high compaction regions grow toward each other.

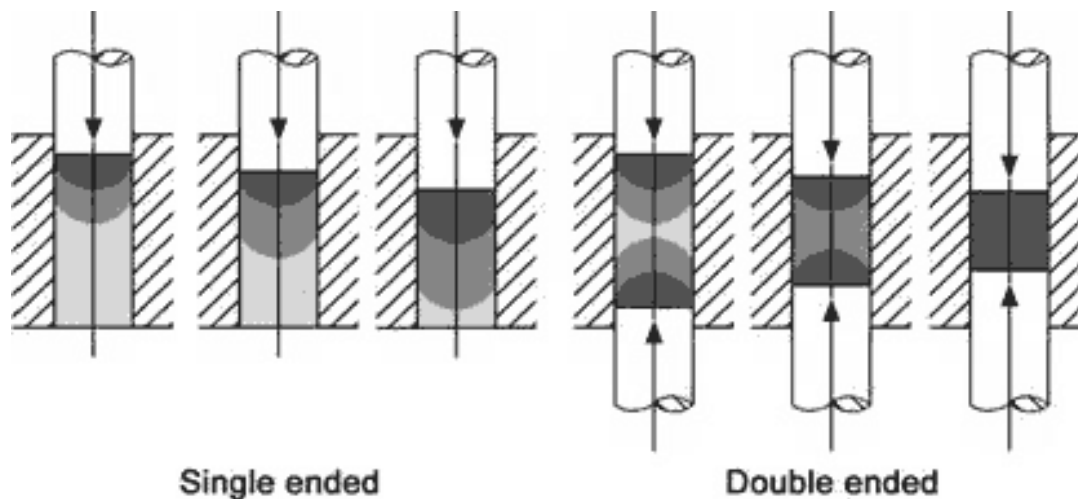


Figure 1-2: Dry pressing process schematic, showing compaction profile for single-ended dies and double-ended dies. The pressure is greater closer to the plungers and reduces with distance. [20]

Dry pressing and compaction are a commonly used process large batches due to cost. The process is quick, and good at making large quantities; however, the dies are expensive and wear over time, lowering shape accuracy. The dry pressing process is very susceptible to the geometry

of the part being formed and mostly used for low complexity small shapes. The effectiveness of dry pressing is strongly related to the distance from the plunger [19]. The effective pressure applied by a plunger decreases with distance from the plunger. Therefore, the thickness of the desired part is limited, or the density profile may be layered, with regions of different densities in the green body. Density strata are undesirable as they can lead to imperfections during sintering.

Dry formation of more complex shapes and high tolerances are commonly produced using powder injection molding. Ceramic powders are mixed with additives such as binders and plasticizers to increase the fluidity of the powder allowing it to flow into the die [21]. The powder is heated and injected into a die cavity under pressure and cooled resulting in the formation of a green body ceramic [21], Figure 1-3. While injection molding offers the ability to form complex shapes it is unable to make large shapes effectively.

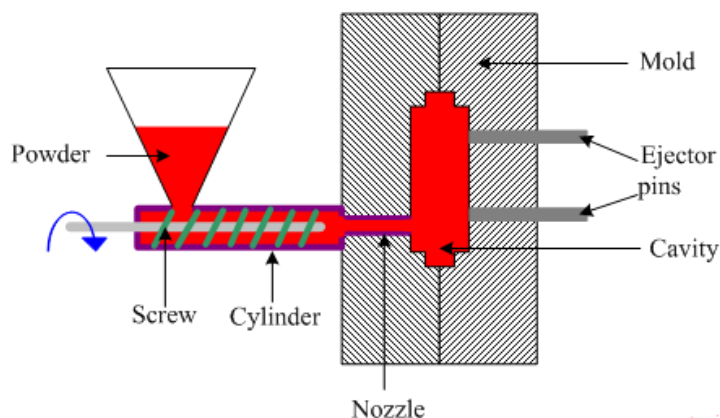


Figure 1-3: Ceramic injection molding schematic showing the process steps. Complex shapes can be formed using injection molding with sufficiently fluid powder mixtures and a uniform pressure application. [22]

Dry pressing processing techniques offer the advantages of being simple processes able to make large batches of product quickly. Dry processing is limited to somewhat simple shapes, otherwise non-uniform green body densities will occur due to uneven pressure. A characteristic of dry pressing techniques is the effect of raw material properties. Any impurities in the powder will be passed on to the green body and sintered part. The quality of the green body density and uniform packing are dependent on the particle size and morphology of the powder used.

1.2.3.2 Wet Forming Techniques

Wet forming processes involve the suspension of ceramics powders in a liquid called a slurry. Slurries are formed by adding liquids such as water and possibly dispersive agents or surfactants to keep the ceramic suspended in the liquid. The slurries are poured into dies and either cured or dehydrated. Slip casting uses micro-porous molds that absorb the liquid from the slurry, leaving behind the ceramic powder in the shape of the part [23], Figure 1-4. Slip casting is commonly used in the formation of porcelain productions. For very large products such as turbine blades, gel casting is used. The ceramic slurries are made with polymers that polymerize once poured into a mold, forming hard green bodies with precise tolerances that can be machined [23]. If ceramics single or multilayer sheets are the desired geometry, tape casting is used. Tape casting spreads the ceramic slurry across a substrate, controlling the thickness with a doctor's knife [24], Figure 1-5. The slurries dry as the liquid evaporates, leaving behind a ceramic sheet.

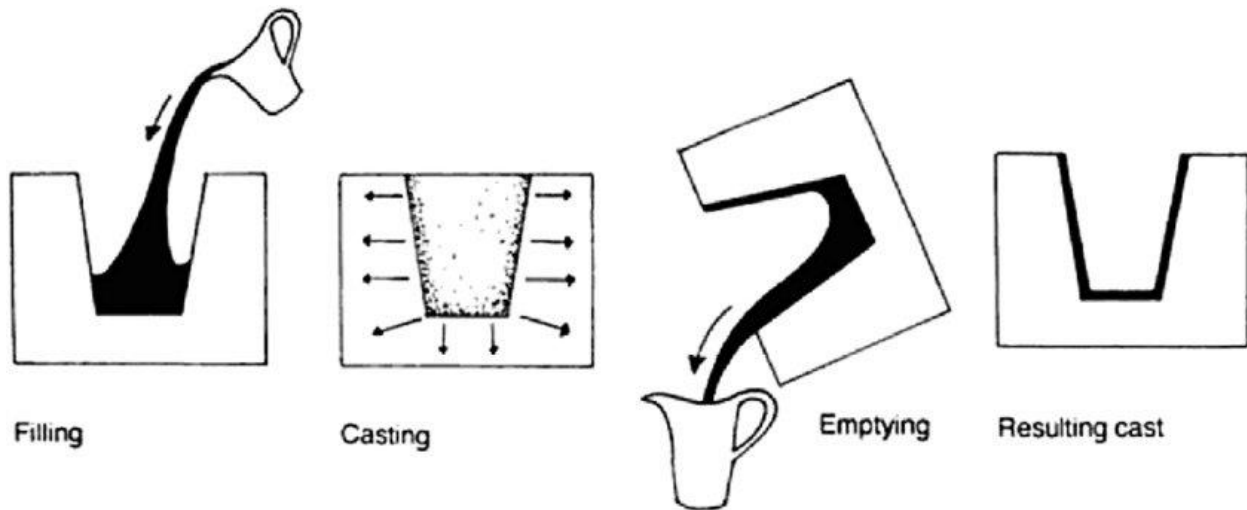


Figure 1-4: Schematic overview of slip casting process. Micro-porous mold is filled with ceramic slurry, liquid is absorbed into porous mold coating the mold with ceramic powders. Excess liquid is removed from the mold leaving the cast part of the perimeter of the mold. [23]

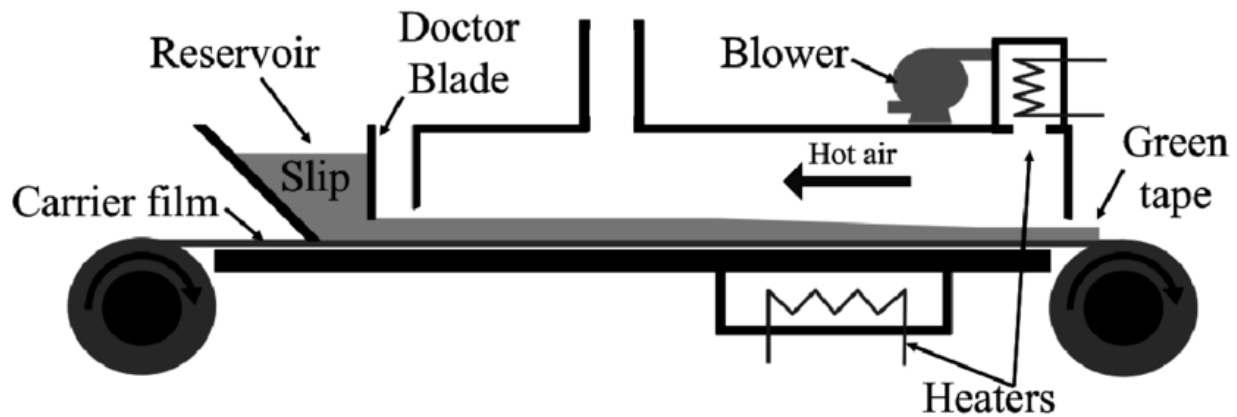


Figure 1-5: Schematic diagram showing overview of tape casting process. Ceramic slurry is spread across a substrate, while excess slurry is scraped away by a doctor blade, setting the desired height. Slurry layer is dried forming a ceramic green body sheet. [25]

Wet forming techniques offer the ability to produce large and complex shapes with ceramics, but require a drying process. The drying process involves the removal of the liquid, leading to volume changes in the ceramic green body. The volume shrinkage may lead to uneven ceramic particle packing and a non-uniform density, causing cracking during the sintering process. Wet forming techniques use slurries formed with numerous additives, which must then be removed or burned off during sintering process. This adds additional steps to the forming stages, slowing down production rates and offering possible contamination if not fully removed.

If the desired product is a tube or rods or even plates, then extrusion of a mixed wet/dry process is used. Additives are added to a ceramic powder, commonly polymer pellets, and melted to form a paste. The paste is then extruded through a die under pressure by a plunger or screw [26], Figure 1-6. Ceramic extrusion is a fast and continuous process; however, it is extremely limited by the shapes that can be formed and suffers from the same volume reduction challenges as does wet forming processes.

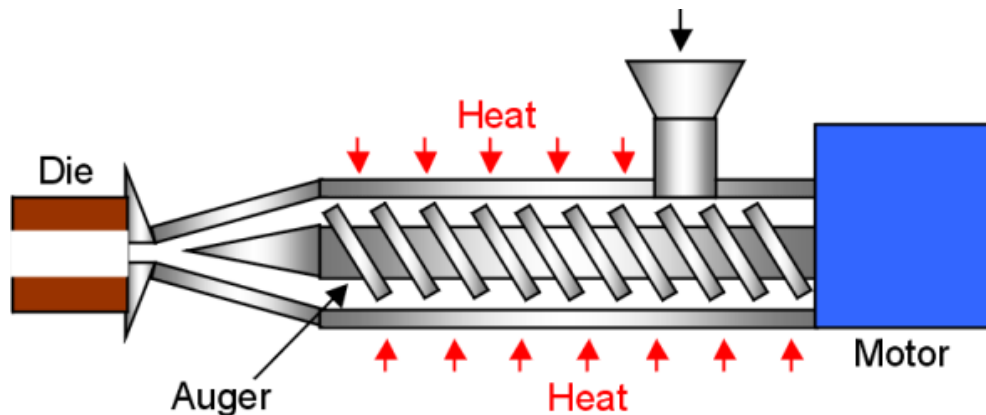


Figure 1-6: Schematic overview of ceramic extrusion processing apparatus. Ceramic powder mixed with polymer pellets are added to the hopper. Powder mixture is heated, forming a paste and extruded through a die by a screw forming the desired green body ceramic. [27]

Wet forming processes offer the ability to form large complex shapes with high tolerances. Wet processes are slower than dry processing due to a necessary drying stage for the produced green bodies. Wet forming challenges revolve around the volume shrinkage during drying while maintaining a uniform density as well removing any additives from the ceramic powder.

1.2.4 Ceramic Firing and Sintering

Sintering is the process of synthesizing a solid from a powder aggregate through the application of thermal energy. The sintering of aggregate particle compacts occurs through processes known as densification and coarsening. Densification and coarsening are separate processes that can happen individually or together during sintering. Numerous sintering techniques exist each having their own method of applying heat and other driving forces to control the sintering process. The sintering process plays a key role in microstructure evolution and controlling sintering is key to achieve a desired microstructure and properties.

1.2.4.1 Sintering Driving Force and Basic Phenomena

The driving force for sintering is the reduction in interfacial energy within a system. Each particle in the green body aggregate has total surface area (A) and specific surface energy (γ) with a total interface energy of γA . The same holds for the green body simply being the summation of all particles' interface energy. The reduction of the total interface energy of the green body

expressed as equation 1, drives the sintering process [28]. Changing interfacial energy, $\Delta\gamma A$, is densification. Densification occurs when solid-vapor interfaces or surfaces of particles interact forming solid-solid interfaces with lower interface energies. Densification results in the shrinkage of the material volume. Changing interfacial area, $\gamma\Delta A$, is referred to as coarsening or grain growth. Coarsening occurs when particles grow in volume by consuming neighbor particles. While the total volume is maintained during coarsening surface area decrease as it becomes concentrated in fewer but larger particles. Visual representation of densification and coarsening individually and combined are shown in Figure 1-7.

$$\Delta(\gamma A) = \Delta\gamma A + \gamma\Delta A \quad (1)$$

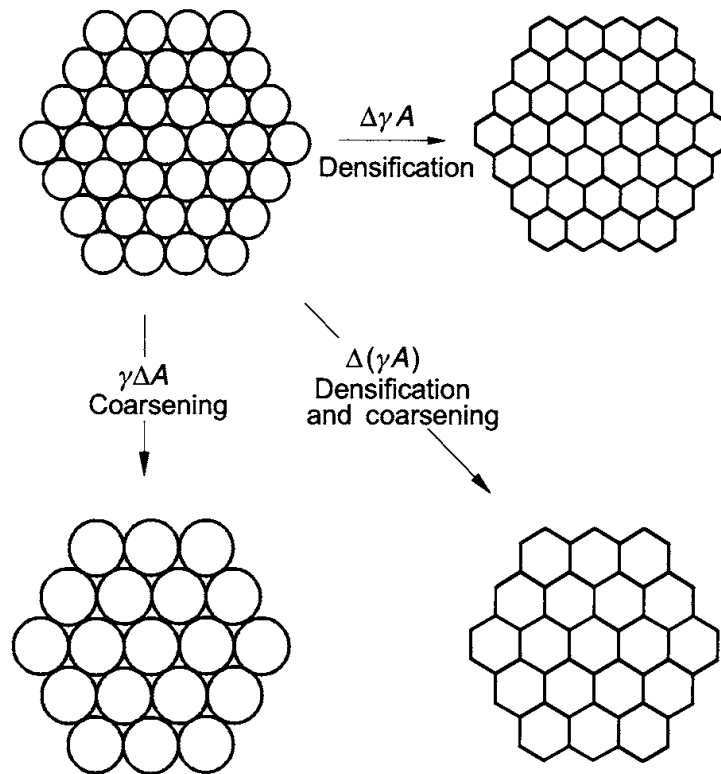


Figure 1-7: Schematic showing densification and coarsening of circular particles. Densification occurs via solid-vapor interfaces becoming solid-solid interfaces. Coarsening occurs with some particles growing at the expense of other reducing in number[28].

The reduction in interfacial energy is the thermodynamic driving force for sintering. Kinetic material diffusion however, is induced by bulk and vapor pressure differences as well as vacancy concentrations resulting from interface curvature [28]. For a curved solid-vapor interface, shown in Figure 1-8, the pressure of a curved surface is calculated using equation 2 for the condensed phase. With r being the radius of curvature, γ is the excess surface free energy and Region I has a positive radius of curvature (r) resulting in a higher pressure than region II with a negative radius of curvature. Oppositely, the pressure of a curved surface for a vapor phase can be calculated using equation 3. With V_m^α being the molar volume of the condensed phase, r the radius of curvature, γ the excess surface free energy. For the vapor phase region I has a negative curvature and therefore a lower pressure than region II with a positive curvature. The solid phase atoms diffuse from high to low pressure, migrating from region I to region II. For the vapor phase, vacancies migrate from high to low pressure moving, from region II to region I. Therefore, due to curvature, mass migrates from region I to II, reducing the curvature of the interface over time via diffusion.

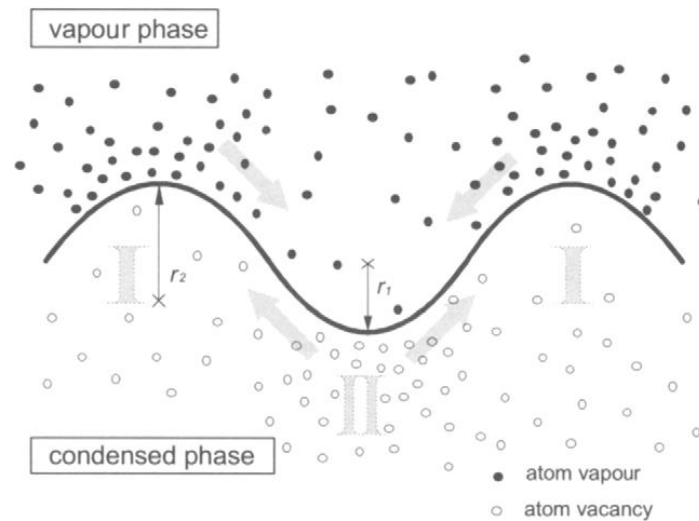


Figure 1-8: Schematic of a solid-vapor interface showing the migration path of atoms and vacancies driving by pressure differences in region I and II resulting from curvature. [28]

$$P^\alpha = P_\infty + \frac{2\gamma}{r} \quad (2)$$

$$P^\beta = P_\infty + \frac{2\gamma P_\infty V_m^\alpha}{r RT} = P_\infty \left(1 + \frac{2\gamma V_m^\alpha}{RT r} \right) \quad (3)$$

1.2.4.2 Three Stages of Sintering and the Two Particle Model

Sintering is commonly broken up into three stages: initial, intermediate and final, or neck formation, interconnected pores, and isolated pores [29], Figure 1-9. The initial stage starts with a green body compact and lasts through neck formation between particles. Green body particles, assuming spherical morphologies, start with simple point contacts with their neighbors. Non-spherical morphologies alter how the particles are packed and interact with its neighbors. During the initial stage of sintering, material diffuses to the contact point due to the pressure differential from curvature, expanding it forming a neck between the particles [30]. The mechanism by which the material diffuses to the neck determines if coarsening or densification or both occur. If coarsening occurs, the distance between the two particle centers do not change while the neck diameter and resulting grain boundary increases in size, Figure 1-10 (a). If densification occurs during neck formation, the interparticle distance decreases as material from the grain boundary moves to the surface neck, increasing its size, Figure 1-10 (b).

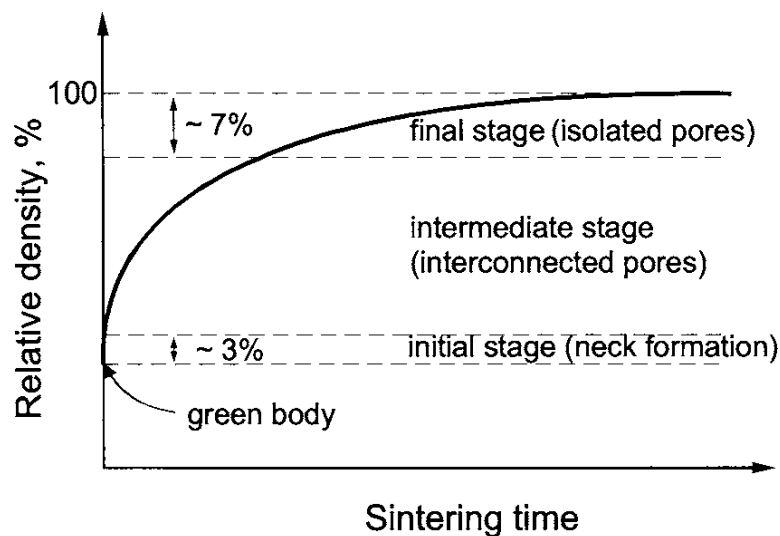


Figure 1-9: Graph of relative density as a function of sintering time showing increasing density with time broken into the three stages of sintering. [28]

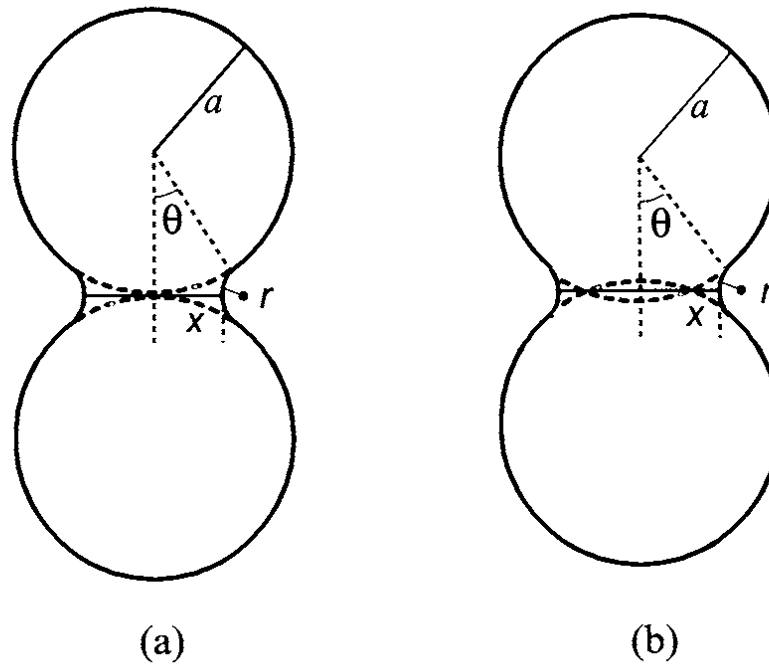


Figure 1-10: Diagram of simple two particle model (a) showing coarsening with neck formation and growth from surface atoms (b) showing densification with neck formation and growth from grain boundary atoms moving the two particles closer. [28]

Multiple methods of diffusion are available for material during sintering [31]. Table 1-1 list possible mechanisms, including the source and sink of the material and the limiting parameter that defines the speed of the materials migration for a given mechanism. Figure 1-11 Shows the transport mechanism pathways for a simple two particle model. Material migrating from the surface of the particles to the neck results in coarsening but not shrinkage, mechanisms 4-6. For the two particles to densify and shrink, the center of the two particles must move toward each other [32]. For the interparticle distance to change, mass from the grain boundary is required to move to the neck at the surface, mechanisms, 1-3.

Table 1-1: Diffusion Mechanism and Pathways During Sintering [28]

Material transport mechanism	Material source	Material sink	Related parameter
1. Lattice diffusion	Grain boundary	Neck	Lattice diffusivity, D_l
2. Grain boundary diffusion	Grain boundary	Neck	Grain boundary diffusivity, D_b
3. Viscous flow	Bulk grain	Neck	Viscosity, η
4. Surface diffusion	Grain surface	Neck	Surface diffusivity, D_s
5. Lattice diffusion	Grain surface	Neck	Lattice diffusivity, D_l
6. Gas phase transport			
6.1. Evaporation/condensation	Grain surface	Neck	Vapour pressure difference, Δp
6.2. Gas diffusion	Grain surface	Neck	Gas diffusivity, D_g

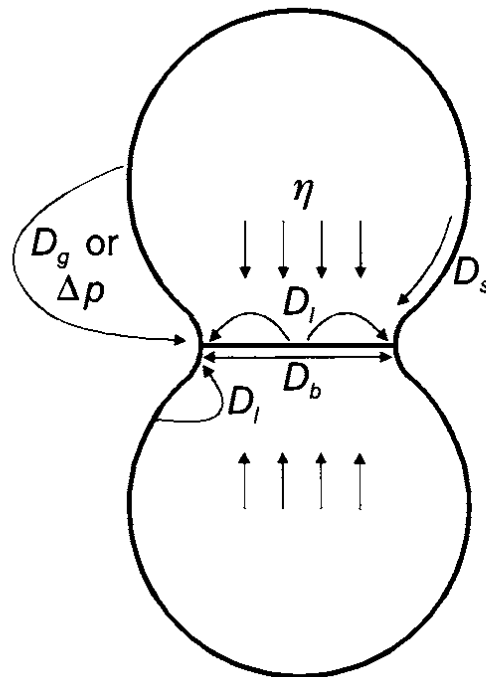


Figure 1-11: Diagram of the two-particle model showing mass transport pathways described in Table 1-1. [28]

As the necks form and their diameter grows, grain boundaries are formed. Grain boundaries are the solid-solid interface between the two particles with their perimeter being the neck. Grain boundaries will be discussed in greater detail later. As necks and grain boundaries

continue to grow, a network of interconnected pores form channels ending the initial stage of sintering. During the intermediate stage of sintering the necks and grain boundaries continue to grow, decreasing the size of the pore network, Figure 1-12 (a). Eventually, neck growth impinges on the pore network, creating isolated pores beginning the final stage of sintering, Figure 1-12 (b). Isolated pores are pockets of trapped gas. In the final stage of sintering these pockets of trapped gas shrink, eventually reaching a pressure equilibrium and stop shrinking, Figure 1-13. At this point sintering is generally considered complete and a final maximum density is achieved. The trapped pores become features of the material's microstructure.

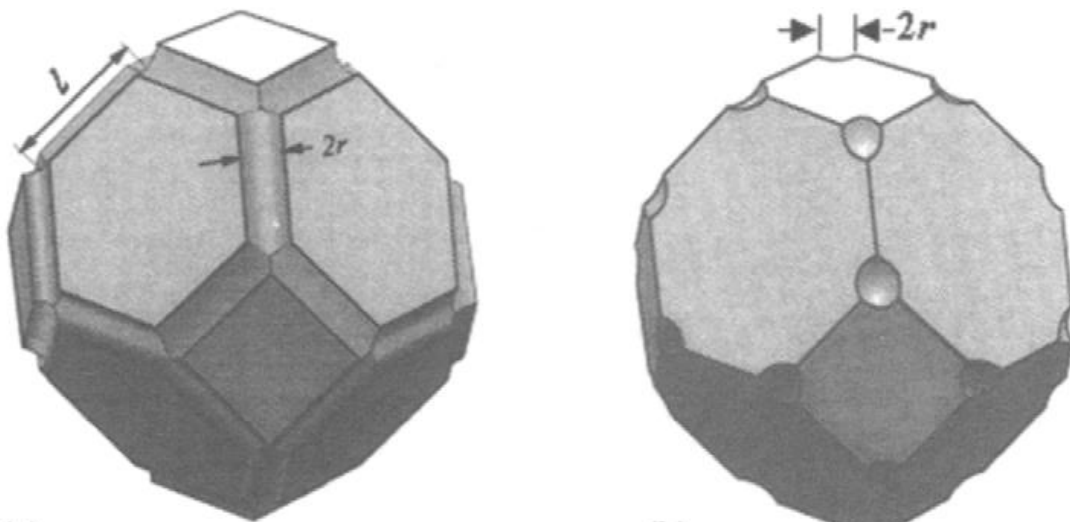


Figure 1-12: Schematic showing (a) network of connected pores during intermediate sintering stage and (b) isolated pores formed shrunk during the final stage of sintering. [28]

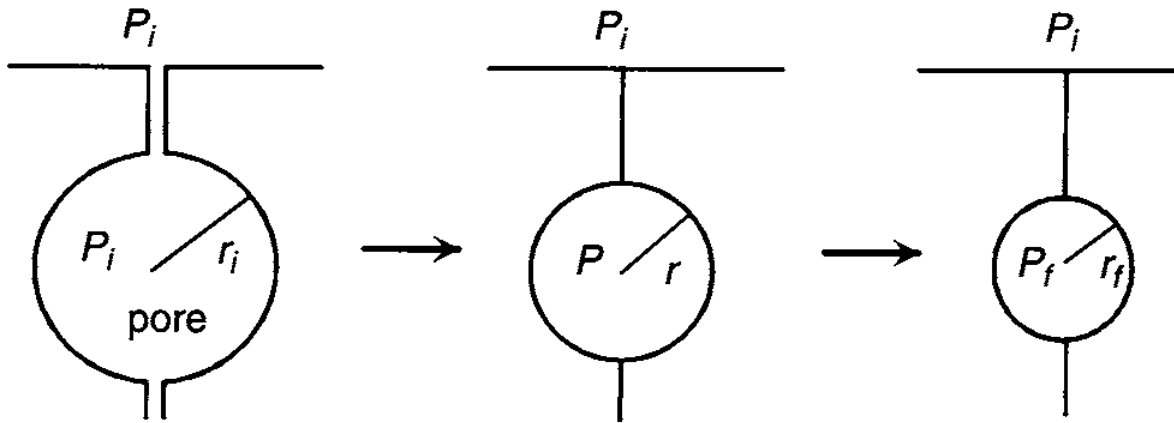


Figure 1-13: Schematic showing the formation of isolated pores and shrinkage during final stage sintering until an equilibrium pressure is reached. [28]

1.2.4.3 Sintering Variables

The sintering process is dependent on many variables involving the raw material used and the forming technique as discussed in the prior sections; also, sintering variables for the sintering technique used. Raw material variables such as particle size, distribution, morphology, agglomeration, impurities and chemical homogeneity influence the sintering behavior of a material [33]. Decreasing particle sizes increases the amount of surface area present as well as increases the curvature, as smaller particles have greater curvature. Bimodal distributions of powder particles alter the packing density in green bodies, reducing initial pore size and starting grain size distribution [34]. Particle morphology changes how particles are packed and how they are connected prior to neck formation as well as interface curvature. Large agglomerates may see grain growth within the agglomerate while it is forming necks with neighbor particles resulting in bimodal grain size distributions [35]. Sintering shape formation variables such as packing density, pore distribution and granulation texture influence the sintering behavior of a material as well.

Sintering is also influenced by the sintering technique used each having variables such as temperature, heating rate, pressure, and environmental conditions. Higher temperatures increase diffusion rates and may change which diffusion mechanism is dominant [36]. The addition of pressure on the green body during sintering alters the driving force by adding to the pressure resulting from curvature, including a geometry term to explain the application, equation 4.

Ceramic literature contains extensive work from papers to books attempting to understand and model the sintering process and the role of all the variables in an effort to exert control over the final microstructure [28]–[32], [37].

$$P = \frac{\gamma}{r} + f(\rho, \text{geometry})P_{\text{appl}} \quad (4)$$

1.2.5 Ceramic Microstructure Characterization

With the completion of sintering the former particle aggregate is now a single solid ceramic body with a distinct microstructure and material properties. As discussed previously the properties of a material are dependent on the microstructure formed during sintering. Determination of material properties is done through what is generally known as microstructural characterization, which is term covering a wide range of material science techniques. Microstructural characterization of microstructures analyzes the effect of the processing history of the ceramic and track microstructure features such as pores and grain boundaries during processing. Understanding how the microstructure evolves during processing and how processing variables alter the microstructure is key to controlling the final microstructure and resulting properties.

1.2.5.1 Grain Growth: Normal and Abnormal

Material coarsening during grain growth occurs with some grains growing at the expense of others. The grain boundary of the growing grain migrates into neighbor grains absorbing their material volume. As the growing grain expands in volume its surface area to volume ratio declines resulting in declining amounts of grain boundary surface area and excess free energy. Increasing in size the radius of curvature of grains decrease, thereby decreasing the driving force for the grain to continue and slows growth resulting in a practical limit to the grain size for a material [28]. Shrinking grains lose volume, increasing their surface area to volume ratio increasing the driving force for them to shrink as their radius of curvature increases. Therefore, shrinking grains shrink faster the smaller they become, inverse of large gains. The grain size time dependence for ideal 3D grains is equation 5 with R_i being initial and R_f the final average grain radius, K is a positive constant representing the grain growth rate, and n is $\leq 1/2$. The value of n is $1/2$ under ideal grain growth conditions with most reported results falling below $1/2$.

$$R_f - R_i = (kt)^n \quad (5)$$

Grain growth occurs as either normal or abnormal grain growth. Normal grain growth occurs when the grain size increase in a uniform manner resulting in a unimodal distribution of grain sizes [38]. Normal grain growth microstructures appear having grains of similar sizes with all grains present having increased in size during the grain growth process. Example representative microstructures are shown in Figure 1-14 at 15 and 720 minutes. Normal grain growth is also referred to as continuous grain growth.

Abnormal grain growth occurs when a subset of grain increase in size at a faster rate than the other matrix grains [38]. Abnormal grain growth results in microstructures containing a few large grains in a small grain matrix. The growth of the small grains during abnormal grain growth is inhibited and minimal growth occurs. The grain size distribution takes on a bimodal distribution. Example representative microstructures are shown in Figure 1-14 at 30 and 60 minutes. Abnormal grain growth is also referred to as discontinuous grain growth.

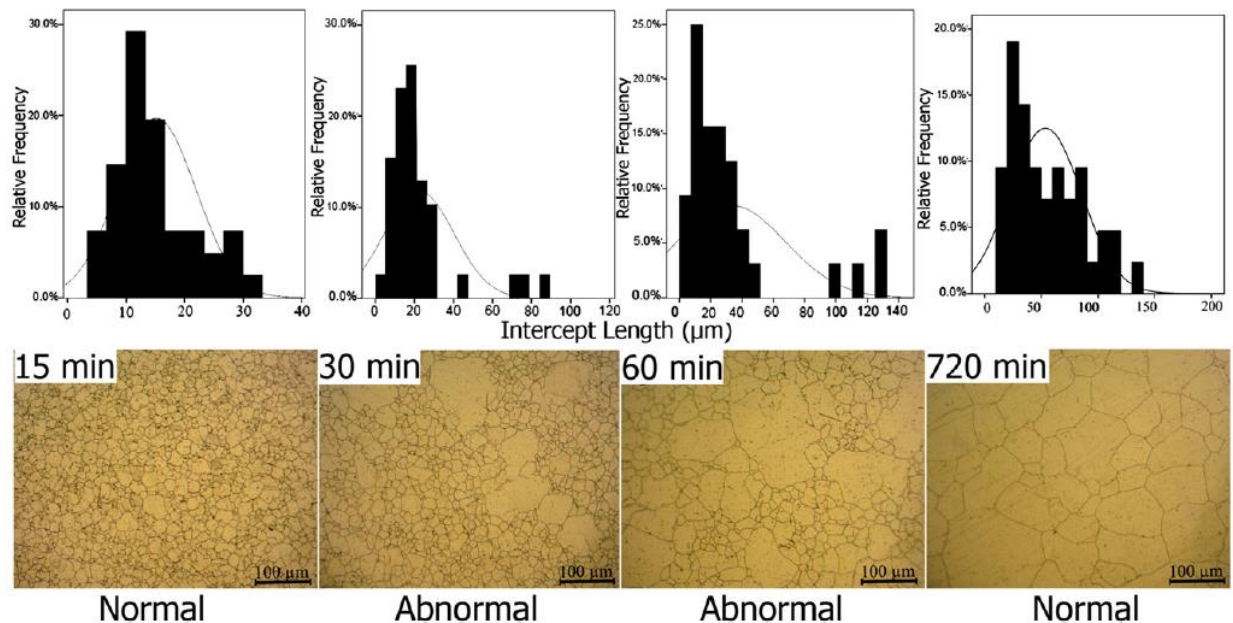


Figure 1-14: Optical images of AISI 304L stainless steel showing normal and abnormal grain growth microstructures that develop at different annealing times at 900°C. Corresponding grain size distributions are shown. [39]

1.2.5.2 Role of Grain Boundary in Grain Growth

As discussed previously in this chapter the grain size, distribution and grain boundaries of a material strongly impact the mechanical properties. At the time of writing this document, it is not fully understood what the cause for some grains to grow rapidly and other not resulting in abnormal grain growth. Numerous ideas exist and are being scientifically tested. As grain growth only occurs with the migration of grain boundaries, what role the grain boundary plays has become of great interest. For abnormal grain growth to occur grain boundaries for a subset of grains needs to have significantly higher mobility along its perimeter. Work done by Rohrer et al. [40] proposed that grain boundaries undergo a structural transition induced by picking up impurities during migration, altering the grain boundary structure. Yoon et al. [41] suggest that grain boundary faceting inhibits grain boundary migration and abnormal grains grow rapidly by not having faceted boundaries.

1.3 Classical Isotropic Grain Boundary Structure and Migration

1.3.1 Grain Boundary Formation and Structure

Grain boundaries are crystal defects that have an associated excess free energy compared to the bulk crystal. Grain boundaries are solid-solid interfaces that form during sintering when two solid-vapor interfaces or surfaces meet. The two solid-vapor interfaces bind together forming a single defect with a lower excess free energy than two separate free surfaces [11]. It follows that the grain boundary interface energy is lower than that of the two free surfaces, otherwise the grain boundary would not form. Therefore, a simple estimation of the grain boundary energy follows equation 6 where the grain boundary interface energy equals the energy of the two free surfaces minus the recovered energy from the binding process.

$$\gamma_{gb} = 2\gamma_s - B \quad (6)$$

Grain boundaries may be either twist or tilt boundaries, Figure 1-15. Twist grain boundaries form when the misorientation is perpendicular to the grain boundary plane normal. Tilt boundaries are formed when the misorientation is parallel to the grain boundary plane normal. Identification of specific grain boundaries require the use of 5 independent parameters.

Considering two neighbor grains, 3 parameters are required to define the rotation from grain 1 orientation to grain 2 orientation commonly expressed as Euler angles. Then 2 parameters to identify the grain boundary plane in term of $\{hkl\}$ in the coordinate system of grain 1. Only two of h , k , or l is needed, as the vector is a unit vector and with two known values of a unit vector the third can be calculated and is no longer independent. Other parameters exist to describe the translation of the crystal; however, the five listed are commonly used in the literature.

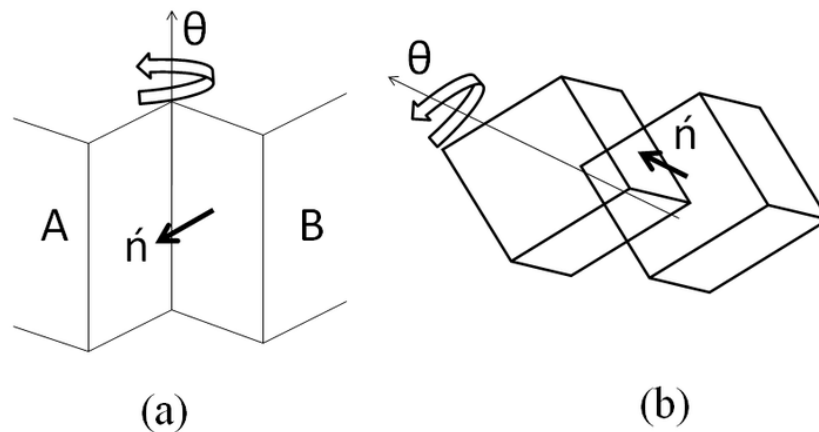


Figure 1-15: Schematic showing the structure of tilt (a) and twist (b) boundaries. Tilt boundaries are rotated parallel to the grain boundary and twist are rotated perpendicular to the grain boundary[42].

The classic model for grain boundaries with low angle misorientations was developed by Read and Shockley. Read and Shockley's model utilized dislocations to accommodate for small lattice misorientations [43]. Each dislocation corresponds to a specific amount of excess free energy. As a grain boundary misorientations increase from zero, the degree of misorientations corresponds to a proportional number of discrete dislocations, Figure 1-16. The total grain boundary energy at low misorientations where dislocations are far enough apart to not have their strain fields interact is therefore simply the energy summation of all distinct dislocations required to compensate for the degree of misorientation. As the grain boundaries, degree of misorientation increases along with the number of dislocations, the dislocations begin to interact, complicating the energy calculation of the grain boundary. Experimental work has shown that the Read and Shockley model for grain boundaries is effective for misorientations of less than 6 degrees [11].

Grain boundary energy calculated for misorientations higher than 6 degrees underestimate the energy.

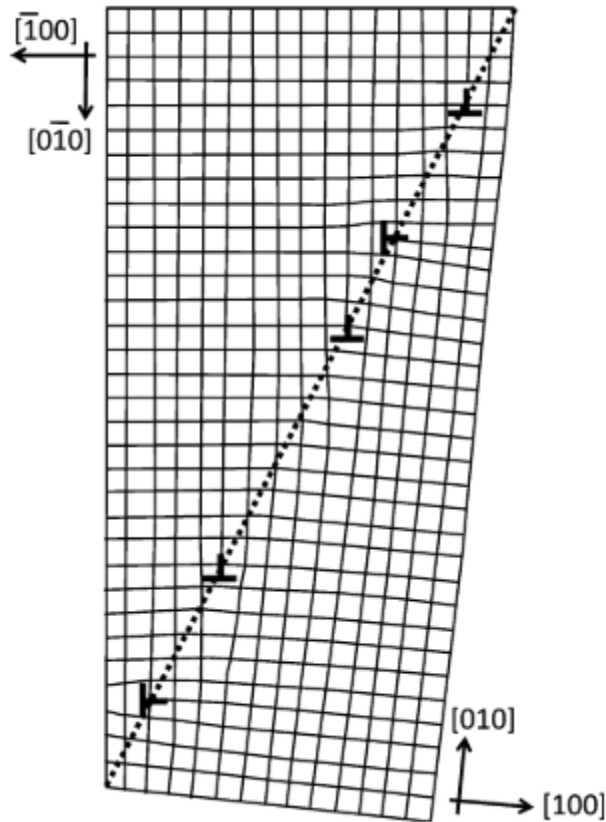


Figure 1-16: Schematic showing Read and Shockley dislocation model for grain boundaries where misorientations corresponds to dislocations. [44]

Another description of grain boundaries developed from the coincident site lattice. Kronberg and Wilson [45] discovered that common grain boundaries in Cu corresponded to misorientations where atomic sites were coincident with both lattices. These coincident site boundaries were named for the size of coincident lattice relative to the crystal lattice and is also the inverse of the coincident site fraction. A grain boundary with $1/3$ coincident lattice sites would be called a $\Sigma 3$ boundary and a site with $1/25$ coincidence would be a $\Sigma 25$ boundary. Examples of 4 low- Σ boundaries are shown in Figure 1-17 with rotations of cubes about a $[100]$ axis. The importance of the coincident lattice site boundaries came from experimental work in Pb-Sn that measured grain boundaries with a high coincidence migrated faster than those with

low to no coincidence [46]. While coincident site lattices provide insight into the structure of the grain boundaries and identification of boundaries with special properties, it does not provide any insight into the determination of the grain boundary energy as the Read and Shockley model does.

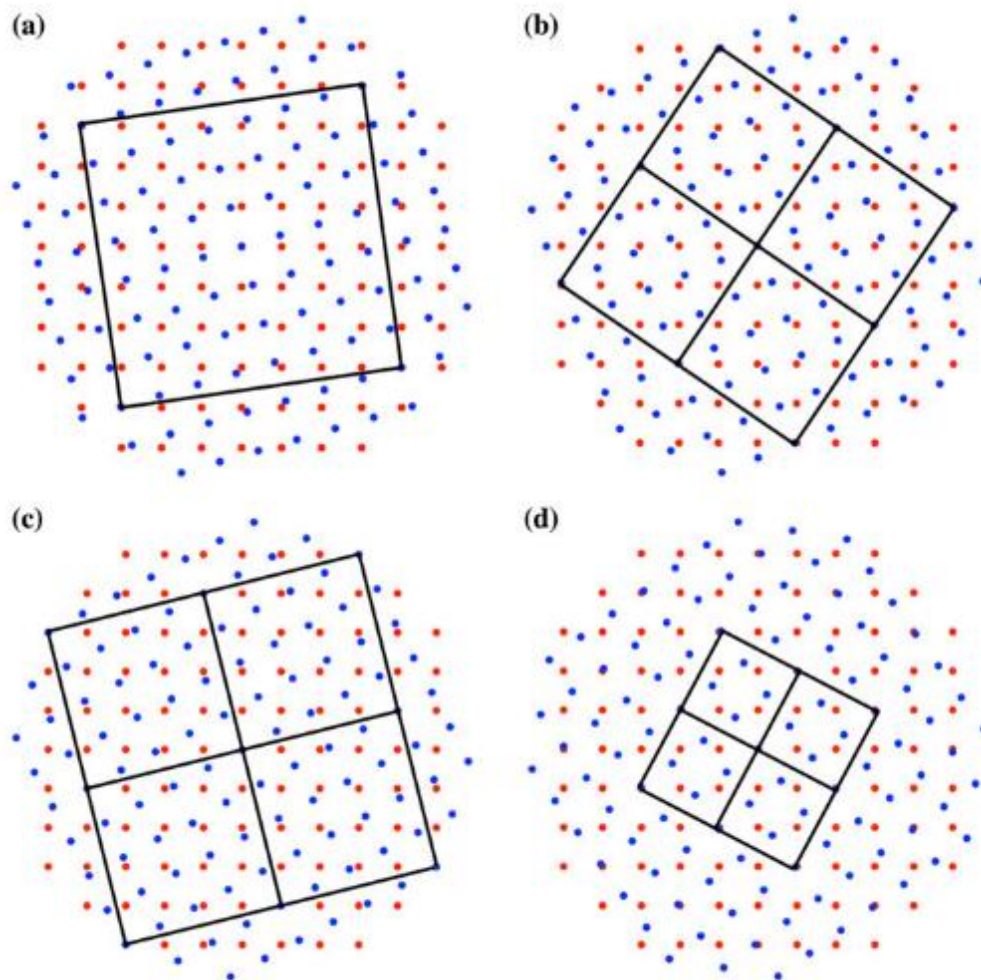


Figure 1-17: Schematic showing (a) Σ 25 at 16° rotation, (b) Σ 13 at 22° rotation, (c) Σ 17 at 28° rotation, and (d) Σ 5 at 36° rotation. The black boxes show the repeating CSL cell for each Σ boundary. [44]

1.3.2 Isotropic Grain Boundary Migration

Intrinsic grain boundary migration occurs when atoms are transferred across the grain boundary, resulting in migration without any drag forces. The velocity of the boundary (V_b) is

then the product of a driving force (F_b) and the mobility of the grain boundary (M_b) detailed in equations 7-9 as derived by Turnbull [47]. The driving force is the product of the grain boundary curvature (κ) and the grain boundary interface energy (γ_b) under ideal conditions. The mobility term is defined by the site factor (f) relating the density of core sites with high jump probabilities, the self-diffusion coefficient (D_b) of the rate limiting species and the ionic volume (Ω) as a function of the number of slow diffusing ions (δ). This form of the mobility term indicates that the mobility is constant for the entire boundary or isotropic, and therefore a linear relationship between the driving force and velocity exists. The mobility can vary between different boundaries within a material, however, as the structure and orientation of the boundaries are different. Use of this model is limited as measured grain boundary migration rates fall well below calculated values using estimated mobility values.

$$V_b = F_b M_b \quad (7)$$

$$M_b = \frac{f D_b \Omega}{\delta k_b T} \quad (8)$$

$$F_b = \gamma_b \kappa \quad (9)$$

1.3.3 Grain Boundary Drag Forces

The poor accuracy of Turnbull's model is partially explained due to the use of an ideal driving force. Real systems are not pure materials having ideal microstructures. Real materials have defects and impurities which inhibit grain boundary migration through the formation of drag forces.

1.3.3.1 Solute Drag

Impurities within a material will have an interaction potential with the grain boundary resulting in impurities being attracted to or repelled from the grain boundary [48]. This results in impurities forming a spatial profile with the grain boundary and concentration gradients to balance the interaction potential. Intrinsic defects in non-stoichiometric materials will behave in a similar manner resulting in a spatial distribution [49]. With the grain boundary with $V_b = 0$, an equilibrium distribution is reached. During grain growth the grain boundary will migrate disrupting this distribution. Migration of the grain boundary will drive diffusion of the solute in

the same direction of the grain boundary through an increasing interaction potential. If the grain boundary migrates with a consistent velocity, a steady state in the compositional profile will be achieved.

The compositional profile will depend on the solute's diffusivity, and strength of the interaction potential and grain boundary velocity. Compositional profiles for solutes attracted to the boundary calculated by Cahn [48] are shown in Figure 1-18. The velocity of the grain boundary increase from a-e with c having the maximum solute drag force on the grain boundary. Initially with low velocities (a-c), solute desorbs across the entire profile, however significantly more at the front of the grain boundary. At higher velocities, d-e, the desorption in front of the grain boundary levels off while continuing behind the grain boundary, resulting in decreasing drag forces at d and e. As the velocity continues to increase, eventually the grain boundary will break away from the solute and solute drag will no longer inhibit the grain boundary's migration.

For solute that is repelled from the boundary, the composition profiles worked out by Cahn [48] are shown in Figure 1-19. With velocity starting at zero, the steady state profile is a depleted zone around the grain boundary. As the velocity begins to move a pile up of impurities forms in front of the grain boundary resulting in the maximum drag force. As velocity continuous to increase and the solute is no longer able to keep up, the depleted zone around the boundary begins filling as the solute is passed by the boundary instead of pushed, lowering the drag force. Eventually with a high enough velocity the grain boundary will break free of the solute and no longer experience any drag force.

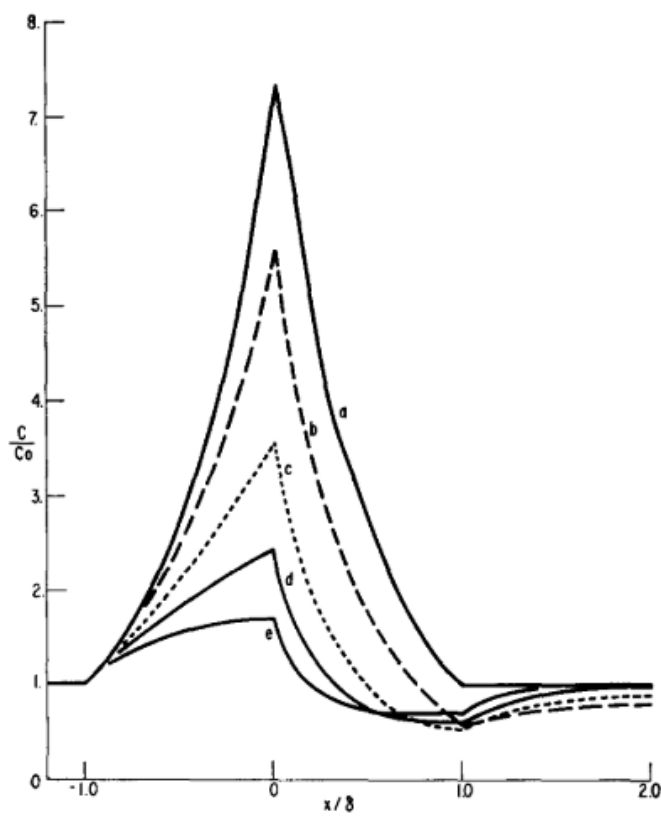


Figure 1-18: Graph showing attractive solute concentration profiles at increasing velocities from a-e. [48]

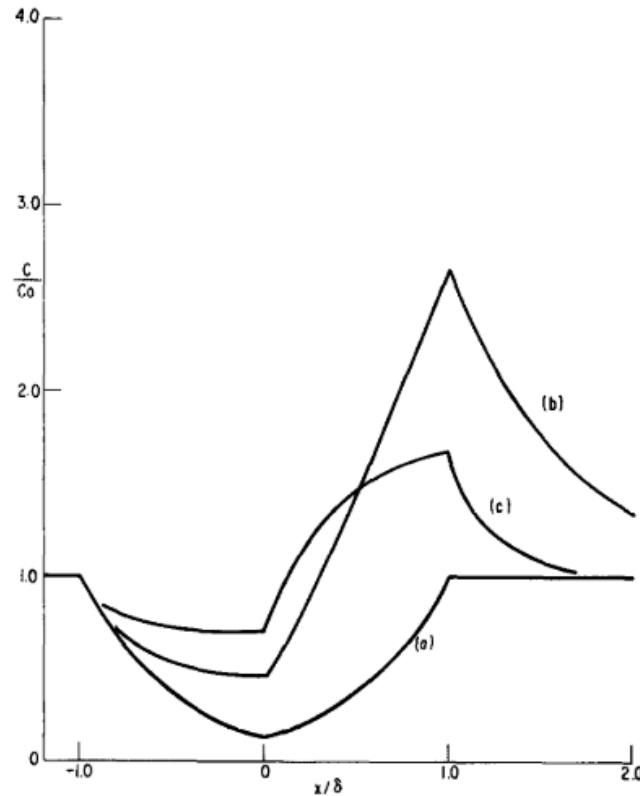


Figure 1-19: Graph showing repelled solute concentration profiles at increasing velocities from a-c [48]

The driving force for a pure material is the intrinsic driving force from curvature and has a linear relationship with the velocity of the grain boundary, Figure 1-20 (a). The driving force and velocity relationship for solute drag is shown in Figure 1-20 (b) where at low velocities the force required is high until the critical force is reached when the grain boundary begins to break away from the solute cloud. A combined force and velocity profiles are shown in Figure 1-20 (c), showing the total drag force experienced by a grain boundary under the influence of intrinsic and solute drag. Solute drag dominates at low velocities, however, as the grain boundary eventually breaks away intrinsic drag becomes dominant.

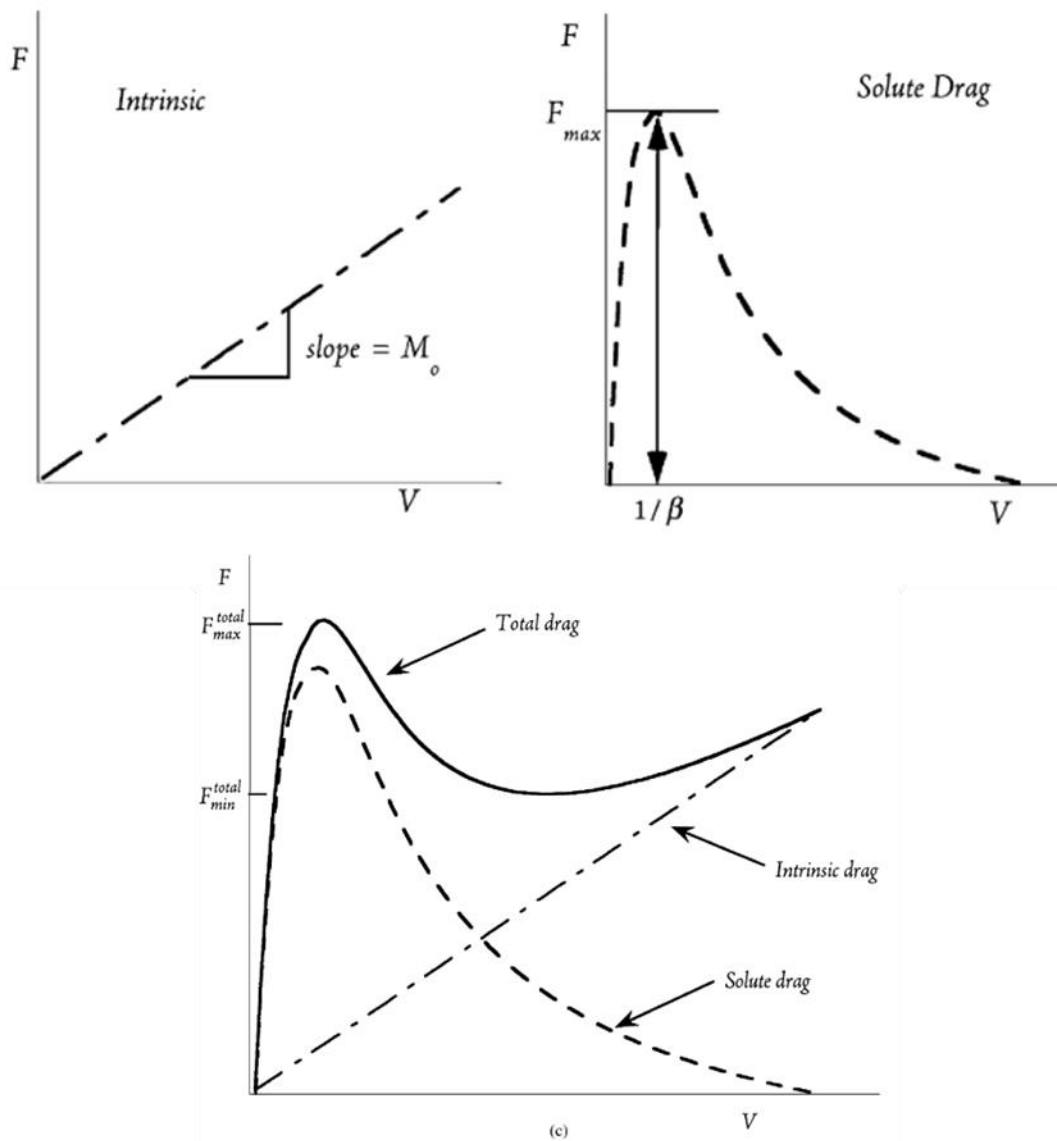


Figure 1-20: Graphs showing the driving for as a function of velocity for (a) intrinsic drag, (b) solute drag, (c) total drag. [48]

1.3.3.2 Smith-Zener Particle Pinning and Pore Drag

The presence of second phase particles that do not wet grain boundaries inhibit grain boundary migration with a pinning force. When a grain boundary passes a second phase particle, the area of the grain boundary that would be within the particle is removed reducing the excess free energy of the boundary [50]. As the grain boundary passes the particle to continue, it must

recreate that now missing area of the grain boundary, which costs energy. Note that, depending on the shape of the particle, as the grain boundary crosses the object, the missing grain boundary surface area changes with time, Figure 1-21. Therefore, the boundary attempts to remain attached to the particle causing the grain boundary to bend around the particle. This bending results in an increasing curvature of the boundary, thereby increasing the excess free energy of the grain boundary. Eventually the excess free energy from curvature reaches a critical level equaling the excess free energy penalty of creating the missing grain boundary area. It then becomes energetically favorable for the grain boundary to break away from the particle and create the missing grain boundary surface area.

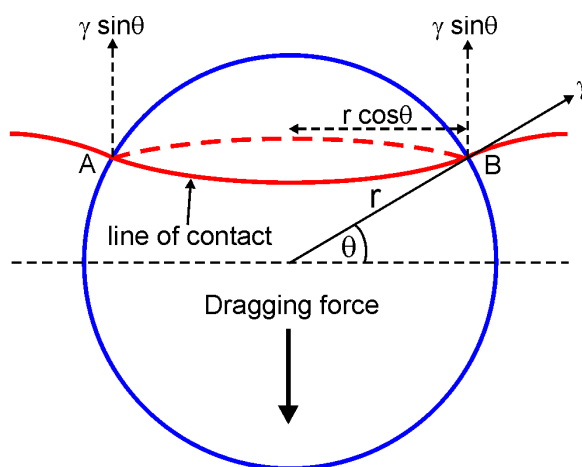


Figure 1-21: Schematic showing particle-grain boundary attachment. Theta increases as boundary moves away from the particle leading to an eventual break away event. [50]

Pores act in a similar manner when pinning grain boundaries; however, while particles have almost no mobility to move pores have some. As a grain boundary passes a pore, the pore's leading edge may attach to the grain boundary and attempt to move with the grain boundary. The pore will move by diffusion of particles from the leading edge of the pore to the trailing surface via surface diffusion or evaporation and condensation, Figure 1-22. The driving force for the diffusion across the pore is the curvature of the pore surfaces. As the pore has very limited mobility compared to the grain boundary, the pore is dragged by the boundary applying a drag force when the grain boundary velocity exceeds the pores maximum [50]. As the pore can have uneven curvature, if not at equilibrium, the drag force applied by the pore is not uniform across

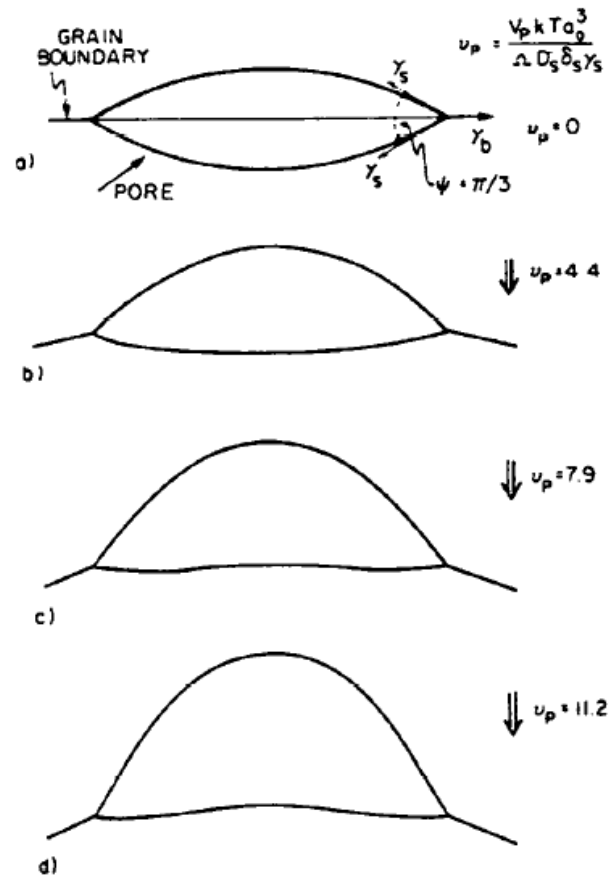


Figure 1-23: : Schematic of pore shape as a function of grain boundary velocity increasing from a-d. Increasing velocity increases the lag of the trailing edge of the pore distending the pore. [50]

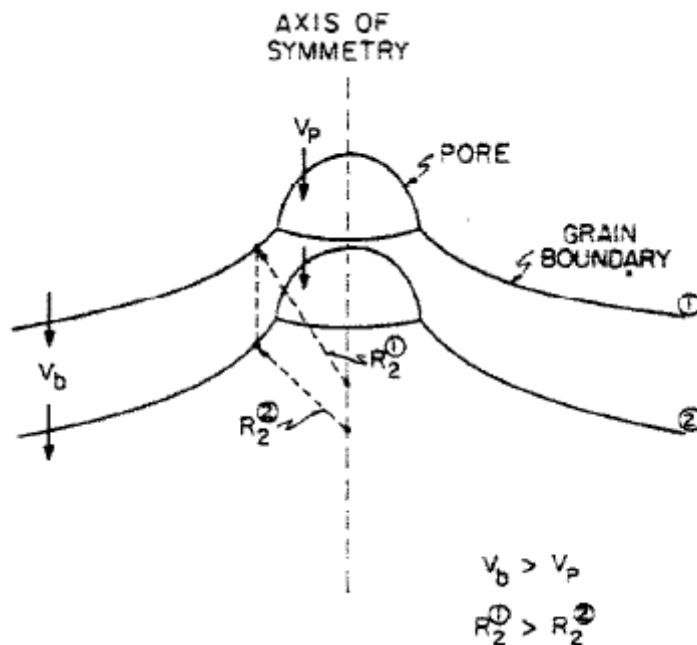


Figure 1-24: Schematic showing increasing grain boundary curvature near pore interface increasing boundary energy eventually leading to break away. [50]

1.4 Grain Boundary Energy Anisotropy

Up to this point all discussion of grain boundaries have made the implicit assumption that the grain boundaries were isotropic. It assumed that each part of a grain boundary was the same as any other part of the same grain boundary and behaved in the same way. This assumption, however, is incorrect, as evidenced by the models being unable to predict microstructural evolution and experimental evidence.

1.4.1 Anisotropic Grain Boundary Structure and Migration

Grain boundaries may take on two forms. Grain boundaries can be faceted when the grain boundary breaks down into repeating segments called facets or steps of various sizes. More will be discussed later in this document on this topic, but for now the grain boundary forms facets due to the grain boundary orientation being unstable. The grain boundary, therefore, minimizes its energy by breaking into small segments of stable orientations while keeping the overall macro-curvature of the boundary. The second type of grain boundary structure is the non-faceted boundary or atomically rough boundary, where the macro curvature is maintained, and the grain boundary orientation is stable.

Previously discussed models involving atoms jumping across the grain boundary, inducing migration in isotropic boundaries, is no longer valid. Faceted boundaries must maintain their segmented structure during migration, and random walk diffusion across the grain boundary would disrupt the structure. Faceted boundaries move through nucleation and growth of entire facet segments, Figure 1-25. To migrate a faceted boundary will nucleate a step on the interface and then the step will grow parallel to the grain boundary causing the grain boundary to move. The rate at which a faceted grain boundary can move depends on the nucleation energy for a facet step which will vary with different facets. Therefore, for faceted grain boundaries there will be a limiting facet that will set the pace for migration. The non-faceted grain boundaries can still migrate by atoms jumping across the grain boundary making the isotropic model useful in some cases.

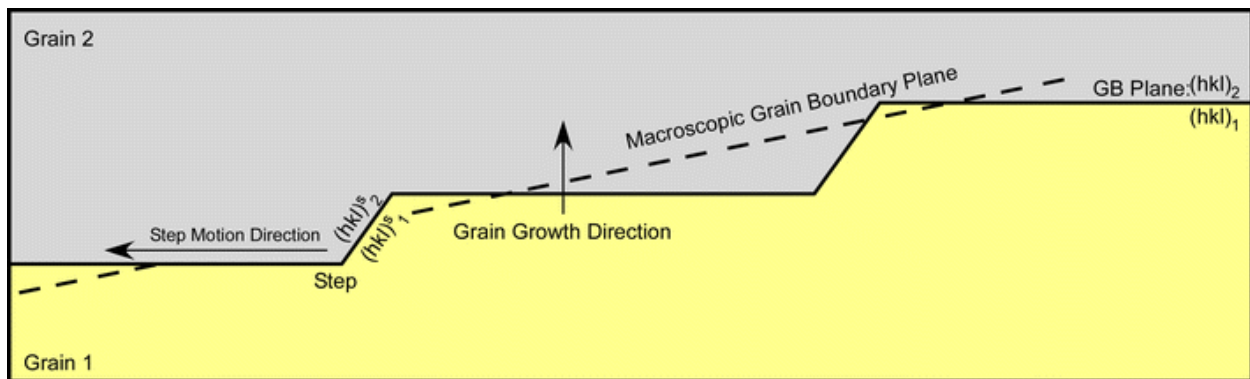


Figure 1-25: Schematic showing a faceted grain boundary conforming to macroscopic curvature and step nucleation and growth resulting in grain boundary migration. [51]

As discussed previously, the driving force for grain growth is the reduction in surface area of grain boundaries. Due to grain boundary anisotropy, the driving force will differ between boundaries and between facets on a single grain boundary. As will be discussed later, the grain boundary structure and energy is dependent upon the misorientation, Figure 1-26. As misorientation increases so does the grain boundary energy until the half way point then beginning to decrease as crystal symmetry comes in to play. However, in Figure 1-26 for the $[111]$ there is a large energy drop which is associated with a twin or $\Sigma 3$ boundary. Therefore, the grain boundary energy is dependent upon the misorientation of the grain boundary.

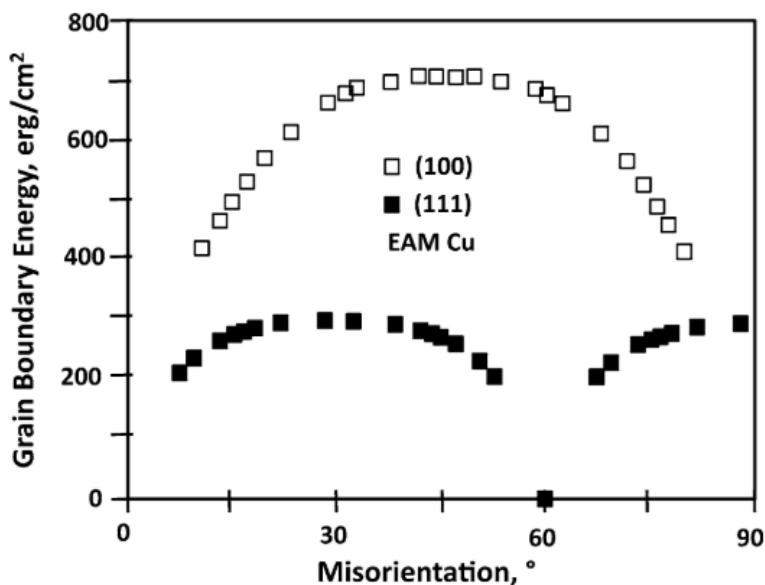


Figure 1-26: Graph of grain boundary energy as a function of misorientation for copper for the (100) and (111). [44]

Experimental work has been done to try and understand the effect of the grain boundary energy anisotropy and is still ongoing. Work done in the BaTiO_3 system [52] has measured abnormal grain growth in the system with the large grains all having faceted grain boundaries. When the system was studied in an H_2 environment, the grain boundaries demonstrated normal grain growth with the large grains grain boundaries undergoing a roughing transition from faceted to rough. Therefore, in the BaTiO_3 system faceted grains migrate faster. Work done by Rheinheimer et al. [53] measured the growth of single crystals of SrTiO_3 of various orientations in polycrystals, Figure 1-27. The growth rate of the single crystal into the polycrystal was different depending on the interface orientation of the single crystal. Similarly, the structure of the grain boundary of the single crystal varied across single crystal orientations, with (100) having a flat boundary while the (110) resulted in a faceted boundary structure. The changes in behavior were attributed to the changing orientation of the grain boundary selected by altering the single crystal orientation.

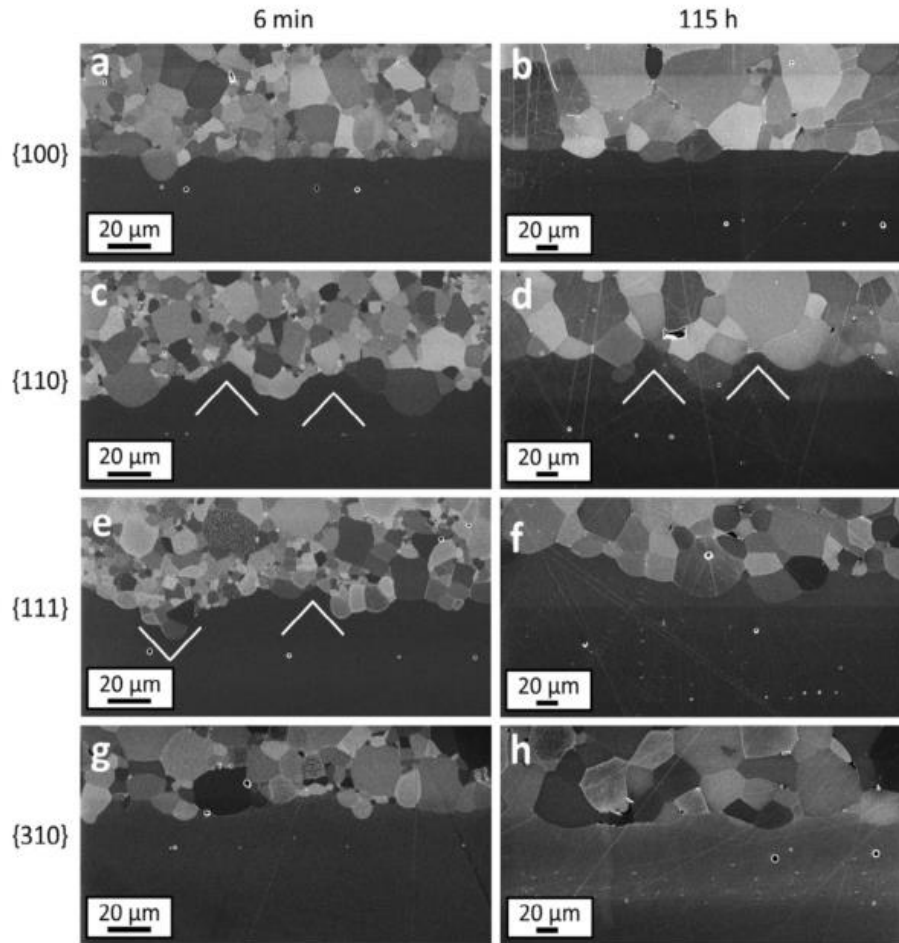


Figure 1-27: Images showing SrTiO₃ single crystals growing into polycrystals. Single crystal interfaces of {100}, {110}, {111} and {310} annealed for 6 minutes and 115 hours. Grain boundary structure changes with single crystal orientation showing both faceted and non-faceted grain boundaries[53].

1.4.2 Linking Equilibrium Crystal Shape to Grain Growth Via Grain Boundaries

1.4.2.1 Wulff Shape and Equilibrium Crystal Shape

The equilibrium crystal shape is the geometric shape an isolated mass of material will take if unconstrained and at equilibrium to minimize its total surface energy. The shape can be determined by a process referred to as the Wulff construction [54]. The Wulff construction requires a known polar plot of the surface energy as a function of orientation for a material. For each orientation a line is drawn from the origin of the plot until it intersects the surface energy for that orientation. At the intersection a tangent line to the surface energy is drawn and this

process is repeated at each orientation. This process creates an inner envelope which none of the tangent lines extend into, the shape of the inner envelope is the Wulff shape or equilibrium crystal shape, Figure 1-28. Due to the nature of the Wulff construction the edges of the Wulff shape must either be flat or convex. As it is difficult to measure the surface energy of a system and few measurements exist, the equilibrium crystal shape is commonly determined through the observations of isolated pores of a material. It should be noted that it is not possible to extract the surface energy as a function of orientation from the equilibrium crystal shape as there is not a unique solution. Multiple surface energy plots will yield the same equilibrium crystal shape [54]. A minimum surface energy as a function of orientation plot can be constructed from the equilibrium crystal shape, but it does not preclude the existence of other higher energy plots.

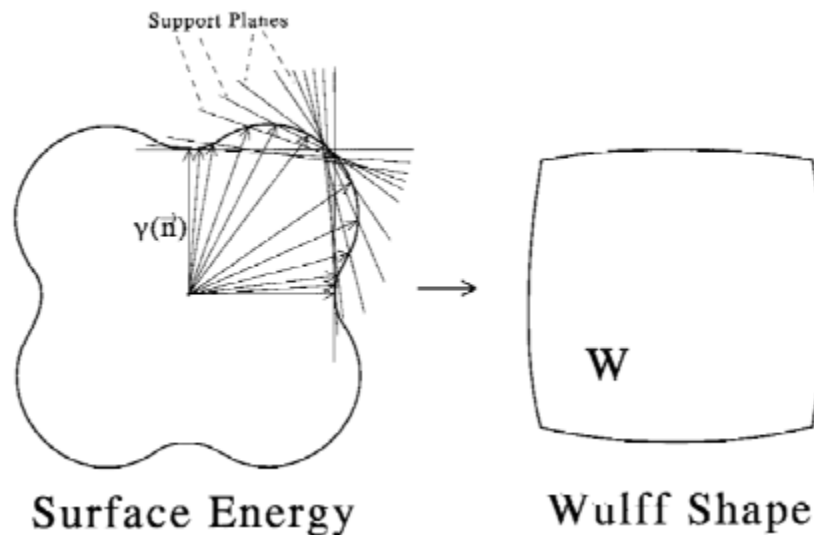


Figure 1-28: Schematic of (a) Wulff construction and (b) Wulff shape or equilibrium crystal shape[55].

While the equilibrium crystal shape cannot be used to calculate a definitive polar plot, it provides information about the faceting behavior of a system. All orientations within smoothly curved regions also called rough regions on an equilibrium crystal shape correspond to stable orientations. Flat regions of the equilibrium crystal shape are faceted and called smooth regions. Shown in Figure 1-29, the faceting behavior of a flat region depends on its boundary conditions. Take orientation n_{gb} with an orientation that falls on the top flat surface of the equilibrium crystal

shape but not on the stable (0001) orientation. The n_{gb} orientation is not one of the stable low energy orientations; therefore, it will break up into a faceted surface containing the (0001) and n_{edge} planes, which are stable and border the unstable orientations. The surface area ratio of (0001) facet and n_{edge} facet is determined by the proximity to the boundary stable orientations. Orientations closer to (0001) will have a larger surface area of (0001) facet with corresponding smaller surface area of n_{edge} .

Edges or transitions from one stable facet to another take on several different forms. The transitions can be either first order discontinuous or second order continuous transitions. First order transitions, as shown in Figure 1-30 (a-b) have a discontinuous jump between stable orientations resulting in some orientations that no longer exist and are known as missing orientations. At the meeting of two flat regions, each having a stable orientation, the orientations between the two stable orientations do not exist. For example, from Figure 1-29 orientations between (0001) and n_{edge} are missing orientations. Missing orientations occur similarly when a faceted region meets a rough region in a first order transition. If, however, a faceted region meets a rough region and is a second order or continuous transition, there are no missing orientations. In this case (0001) and n_{edge} have the same orientation at the transition from the faceted region to the rough region and no orientations are missing.

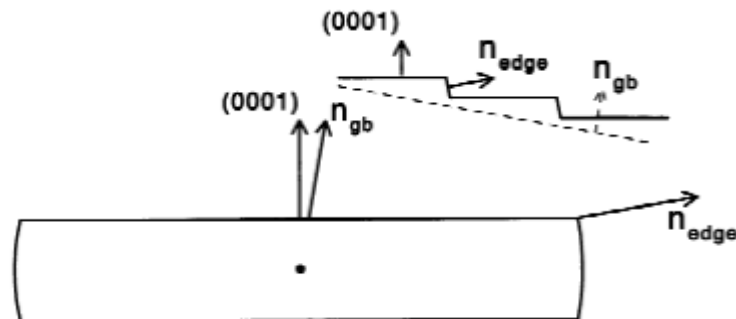


Figure 1-29: Schematic for elongated equilibrium crystal shape of aluminum sample showing unstable orientations devolving into stable boundary orientations[55].

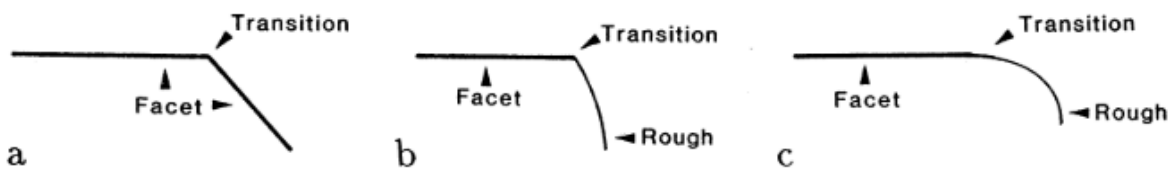


Figure 1-30: Schematic showing (a-b) first order transitions between faceted and rough regions resulting in missing orientations and (c) a second order transition between facet and rough regions with no missing orientations[54].

The equilibrium crystal shape of a material is known to be altered by variables like temperature and chemical potential. As the temperature of a material is increased, the surface area of the equilibrium crystal shape corresponding to a rough surface increases. Increase in temperature causes the entropy to increase, allowing for more orientations to become stable, resulting in an increasingly rough surface area on the equilibrium crystal shape. Taken to the limits eventually all equilibrium crystal shapes will become spherical at a high enough temperature as shown in Figure 1-31. The changing equilibrium crystal shape as a function of temperature manifests itself into what is commonly known as a faceting transition temperature or sometimes called a roughening transition where at a critical temperature, grain boundaries change from faceted to rough and if cooled changed from rough to faceted [56].

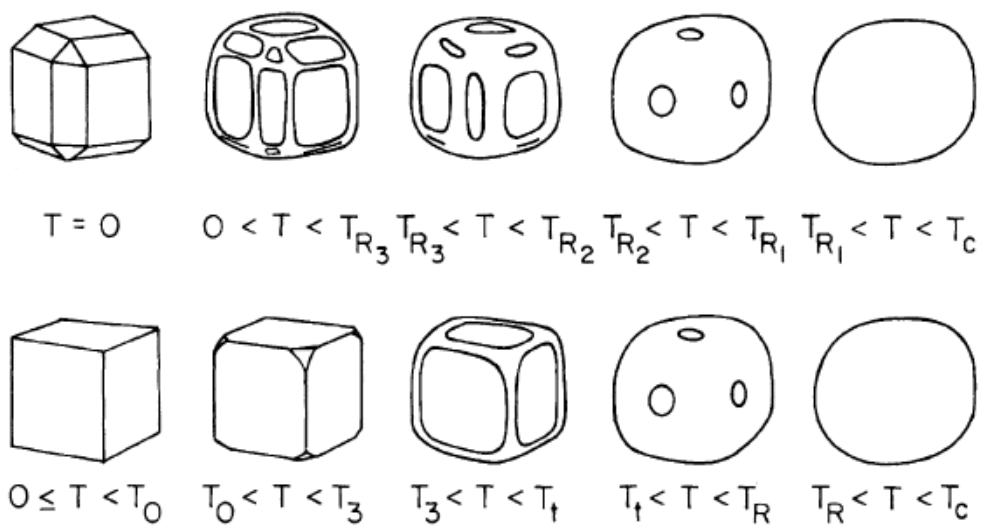


Figure 1-31: Schematic showing increasing rough surface area of an equilibrium crystal shape with increasing temperature for two equilibrium shapes[56].

1.4.2.2 The Grain Boundary Plane Distribution

As it has been determined that the structure of the grain boundary plays an influential role in the final grain boundary properties, recent work has focused on developing a method to characterize the grain boundary plane distribution and the role of orientation. As discussed prior, the 5 independent parameters are required to identify a grain boundary [56]. The misorientation across the grain boundary provides 3 parameters easily obtainable through EBSD measurements. The 2 parameters needed to define the grain boundary plane orientation are difficult as the plane is buried within the sample. Increasing the difficulty is that a grain boundary with a fixed misorientation may be made from multiple segments, each with their own grain boundary orientation[56].

A large effort by Rohrer et al. [44] has developed a method to overcome these challenges and measure the 5 grain boundary parameters to produce a grain boundary plane distribution. The process starts by taking each grain boundary in a data set and segmenting it. Each grain boundary is broken into more and more segments until each segment fits to the grain boundary within a set tolerance. With each grain boundary now defined by a number of segments, each segment has its trace calculated. The trace is simply the direction of the segment giving 1 parameter of the grain boundary plane orientation. Statistically, this process is repeated for all segments in the entire data set. Each segment has a trace direction and a misorientation assigned to it, 4 parameters.

For each trace segment, the orientation of the grain boundary can be any perpendicular vector, Figure 1-32. The trace direction for a segment is plotted on a stereographic projection and all the possible grain boundary plan normals appear as a curved line on the plot, Figure 1-33. The curved line of all possible grain boundary normals is plotted upon the same stereographic projection, Figure 1-34. The possible curves will intersect at a point and that point is the grain boundary normal, the 5th parameter needed. Using this method for a large data set the grain boundary plane distribution can be calculated for a material as have been done for Ni [57] and MgO [58].

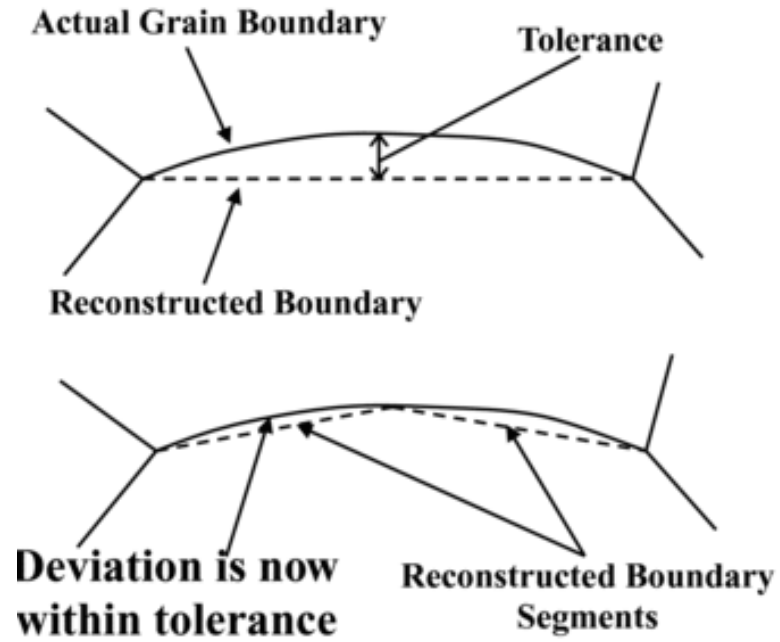


Figure 1-32: Schematic showing grain boundary trace segment formation until tolerance is complete[59].

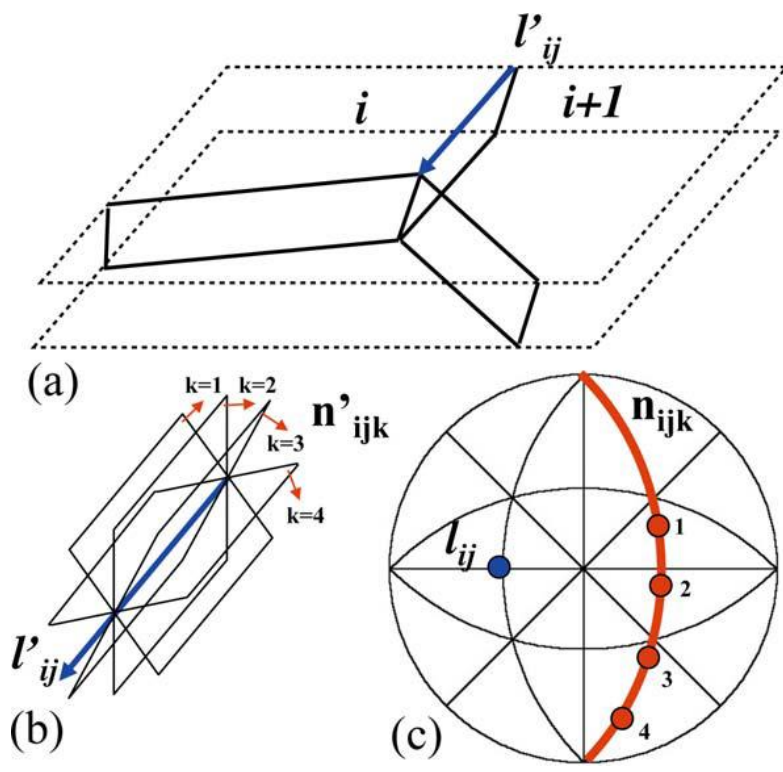


Figure 1-33: Schematic showing (a) grain boundary trace, (b) possible orientations of the grain boundary of a single trace and (c) grain boundary trace and possible grain boundary orientations plotted on a stereographic projects[59].

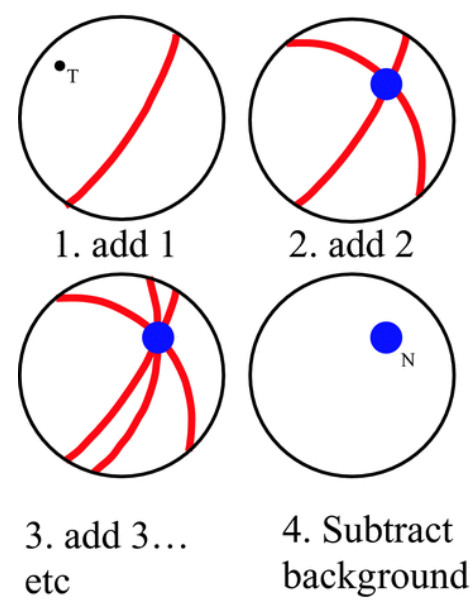


Figure 1-34: Schematic demonstrating the identification of the grain boundary orientation by the accumulation of trace orientations intersecting at a single orientation[59].

The boundary plane distributions calculated from large data sets for Ni and MgO were compared with the calculated grain boundary energy distribution, Figure 1-35 and 1-36. An inverse relationship was found, with grain boundary planes that showed up with a higher than average frequency were grain boundaries that had the lowest energy [44]. Going further the grain boundary plane distribution was compared to the surface free energy and found the same inverse relationship. Grain boundary planes that were measured with higher than average frequency were the same planes with low surface energy. From these inverse relationships, it was determined that when grain boundaries bind and restructure, minimizing their energy, grain boundaries favor configurations that preserve orientations with the low surface energy. Therefore, surfaces with low surface energy dominate the grain boundary restructuring process by keeping their surface structure while forcing the other surface to restructure.

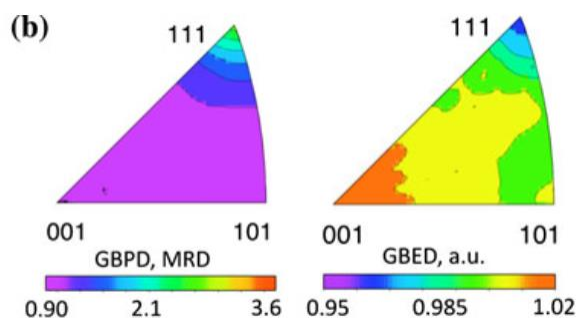


Figure 1-35: Inverse pole figures for Ni showing the grain boundary plane distribution and grain boundary energy distribution having an inverse relationship. [57]

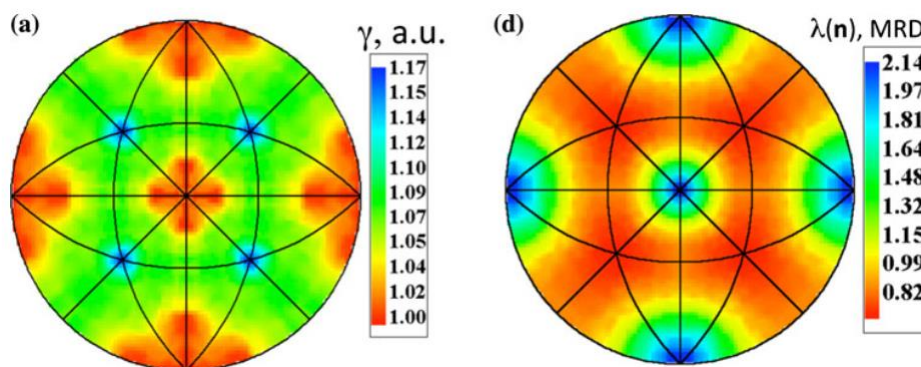


Figure 1-36: Pole figures for MgO showing surface energy and grain boundary energy distribution having an inverse relationship [58]

The low energy surfaces that dominate the grain boundary restructuring process were determined and found to correlate to those found on the equilibrium crystal shape. This indicates that the grain boundary plane distribution and the high frequency planes are determined by a materials equilibrium crystal shape. The equilibrium crystal shape determines what orientations are stable, thereby determining what high frequency grain boundary planes will form for a material system.

1.4.2.3 The Hypothesis: Linking the Equilibrium Crystal Shape to Grain Growth

Work done by Rohrer et al. discussed in 1.4.2.2 showed evidence that the grain boundary plane distribution was correlated with the equilibrium crystal shape. High frequency grain boundary planes corresponded to the low energy planes. The low energy planes correspond to the low energy, stable planes determined from the equilibrium crystal shape. Therefore, by altering the equilibrium crystal shape one can alter the grain boundary plane distribution by altering what are the stable low energy planes for a material.

In 1.4.2.1, it was discussed how grain boundaries of different structures, such as faceted and not, exhibit different migration behavior during grain growth. Therefore, it is hypothesized to be possible to influence what grain boundary planes form by controlling the equilibrium crystal shape, and in turn altering the grain boundary plane distribution will alter the grain growth behavior of a system. The equilibrium crystal shape may be a possible mechanism to control grain growth in a system provided you can control the equilibrium crystal shape.

1.5 The NiO-MgO System

A correlation between the stable surface orientations from the equilibrium crystal shape, the grain boundary plane distribution and grain growth behavior were highlighted in section 1.4. The general hypothesis of the original work presented in this document was that the controlling the equilibrium crystal shape and its stable orientations could be used as a mechanism to control the microstructural evolution and grain growth in a material through alterations of the grain boundary plane distribution. To experimentally test this hypothesis a material where the equilibrium crystal shape is controllable and the ability to isolate the effect of the changing equilibrium shape was needed. The NiO-MgO alloy system was selected.

1.5.1 Equilibrium Crystal Shape of NiO-MgO Alloys

The equilibrium crystal shape of the NiO-MgO alloy system was studied by Handwerker et al. [60]. NiO-MgO powder was produced by mixing NiO and MgO powders and annealing at 1500°C for 55 hours. The equilibrium crystal shapes were then estimated from SEM images. It was determined the equilibrium crystal shape of MgO was cubic with (100) stable orientations. With low nickel concentrations, less than 5%, the equilibrium crystal shape remained cuboidal with the presence of (100) facets; however, sharp corners degraded into smoothly curved corners between the (100) facets with second order transitions. The (100) facet size decreased with increasing nickel content, up to 10%, resulting in the smoothly curved regions growing in area and the equilibrium crystal shape becoming spherical. Nickel content between 10% and 60% see the (100) facet size increasing, however with sharp first order transitions. The rough region was suggested to form a (110) stable facet causing the first order transition with the (100) as opposed to a secondary transition observed with less than 10% nickel content. Increasing nickel content above 60% led to the formation of (111) stable facets. The (111) facets continued to grow in size with increasing nickel content, overtaking all other stable facets. Pure NiO was observed to have only stable (111) facets forming an octahedral structure. The above description of the equilibrium crystal shape of NiO-MgO is shown in Figure 1-37, showing a 3D view as well as cross sections about the (100) and (111). Figure 1-38 shows 3D representations with corresponding SEM images from which they were estimated. The work by Handwerker et al. [60] show that in the NiO-MgO system the equilibrium crystal shape is a function of the alloy compositions. It was observed that facets stable at one composition were replaced with another facet as the composition varies. The (100) facets dominate at low nickel content, the (110) facet forms at intermediate alloy compositions and (111) facets dominating at high nickel content.

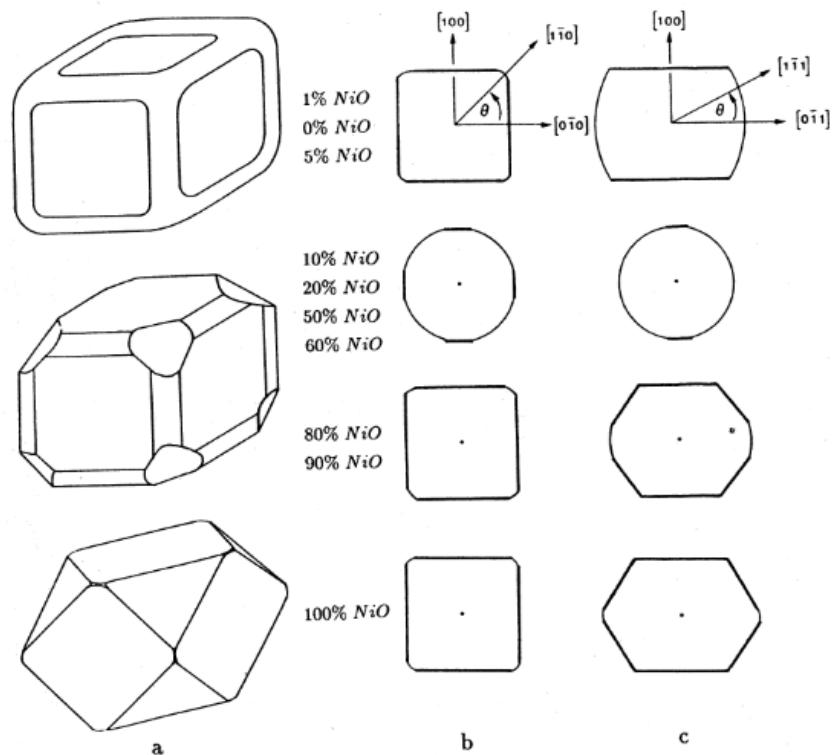


Figure 1-37: Schematic of equilibrium crystal shape of NiO-MgO alloys (a) in 3D, (b) cross section along (100) axis and (c) (110) axis. [60]

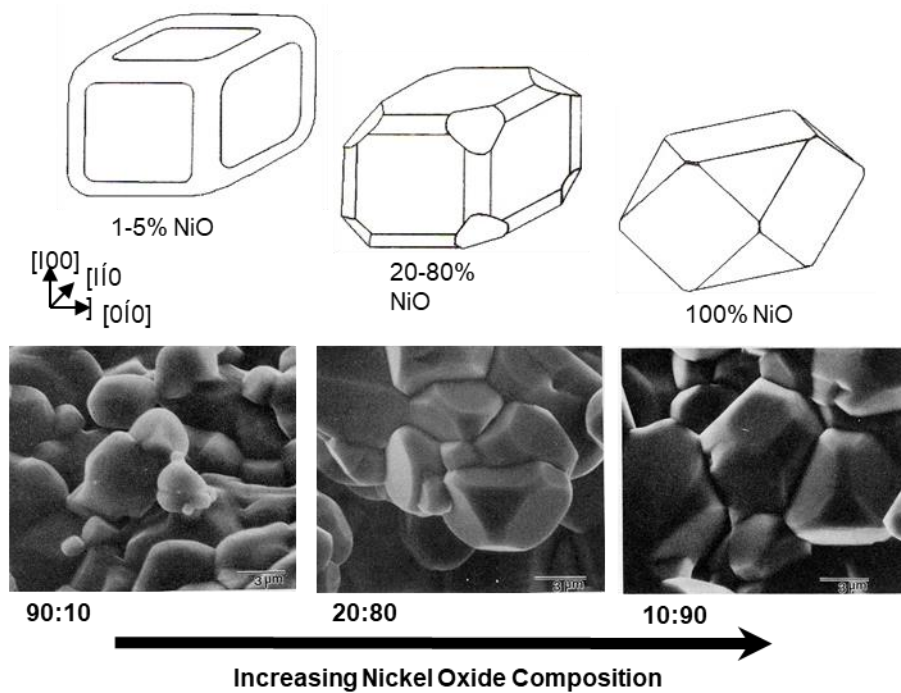


Figure 1-38: Schematic showing NiO-MgO 3D equilibrium crystal shapes extrapolated from SEM images. Recreated from [60].

1.5.2 Other Characteristics of NiO-MgO System

The NiO-MgO alloy system offers the ability to test the equilibrium crystal shape's effect on grain growth with the equilibrium crystal shape being a function of composition. However, the NiO-MgO system offers other benefits to isolate the effect of the changing equilibrium shape. The rock salt crystal structure NiO-MgO system is a single phase solid solution, Figure 1-39. The nickel and magnesium share the same lattice sites in the rocksalt unit cell. Nickel and magnesium have similar atomic radii with 200 pm for nickel and 173 pm for magnesium, resulting in only minimal changes to the lattice parameter from site to site. The nickel and magnesium carry the same charge, making NiO-MgO an isomorph. Being isomorphous is ideal for this, work as changing the ratio of nickel and magnesium will not alter the behavior of the material except for the equilibrium crystal shape. NiO-MgO also has no solubility with other elements, resulting in any impurities forming precipitates.

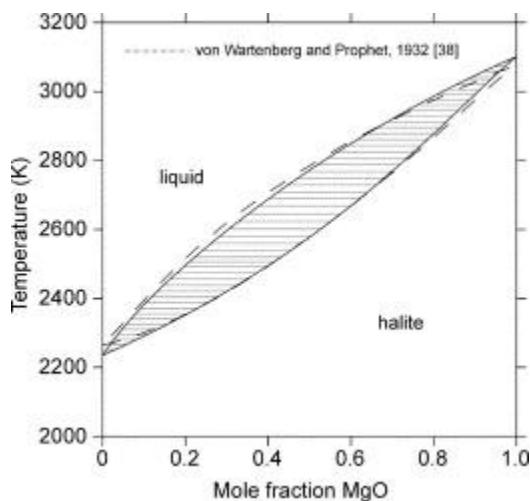


Figure 1-39: Phase diagram for NiO-MgO system. [60]

The NiO-MgO system being isomorphous and having no solubility with other elements makes the NiO-MgO system ideal for isolating the effect of a changing equilibrium crystal shape. Solute drag is minimized as impurities will precipitate out of the system instead of segregating to the grain boundaries and forming chemical gradients. Nickel and magnesium single phase isomorphism results in a dispersed mixed oxide and, if mixed well, a chemically homogenous material. These factors allow for the isolation of the effect of the changing

equilibrium crystal structure on grain growth. For these reasons the NiO-MgO system was selected for use in the original work reported in this study.

2. NIO-MGO POWDER PRODUCTION AND CHARACTERIZATION

2.1 Introduction

The NiO-MgO system was selected to investigate the effect of surface energy anisotropy as its equilibrium crystal shape is a function of composition as discussed in Chapter 1. As NiO-MgO alloys are not commercially available, the powders were fabricated. To isolate the effect of changing surface energy, powder properties needed to be strictly controlled to produce an ideal powder. To minimize the effect of impurity drag on grain boundaries, ideal powders require the removal of all impurities. As it is impossible to remove all impurities, the starting raw materials must have the highest purity possible. Continuing the process by which the NiO-MgO powders are produced must minimize any possible source of contamination to retain the purity of the raw materials. Ideal powders will need small particle sizes. Smaller particles improve the sintering and densification as discussed in chapter 1. The ideal particle shape is roughly spherical as particle geometries such as platelets or fibers do not pack well [61], reducing the green body density of produced pellets. The ideal powder must also be compositionally homogeneous. Compositional gradients in the powder, as discussed in Chapter 1 can result in drag terms which affect the grain growth behavior of a material and must be eliminated. Therefore, the powder production method needed to meet the following criteria:

1. Produce powders that minimize impurity content thereby maintain the purity of the raw materials
2. Produce powders with small particle size, ideally less than 100 nm
3. Produce powders that have homogeneous compositions with no compositional gradients

NiO-MgO alloy powders were produced using both mechanical and chemical production routes and the resulting powders were characterized and compared.

2.2 Mechanical Alloying

2.2.1 NiO-MgO Mechanical Alloying Process

Mechanical alloying is a solid-state powder processing method that repeatedly welds and fractures powder particles [62]. The alloying process mixes dry powders and milling media made of inert material in a high energy mechanical mill, Figure 2-1. Powder particles are crushed

between the milling media, welding powder particles together. Particles increase in size as more particles are welded together and the shear stress experienced by the particles increases with size [63]. Particles exposed to critical levels of shear stress fracture, producing smaller particles. As small particles are welded and grow and larger particles fracture and shrink, an intermediate average size is reached, Figure2-2. The process of welding and fracturing is repeated, producing a dispersed oxide particulate.

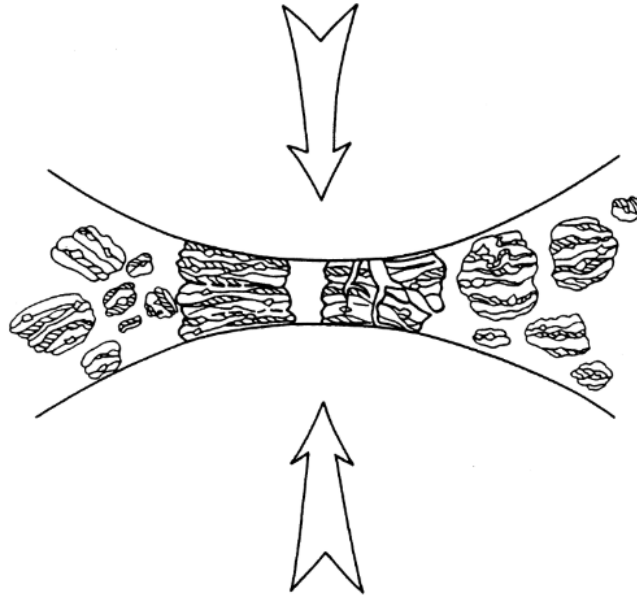


Figure 2-1: Schematic drawing showing powder welding and fracturing experienced during mechanical alloying. The schematic shows a powder mixture of two distinct chemical compositions [62].

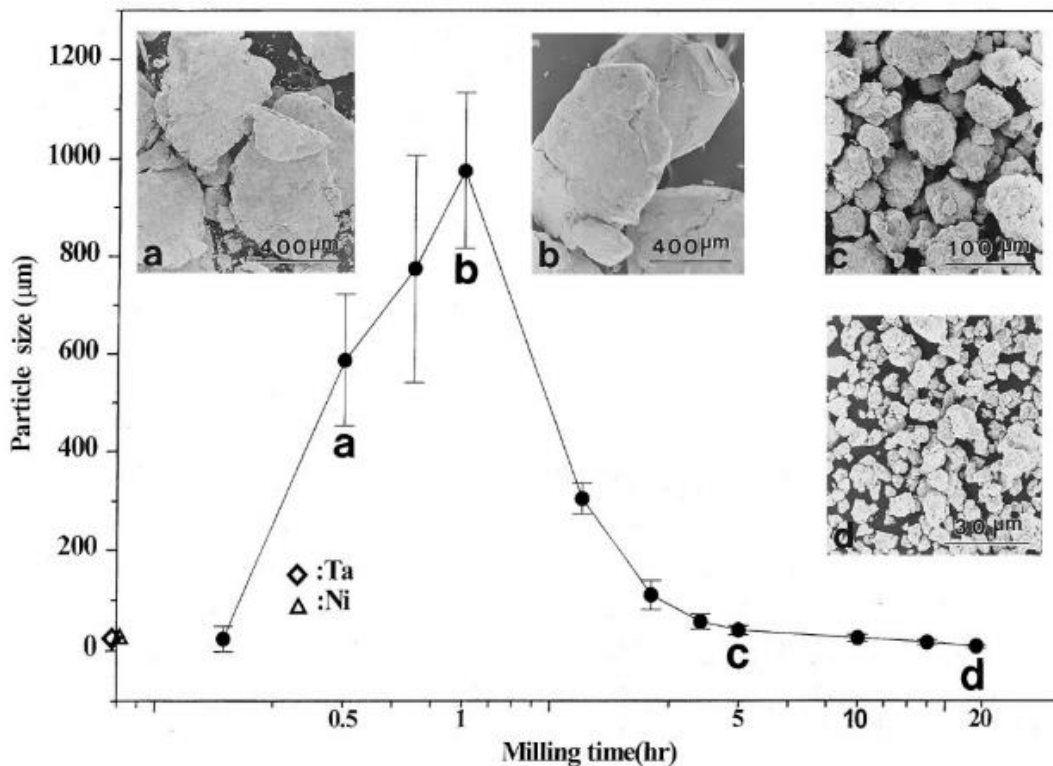


Figure 2-2: Graphical figure showing particle size increases initially during mechanical alloying as small particles weld together. As particles continue to grow and shear forces increase, they will reach a critical mass a fracture. During mechanical milling as, small particles weld and grow, large particles fracture and a stable intermediate particle size is reached. [62]

Double mechanical alloying adds a heat treatment and second milling step to the mechanical alloying process [63]. Alloyed powders are heat treated at temperatures allowing for diffusion to occur. Diffusion in the alloyed powders removes any remaining compositional gradients, homogenizing the system. Once the alloyed powder has a homogeneous composition, the powder undergoes a final milling step. The final milling step is used to manipulate the particle size of the powder to achieve the desired size and distribution.

Five NiO-MgO alloys with compositions having Ni:Mg ratios of 100:0, 75:25, 50:50, 25:75, 0:100 were produced. Powders were produced by mixing respective amounts of commercially purchased NiO and MgO powders with purities of 99.99%. Mechanical alloying is known to have impurity contamination; therefore, extensive work was done optimizing the double mechanical alloying process. The following variables were tested and adjusted with the objective to minimize the impurity contamination throughout the process:

- Milling media and jar chemical composition (stainless steel and yttria stabilized zirconia)
- Milling media geometry (balls and beads)
- Milling media size (0.05-2mm)
- Milling media to powder filling ratio (1:2, 1:1, 2:1, 3:1)
- Milling jar fill (40-70%)
- Milling environment (dry, water, ethanol)
- Planetary mill rotations per minute (100-300 rpm)
- Mechanical alloying duration (30 minutes to 4 hours)
- Milling jar temperature (less than 100°C)

The optimal milling conditions had NiO-MgO alloys mechanically alloyed in a planetary mill with yttria stabilized zirconia milling media for 2-hour segments at 250 rpm with a dry environment to prevent heating concerns. Beaded milling media with a diameter of 1mm was used. Alloyed powders were then heat treated at 1500°C for 5 hours in atmospheric conditions to chemically homogenize the powders. The temperature and time were selected based on prior work done by Handwerker et al. [60] Powders were characterized using XRD to determine their compositional homogeneity. If powders were not homogeneous, the powders repeated the double mechanical alloying process. Powders were considered complete when compositional homogeneity was achieved.

2.2.2 Mechanical Alloyed Powder Characterization

2.2.2.1 Mechanical Alloyed Powder Compositional Homogeneity

NiO-MgO alloy powder compositional homogeneity was characterized using XRD. Starting powder mixtures contained NiO and MgO resulting in two distinct set, of XRD peaks matching XRD standards. Powders undergoing the mechanical alloying process were expected to see the two peaks merge. If XRD measured two peaks after the double mechanical alloying process, the powder was deemed incomplete and repeated the double mechanical alloying process. XRD analysis of alloyed powders showed that full homogenization of the NiO and MgO powders took 4-5 iterations of the double mechanical alloying process.

2.2.2.2 Mechanical Alloyed Powder Impurity Level Characterization

The main source of contamination occurs during the mechanical alloying and milling steps, during the milling process, as the powder is crushed between the milling media and the milling media and milling jar. This is an abrasive process that damages the media and jar, grinding down their surfaces. The material ground off the media and jar become part of the powder, resulting in increasing impurity contamination for longer times and higher energy milling. The damage to the media and jar was measured by massing the media and jar before and after the alloying and milling stages. The composition of the alloyed powder was recalculated to include the missing mass from the jar and media.

Even with extensive optimization, the mechanical alloying stage contributed significant impurity contamination. Mechanical alloying requires high energy milling, resulting in significant damage to milling media and milling jar. Impurity concentrations calculated for mechanical alloying stage ranged from 2.3-5.4 atomic percent of final alloyed powders. The high contamination rate was also due to multiple iterations of the double mechanical alloying steps required to achieve the desired powder homogeneity. An impurity level less than 1% was the desired objective and mechanical alloying did not meet this requirement. Subsequently mechanical alloying powder production was abandoned as a viable method to produce NiO-MgO alloy powders. Other mechanical milling options were pursued; however, none were able to overcome the contamination problem and focus shifted to chemical production methods.

2.3 Amorphous Citrate Chemical Production

2.3.1 Amorphous Citrate Production Process

The chemical production path for NiO-MgO powders was developed based on the amorphous citrate process reported by Marcilly et al. [64] to produce mixed oxides. Marcilly et al. process mixed metallic salts with a polyfunctional organic acid. The mixture contained the desired ratio of metallic cations in the final mixed oxide powder. The mixture was heated in a vacuum rotary evaporator and rapidly dehydrated. As dehydration occurred, the viscosity of the mixture increased. Upon cooling, the viscous melt forms an amorphous solid foam separated into cells. The cells contained the homogeneously mixed metallic salts, which crystallized. The foam

structure was then calcined at a selected temperature, allowing for the metal salts to react and form the desired material phase of mixed oxide.

Modifications were made to the process developed by Marcilly et al. to produce NiO-MgO alloy powders. Powder mixtures containing $\text{Ni}(\text{NO}_3)_2 \cdot 6\text{H}_2\text{O}$ and $\text{Mg}(\text{NO}_3)_2 \cdot 6\text{H}_2\text{O}$ with the desired ratio of Ni and Mg were created. Citric acid was used as the polyfunctional organic acid, with an equal molar concentration of the combined Ni and Mg metallic cations. The powder mixture was melted and dehydrated in a vacuum rotary evaporator at 70°C with a pressure of 0.7 kPa. Dehydration occurred over the period of 30 minutes and the melt was transferred to a MgO crucible and allowed to cool, forming the foam structure. Based on work developing NiO-MgO as a catalyst [65]–[67] a two-step calcination process was developed. The foam was heated with a heating rate of $5^\circ\text{C}/\text{min}$ and held at 170°C for 1 hour. This step completed the dehydration of the foam and activated the polyfunctional acid, causing it to expand with the formation of gasses. The foam was then heated to and held at 500°C for 3 hours to complete the calcination process. Five base NiO-MgO alloy powders were produced using this method having the following ratios of Ni:Mg, 100:0, 75:25, 50:50, 25:75, 0:100.

2.3.2 Amorphous Citrate Powder Characterization

Powders produced by the amorphous citrate process containing Ni 100:0, 75:25, 50:50, and 25:75 Ni:Mg were colored black. The 0:100 Ni:Mg powder were colored white. It was expected that the resulting powders would be on a color scale from green to white with reducing levels of Ni. The cause for the unexpected black colored powder was investigated. Based on work done by Renaud et al., it was determined that alloy powders containing Ni had a non-stoichiometric level of oxygen [68]. This was caused by the gas formation in the foam during the calcination process, creating a low-level reducing environment. The Ni containing powders, when heated to 1000°C with no hold, took on the expected green color as the oxygen content was restored to stoichiometric levels, Figure 2-3.

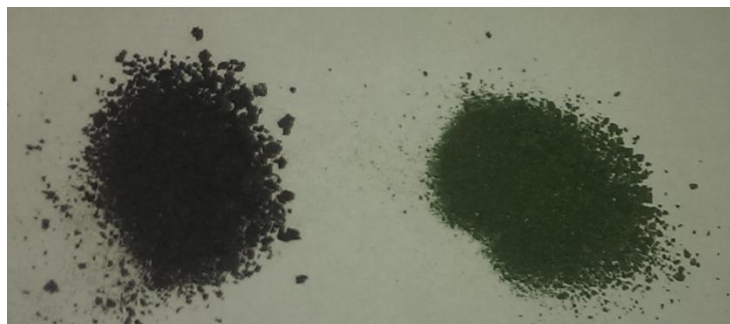


Figure 2-3: Images taken of powder before (left) and after (right) 1000°C step showing the color transition from black to green with the restoration of oxygen in the powder to stoichiometric levels.

2.3.2.1 Compositional Homogeneity

The compositional homogeneity of amorphous citrate produced powders were determined using XRD. Pure NiO and MgO powders were produced and used as a reference for NiO-MgO alloys peak identification. Powders were classified as homogeneous if the following criteria was met.

- Pattern and identified peaks matched that of the pure NiO and MgO patterns
- NiO and MgO 2θ peak positions corresponded to XRD standards
- NiO-MgO alloy peak 2θ values corresponded to an extrapolation of peak location between the NiO and MgO peaks based on the ratio of Ni and Mg cations.

XRD analysis of the five base powders measured five distinct homogeneous patterns, Figure 2-4 (a). Peaks' 2θ position was determined to correspond to the ratio of Ni and Mg present. As a base powder's ratio of Ni and Mg is varied from 100% Ni to 100% Mg the peak positions shifted to higher 2θ values, moving from a NiO peak to a MgO peak. Peak positions for 75:25, 50:50 and 25:75 Ni:Mg powders corresponded to the expected 75%, 50% and 25% Ni 2θ values for a linear extrapolation between the NiO and MgO peaks, Figure 2-4 (b). It was concluded that the powders produced using the amorphous citrate method were homogenous powders meeting the set criteria.

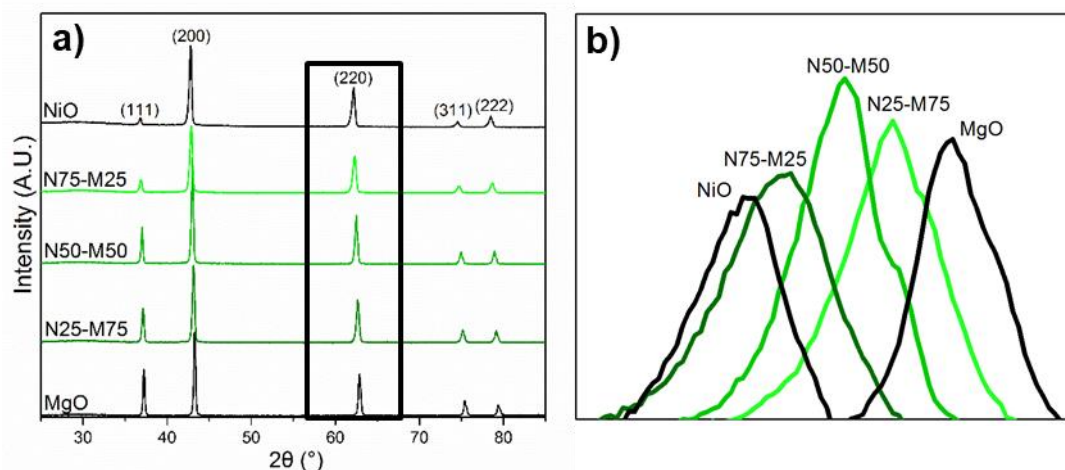


Figure 2-4: X-ray diffraction patterns (a) five compositions of NiO-MgO with Ni to Mg ratios of 100:0, 75:25, 50:50, 25:75, 0:100, (b) (220) peak highlighting formation of distinct peaks for each alloy, ranging from pure NiO to pure MgO, following a linear extrapolation of the peak position.

2.3.2.2 Particle size and Morphology

The morphology and particle size of the five produced base powders were characterized with XRD and SEM. From XRD patterns measured for each of the five compositions, the particle size was estimated using Scherrer's equation [69], equation 10. λ is the wavelength of the Cu radiation, β is the full width half max, θ is the Bragg angle and K is the shape factor, for which a value of 0.9 was selected from literature [69]. Calculated values shown in Table 2-1 show an increasing crystallite size with increasing Ni content, going from 244-393 nm

$$\tau = \frac{K\lambda}{\beta\cos(\theta)} \quad (10)$$

Table 2-1: Calculated Scherrer Crystallite Size

Composition NiO-MgO	Crystallite Size (nm)
N0-M100	244
N25-M75	280
N50-M50	328
N75-M25	350
N100-M0	393

Particle morphology was investigated and NiO-MgO powders produced following the amorphous citrate method showing platelet-like particles. Further investigation of the produced powders discovered the formation of large hard plate-like agglomerates. While crystallite size calculated from Scherrer equation ranged from 244-393 nm, hard agglomerates in the base powders range from 20-300 μm in size, Figure 2-5. The hard agglomerates were multigrain, fully dense and made of multiple layers of grains initially, Figure 2-6.

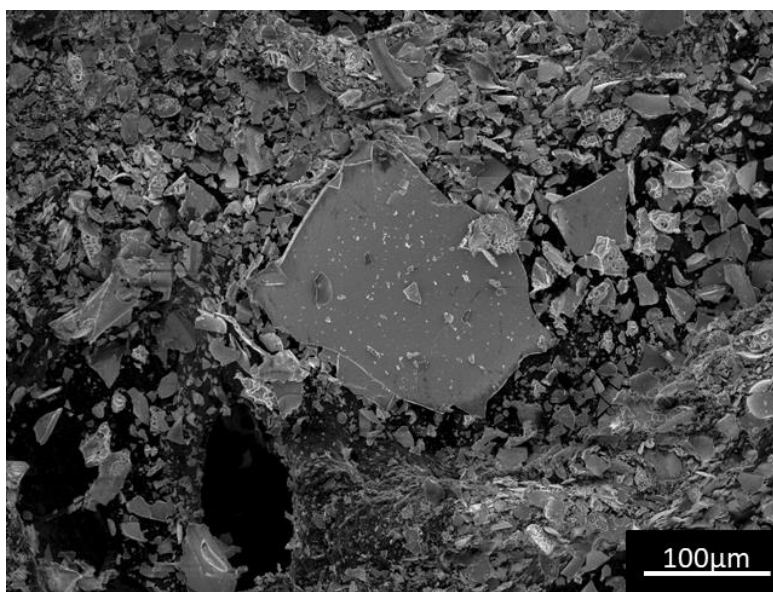


Figure 2-5: SEM micrograph of particle plate like morphology large agglomerate forming from amorphous citrate process with sizes greater than 300 μm s in a 75:25 Ni:Mg powder.

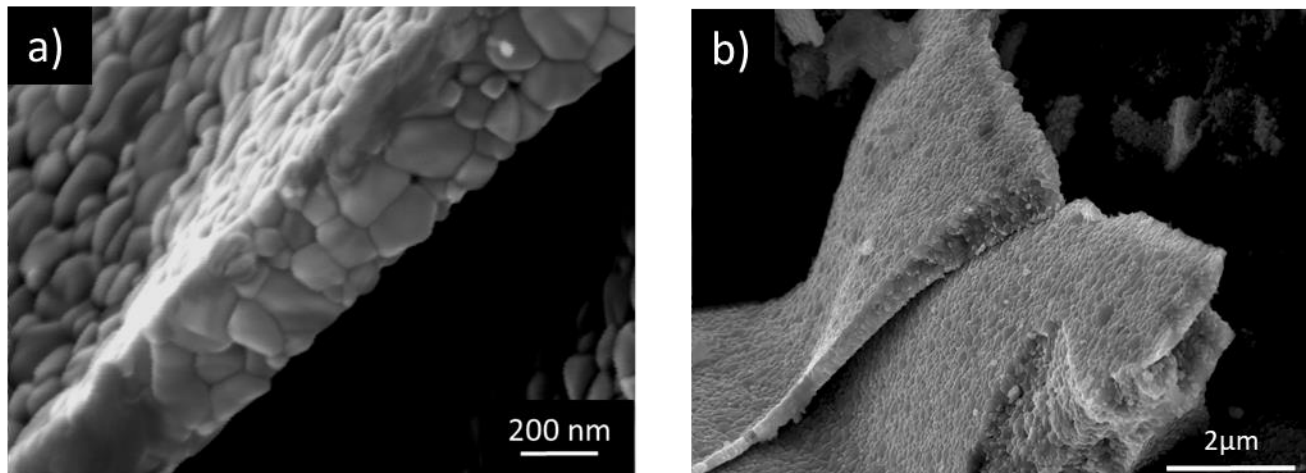


Figure 2-6: Sem micrographs of multigrain, multilayer agglomerate structures resulting from amorphous citrate process in a) 75:25 Ni:Mg powder, b) 50:50 Ni:Mg powder.

2.4 Powder Morphology and Size Distribution Alteration

The five base powders produced using the amorphous citrate method met two out of three of the criteria for a successful powder production process. The powder produced was compositionally homogenous and did not induce any impurity contamination. The powder particle size, however, was larger than desired. Attempts were made to break up the larger agglomerates through forms of mechanical milling. As described earlier in this chapter, there exists a contamination penalty when mechanically milling and it increases with higher energy milling and longer milling times. Attempts at hand milling using a mortar and pestle and low energy ball milling was attempted. Neither milling process was sufficient to break the hard agglomerates. It was determined through trials that any mechanical milling intense enough to break up the hard agglomerates introduced more than 1% atomic percent contamination. Therefore, it was unviable to break the hard agglomerates post-production.

Alterations to the amorphous citrate process were attempted to minimize the formation of the large hard agglomerates. Heating and cooling rates were increased to 10°C/minute with the objective to thermally shock the agglomerates causing them to fracture. This was taken further, using 20°C/minute heating and cooling rates. Referencing NiO-MgO catalyst literature [70], [71] the amount of citric acid was increased and decreased. The second dehydration step at 170°C was skipped. The best result was increasing the amount of citric acid by 10% and heating rates to

10°C/minute, resulting in the largest hard agglomerate found being reduced to 150 μm in diameter.

2.5 Final Comments on NiO-MgO Powder Production

Production of NiO-MgO alloy powder via double mechanical alloying and amorphous citrate processing routes were discussed. Despite extensive optimization and variable configurations, NiO-MgO alloy powders produced using mechanical alloying suffered unacceptable impurity contamination. Contamination of 2.3-5.4 atomic percent would have resulted in any grain growth measurements being influenced by significant impurity drag forces and possible precipitate pinning as yttria-stabilized zirconia is not soluble in NiO-MgO. The double mechanical alloying process did produce homogenized NiO-MgO alloy powders; however, with high contamination levels, using the process to produce NiO-MgO powders was abandoned.

NiO-MgO alloy powders produced via the amorphous citrate route did, however, produce viable powders. Amorphous citrate powders were homogenous and the process itself did not contaminate the powders with impurities. The measured particle size was larger than desired, and the particle morphology was undesirable platelets. Worse, the formation of large hard agglomerates up to 300 μm in size was measured. Process alteration through the addition of 10% more citric acid and higher heating rates did reduce the size of the hard agglomerates, with the largest ones being less than 150 μm in size down from 300 μm . Exploration of the NiO-MgO literature offered no alternative processing routes. Therefore, it was concluded that NiO-MgO alloy powders produced via the amorphous citrate method were acceptable and would proceed to sintering and densification trials.

3. SINTERING AND DENSIFICATION OF NIO-MGO ALLOYS

3.1 Introduction

To perform grain growth studies in the NiO-MgO system and measure the effect of changing surface anisotropy, bulk polycrystalline samples were needed. Five NiO-MgO alloy powder compositions were produced: 100:0, 75:25, 50:50, 25:75 and 0:100 Ni:Mg. The powder production method was described in Chapter 2. The five powder compositions would undergo shape forming and sintering to produce samples. To isolate the effect of changing surface anisotropy on grain growth ideal, fully dense samples were needed. Ideal fully dense samples are defined by the following conditions:

- Retain the purity and compositional homogeneity of the powders produced using the amorphous citrate production method.
- Samples need to achieve a high density, ideally reaching 100% of their theoretical density, referred to as fully dense.
- Samples need to minimize grain growth during sintering, allowing for a smaller grain size when starting grain growth studies.
- Final sample microstructure needs to be free of microstructure features that act to impede grain growth, such as open and closed porosity and impurity precipitates, resulting in large regions of clean microstructure.

To form and sinter the five NiO-MgO alloy powders to meet the ideal requirements, extensive testing of forming techniques and sintering process variables and sintering techniques was carried out and is reported in this chapter.

3.2 Ceramic Powder Formation

Ceramic powder shape formation can be done by various dry and wet techniques discussed in greater detail in Chapter 1. Dry forming techniques are simple and effective at producing large quantities of both small complex and simple shapes with high tolerances. Dry forming processes are limited in that they inherit many properties of the powder being used. The

particle size and geometry limit the packing and resulting density uniformity of produced green bodies. Powder impurities are carried from the powder to the green body. Sample defects may occur during formation and later during sintering due to non-uniform pressure during formation, resulting in stress gradients within the sample. While limited by the powder used and having known defects, dry forming techniques can be used without using any additives to the powder, limiting any further contamination, which is advantageous to this body of work.

Wet forming techniques generally function using ceramic slurries. Techniques such as tape casting and slip casting can form complex shapes, however include a drying step. The slurries are formed by mixing ceramic powders with liquids, commonly water and additives. Additives such as plasticizers and binders are required to disperse and suspend the ceramic powders in the slurry. As the formation of an ideal sample requires that the chemical purity of the powders be maintained, slurry formation with additives is a disadvantage.

Comparing dry and wet ceramic forming techniques, it was determined that dry forming with a double-ended press was the best candidate for green body formation primarily for maintaining the chemical purity of the powder. A stainless-steel die with a 0.635 cm diameter was selected. Corresponding stainless-steel plungers were selected with 0.635 cm diameters and end caps to assist in plunger withdrawal. Smaller diameter stainless-steel dies were tested; however, the gauge on the hydraulic press was not sensitive enough to measure the load accurately for these sizes. The desired pellet formed using dry pressing was 0.635 cm in diameter and 2 mm thick. Using dry pressing literature [72]–[74] as a reference for starting conditions, trial and error was used to establish the optimal values for the following variables involved in pellet formation:

- Hydraulic load and plunger pressure
- Time held at max load
- Powder mass for each pellet to achieve a thickness of 2 mm

The optimal pressure applied to NiO-MgO powders was established to be 40 MPa. Lower pressures resulted in fragile pellets that broke apart during the pellet extraction. Pellets that did survive commonly deformed or broke up during sintering and had observable density gradients in the final sintered pellet. At pressures above 40 MPa, capping defects were observed in the

pellets. Sintered pellets would deform during the sintering process and sometimes shatter. At higher pressures extracting the die plungers became difficult as the plungers began to plastically deform under the pressure. Pressure of 40 MPa minimized the observed problems and failures during sintering and therefore was selected.

Hold times at 40 MPa were investigated measuring the impact on the green body density. Hold times longer than 1 minute were measured to have no discernable increase in green body density. With pressure and hold times set, the mass of powder used for each NiO-MgO composition to achieve a 2 mm thick pellet was then determined. Multiple 2 mm thick sample pellets were then made for all five of the NiO-MgO compounds. Green body densities were estimated using calipers, as green bodies formed became unstable in liquid, preventing measurement with the Archimedes method. Green body densities ranged from 55-68% compared to the calculated theoretical density.

3.3 Sintering and Densification

3.3.1 Conventional Sintering

Conventional sintering is the application of heat to a green body compact in order to change the packed aggregate into a solid compact. During the sintering process grain growth and densification occur, as discussed in greater detail in Chapter 1. Powders produced using the amorphous citrate process and formed by dry pressing were enclosed in a MgO crucible on top of a second pellet of the same composition and covered with powder of the same composition. The bottom pellet and excess powder were to protect the pellet from the atmosphere and the crucible, preventing evaporation and diffusion to maintain the chemical stability of the pellet. The crucible was placed inside of a box furnace's hot zone and sintered.

The theoretical densities for each of the five base NiO-MgO compositions were calculated, shown in Table 3-1. The lattice parameter was extracted from XRD measurements and used to calculate the theoretical density using NiO-MgO's known crystallography. References to density measurements from this point on will refer to the relative density comparing samples measured density to that of its theoretical density with the objective of achieving 100% relative density.

Table 3-1: NiO-MgO Calculated Theoretical Density

Composition NiO:MgO	Lattice Parameter (nm)	Theoretical Density (g/cm ³)
100:0	0.4236	6.5273
75:25	0.4196	5.9427
50:50	0.4211	5.1147
25:75	0.4225	4.3068
0: 100	0.4182	3.6603

3.3.1.1 Conventional Sintering Optimization

Sintering temperatures of 1400°C, 1500°C and 1600°C were investigated with 10 hours hold times. Very little densification occurred at 1400°C, with the highest density measured never exceeding a 70% relative density. Samples sintered at 1500°C and 1600°C achieved similar relative densities, averaging 78%. To minimize the grain growth during sintering, 1500°C was selected as the optimal temperature, as grain growth is slower at lower temperatures. The sintering temperature of 1500°C was selected also based on the work done previously by Handwerker et al. [54]. Handwerker et al. measured the equilibrium crystal shape of NiO-MgO alloys after long annealing times at 1500°C. Therefore, 1500°C was selected as the sintering temperature so the equilibrium crystal shapes measured would be concurrent with the grain growth studies and maximize the sample's densification.

Furnace hold times of 4, 8, 12 and 48 hours at 1500°C were investigated to determine the optimal sintering duration. The relative density was measured using the Archimedes method and open porosity was estimated using the Archimedes method as the success metric. Samples' relative density increased up to 12 hours and made no significant gains after. As relative density increased, open porosity decreased and leveled off after 12 hours. The inverse relationship for 75:25 Ni:Mg powder is shown in Figure 3-1. It is well established in sintering literature that higher heating rates increase the densification of a sample during sintering. Heating rates of 5°C/minute and 20°C/minute were testing. As expected, a samples relative density was higher when the higher heating rate was used and a heating rate of 20°C/minute was selected.

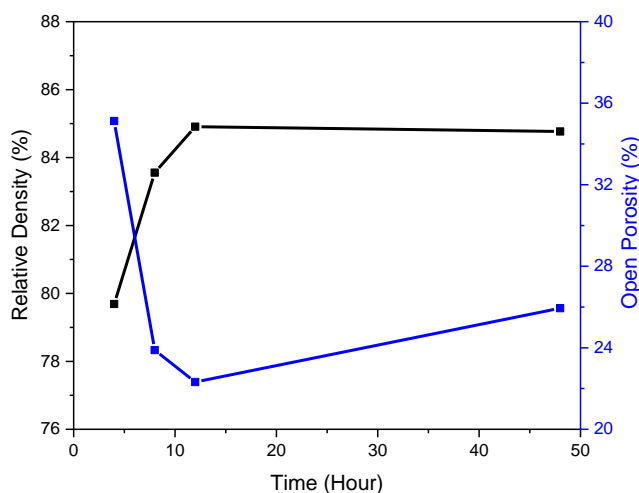


Figure 3-1:Relative density and open porosity as a function of time for 75:25 Ni:Mg powder. Relative density increases over time where open porosity, inversely, decreases.

The final sintering procedure was to heat samples at a rate of 20°C/minute to 1500°C and hold for 12 hours finishing with air cooling to room temperature. Samples of all five powders were sintered in this manner. Representative microstructures for 75:25, 50:50, and 25:75 Ni:Mg are shown in Figure 3-2. Final densities for all samples ranged between 88-92% relative density. As can be seen in the SEM micrographs, the microstructures do not meet the desired standards. Significant porosity is visible across all samples with inter and intra granular pores present. The grain size is also larger than desired, averaging roughly 15 μm . Even using optimized sintering conditions, pellets conventionally sintered did not meet the required conditions to allow successful grain growth studies.

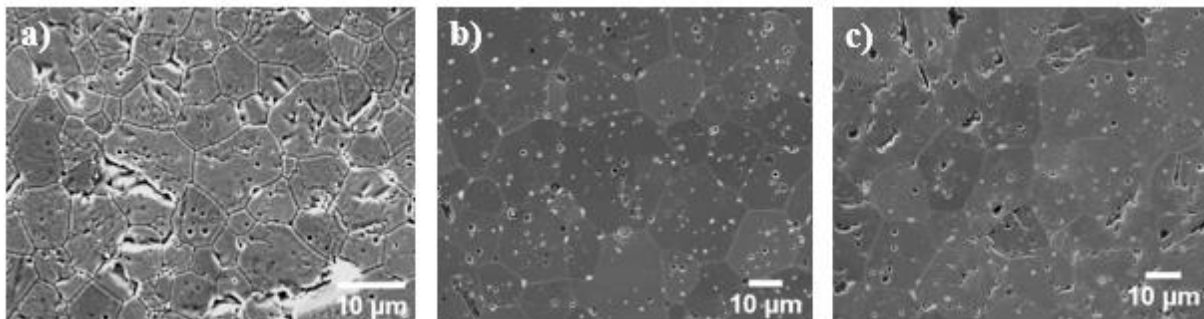


Figure 3-2: SEM micrographs for a) 75:25, b) 50:50 and c) 25:75 Ni:Mg powders. All micrographs show extensive inter- and intra-granular porosity.

3.3.1.2 Investigation of Particle Size and Morphology

In Chapter 2, it was discussed that powders produced by the amorphous citrate method had a platelet geometry. Platelets are known to pack poorly compared to spherical particles, lowering the final density of the green body [61]. As conventional sintering was only achieving final relative densities ranging from 88-92%, the inhibiting effect of the particle geometry was investigated. Powder samples were ball milled for 24 hours to break up the agglomerates. The impurity contamination from ball milling was ignored. Milled powders were dry pressed and conventionally sintered using optimal parameters. The samples final relative densities were measured to be 95-96% and impurity particles confirmed to be yttria stabilized zirconia were found in the microstructures. Therefore, the particle geometry was inhibiting the densification of the NiO-MgO powders. However, even minimizing the effect of particle geometry, NiO-MgO displayed poor sintering behavior. It was therefore determined that conventional sintering of NiO-MgO samples could not be fully densified to create ideal samples for grain growth measurements.

3.3.2 Spark Plasma Sintering

With conventional sintering failing to achieve fully dense samples, spark plasma sintering, a form of field assisted sintering, was attempted. Spark plasma sintering subjects the powder to heat and pressure during the sintering process. A spark plasma sintering apparatus schematic is shown in Figure 3-3. The ceramic powder is placed in a graphite die in a vacuum furnace and the apparatus is pumped down. A load is applied to the die using a hydraulic system

via die plungers. Unlike conventional sintering where heat is applied to the powder only by an external source, furnace heating elements, spark plasma sintering also uses an internal source. A DC electric current is applied to the die and powder inducing resistive heating, Figure 3-4. The temperature, heating rate and hold times are all controlled via the DC power source.

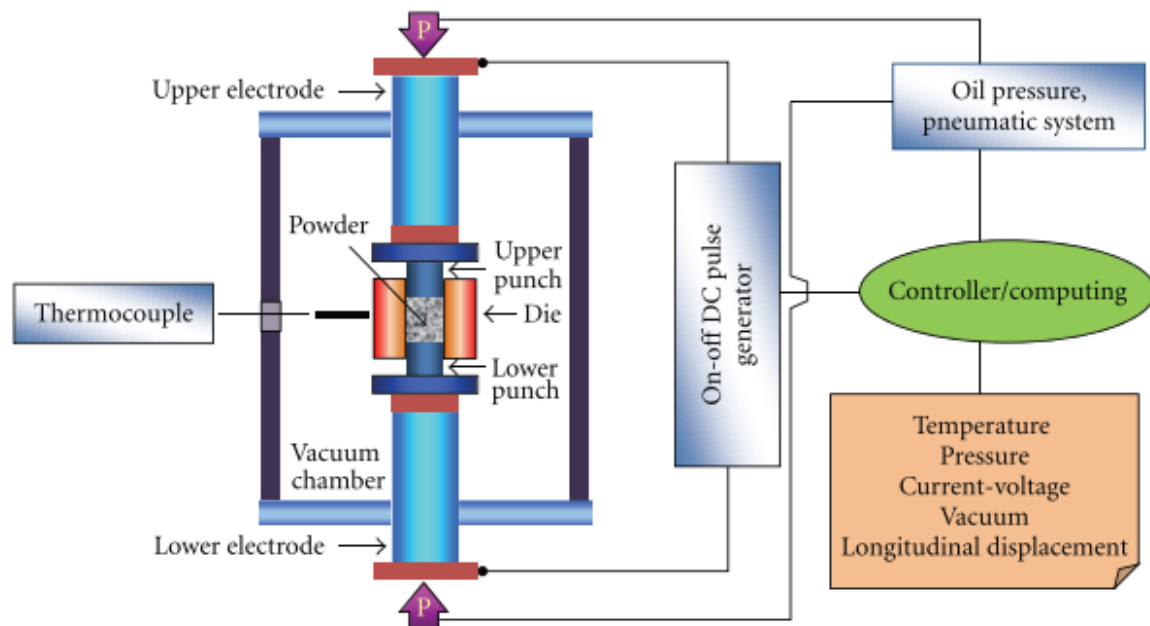


Figure 3-3: Diagram of spark plasma sintering apparatus. Powder is inserted into a double-ended die in a vacuum chamber and pressed with hydraulic rams. Resistive heating occurs by the application of an DC current through the die and powder [75].

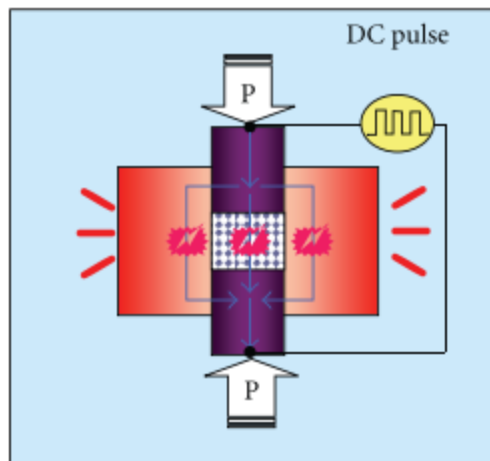


Figure 3-4: Diagram of spark plasma sintering double-ended die. Powder is compressed in the die between two plungers while a DC electric current is applied shown in the diagram as light blue arrows. Resistive heating heats the powder and die[75].

Spark plasma sintering trials were conducted in collaboration with Wolfgang Rheinheimer at Karlsruhe Institute of Technology. Several samples of 50:50 Ni:Mg powder were spark plasma sintered at 1250°C for 10 minutes with a pressure of 50 MPa. The sintered samples' color changed from solid green to green and black. The interior of the sample was green, and the outside shell was black. The density of the sintered samples was greater than 95% of the theoretical measured using the Archimedes method. Sintered samples were cross sectioned, polished, thermally etched at 1150°C and analyzed using SEM imaging.

The color transition of regions of the spark plasma sintered samples was determined to be due to the reduction in oxygen levels similar to what was discussed in Chapter 2. As the spark plasma sintering process was done in vacuum, the oxygen was removed from the surface first, creating an oxygen depleted zone. The center of the samples remained green due to the short exposure to the vacuum and would have been removed if held in vacuum longer. Both the oxygen-rich and oxygen-depleted segments of microstructure showed significant reductions of porosity compared to conventionally sintered samples. In both sections, contamination along grain boundaries was observed with particles appearing to pin boundaries. While the source of this contamination was not identified it was believed to be likely related to the polishing process. While the average grain size was similar in both regions of the spark plasma sintered samples, their microstructures had different behaviors. During the thermal etching process at 1150°C, the

grain boundaries of both microstructures were etched, Figure 3-5. In the oxygen-depleted region, the grains showed significant growth and surface faceting compared to the oxygen-rich regions. The reason for this behavior was not discovered.

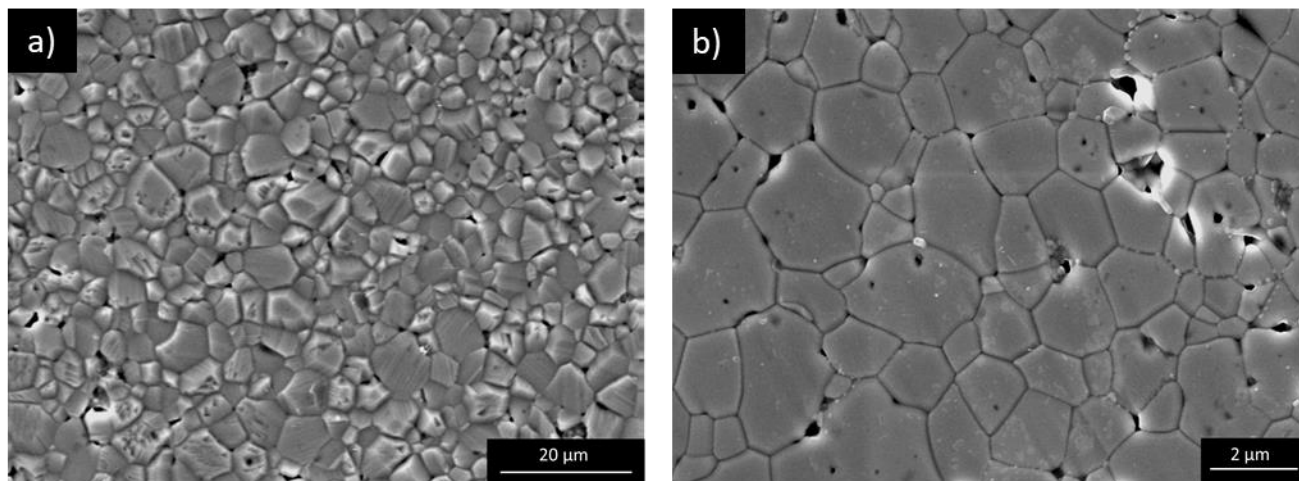


Figure 3-5: SEM micrographs of a) oxygen-depleted and b) oxygen-rich regions of a 50:50 Ni:Mg spark plasma sintered sample. Oxygen depleted and oxygen rich regions showing distinct microstructures after thermal etching at 1150°C. Oxygen depleted regions showing significant surface roughening by comparison.

The formation of oxygen depletion zones during spark plasma sintering raised concerns that the samples produced may no longer be compositionally, homogenous. Along with the unexplained behavior during the thermal etching process and remaining porosity, spark plasma sintering was abandoned as a viable sintering technique for NiO-MgO.

3.4 Hot Pressing

Concurrently with the investigation of spark plasma sintering, the sintering technique of hot pressing was investigated. Hot pressing uses the application of heat and pressure during the sintering process, Figure 3-6. The pressure is applied through hydraulic uniaxial plungers. The heat is externally generated, as in conventional sintering by furnace heating elements. The hot-pressing units available at Purdue that were able to reach the desired 1200°C used dies and plungers made from graphite. As graphite is flammable in oxygen around 500°C, the hot-press

furnaces operate under vacuum. The graphite dies are also brittle, limiting the pressure that can be applied to the powder before the die breaks to 50 MPa. The powders being sintered were enclosed in graphite foil to prevent contamination of the dies. The die setup is shown in figure 3-7.

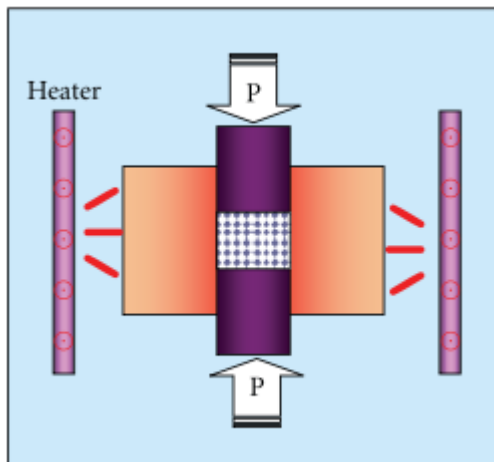


Figure 3-6: Diagram of a general hot press double-ended die. Uniaxial pressure is applied through plungers while the die is heated by the surrounding furnace under vacuum[75].

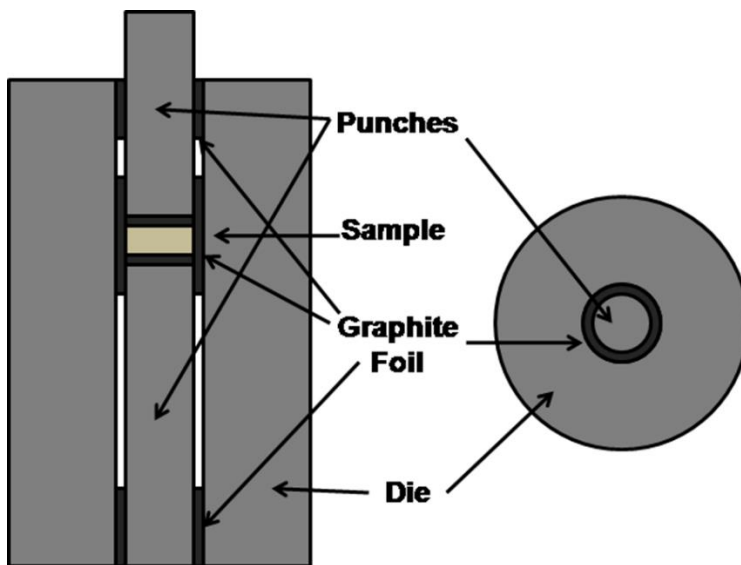


Figure 3-7: Diagram of graphite double-ended die used. Powder is packed in graphite foil to prevent die contamination. Graphite foil is inserted at the top and bottom to align the plunger rods with the furnace hydraulic rods of the furnace reducing risk of fracture.

Samples of 50:50 Ni:Mg were prepared and sintered in the described hot press. Samples were heated at a rate of 10°C/minute to 1200°C and held for 2 hours at a pressure of 30 mmHg. The hydraulic plungers applied a pressure of 40 MPa during the hold at 1200°C. Samples sintered by hot pressing changed color from completely green to completely black, similar to the spark plasma sintered samples. The sample's density was measured using the Archimedes method and determined to be 100% dense compared to the calculated theoretical density. The samples were cross sectioned, polished, thermally etched at 1150°C and their microstructures were analyzed using SEM imaging.

Observed microstructures from hot pressed samples show fully dense samples, Figure 3-8. There are a few observable pores on the surface; however, they make up less than 1% of the microstructure, leaving large regions of the microstructure ideal for grain growth studies. Impurity particles were observed on the sample's microstructure. Investigation using EDS revealed that these particles were 100% Ni. XRD patterns were measured for hot pressed samples. The XRD analysis confirmed the presence of Ni metal. Therefore, during the hot pressing NiO was being reduced to Ni metal, which precipitated out at the grain boundaries. Further investigation found that the Ni precipitates were only found in regions near the surface of the samples. These observations of the NiO-MgO samples after hot pressing resemble that of NiO-MgO catalyst particles after reduction, Figure 3-9. While the microstructure of hot pressed samples appeared ideal for grain growth studies, the discovered reduction of NiO and Ni precipitate formation, showed that the compositional homogeneity of the samples were compromised. NiO-MgO samples could not be produced for grain growth studies using hot pressing due to the process occurring in a vacuum like spark plasma sintering.

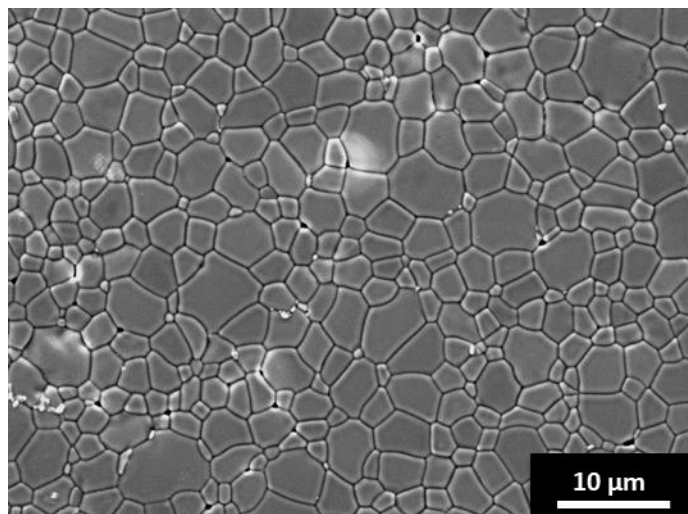


Figure 3-8: SEM micrograph of hot pressed 50:50 Ni:Mg powder. Microstructure exhibits minimal porosity appearing fully dense. Small impurities are observed at grain boundaries showing evidence of some pinning with changing boundary curvature.

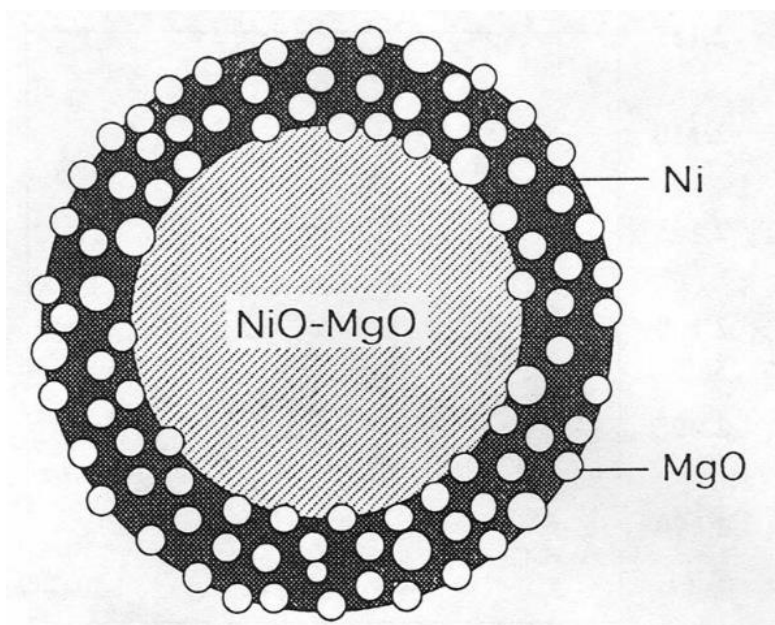


Figure 3-9: Schematic cross section of a NiO-MgO sample showing the reduction of the outer shell occurring first with the development of Pure Ni particles. The extent of the reduced section will expand with time in a reducing atmosphere[71].

3.5 Final Comments on Sintering and Densification of NiO-MgO Powders

Exhaustive efforts were made to form and sinter NiO-MgO powders. Conventional sintering achieved relative densities in the 88-96% range with poor final microstructures riddled

with pores. Spark plasma sintering improved to relative densities of 97-98%, still suffering from porosity. Hot pressing achieved acceptable fully dense sample with ideal microstructures; however, as with the spark plasma sintering, samples suffered from reduction reactions including the formation of Ni metal precipitates. Overall, no successful method to produce ideal fully dense NiO-MgO samples were found.

Literature sources report that sintering NiO and MgO to full theoretical density is challenging [1-4]. Achieving fully dense MgO samples is usually achieved using additives such as aluminum in small quantities. NiO is most often used as an additive to other processes and fully dense samples are not needed, therefore little work has been done. NiO-MgO's use as a catalyst was in part due to the ability to produce low density pores samples with ample surface area. NiO and MgO exhibit poor densification and sintering behavior and their NiO-MgO alloy does the same.

It is suggested that future attempts could be made to perform hot pressing under standard atmospheric conditions. This in theory will allow for the production of full dense NiO-MgO samples, assuming that the reduction process is not critical to achieving full density. This was not attempted as no equipment at Purdue was designed for this process. Locating an available hot press that function in atmospheric conditions will be challenging as the process essentially creates a large pressurized chamber of hot gas and comes with significant safety considerations.

4. GRAIN GROWTH

The following chapter was reprinted from David A. Lowing and John E. Blendell, “Grain growth and Microstructure Evolution in NiO-MgO Dependent on Anisotropic Crystal Shape” Submitted to Journal of American Ceramic Society (December 2018)

4.1 Introduction

It is well established in material science literature that material properties and performance are determined by their microstructure. Grain size plays an important role in the microstructure formation and determining the mechanical properties of a material. As grain size is reduced, mechanical properties like hardness, tensile strength and impact strength generally increase to a limit [12]. As grain size changes so does the grain boundary surface area present. Grain boundaries are well known to inhibit the motion of defects [11] and growth of cracks [11] as well as induce anisotropic electrical properties [12]. Accordingly, controlling grain growth during processing is critical to obtaining the desired microstructure and properties from a material. Multiple processing variables are known to influence the microstructural evolution and grain growth in a system. Altering the temperature, heating rate, pressure and atmosphere are well understood to influence grain growth rates and the final microstructure created[2]. As technology progresses, the need for new and novel properties expands, and new processing variables for the control of grain growth and microstructure are needed.

For grain growth to occur, grain boundaries must migrate within a material, causing some grains to grow and other to shrink. Ideal grain growth is commonly modeled with the velocity of grain boundaries as a product of a driving force and a boundary mobility term, equation 11.

$$V_b = F_b M_b \quad (11)$$

The driving force is based on the curvature of the boundary, equation 12. Atoms diffuse from areas of high curvature to low curvature, thereby moving the grain boundary. As grain size increases, the curvature of the boundary decreases, causing the curvature driving force to

decrease over time. Other driving forces may be applied such as a strain or a temperature gradient along with curvature.

$$F_b = \gamma_b \kappa \quad (12)$$

The mobility of a grain boundary is classically defined as the ability for atoms to migrate or “jump” across a boundary, equation 13. Atoms with enough energy provided by the driving force would jump across the boundary to a vacancy, resulting in grain boundary migration. Grain boundaries and interfaces in general are considered to be either atomically smooth interfaces, or faceted, or atomically rough interfaces. Faceted grain boundaries were found to maintain their atomically smooth interface during grain boundary migration. For faceted grain boundaries to migrate entire steps must nucleate and then grow or shrink to maintain their faceted interface structure. Random walk diffusion across the boundary would otherwise disrupt the faceted interface structure, incurring an energy penalty.

$$M_b = \frac{D_{eff}\Omega}{\delta k_b T} \quad (13)$$

Beyond simple models of grain boundary migration, drag forces exist and can inhibit grain boundary migration. Pores and particles attached to migrating grain boundaries will have to move with the boundary. However, when their mechanisms of migration are slower than the grain boundary, the result is a drag force on the boundary. This boundary drag force exists while the boundary migrates unless the boundary has enough energy to break away from the drag source. Materials containing solutes or impurities may have drag terms, called solute drag. Solute that segregates to a grain boundary minimizing its local lattice strain will remain at the grain boundary during migration. The solute will impart a drag force upon the moving boundary as the segregation profile must be maintained at equilibrium.

The above discussion assumes that grain boundaries are isotropic. Experimental evidence suggest that grain boundaries are anisotropic, as grain boundaries form faceted structures. Grain boundary energy can vary from grain to grain and along an individual grain boundary, forming facets. Regions of grain boundaries with different energies will behave differently under the

same conditions. The mobility and driving force will be different, resulting in grain boundaries in a system moving at a range of velocities even for single grain boundary. The extent that anisotropy effects grain growth is not well understood.

Studies have measured and compared grain boundary energy as a function of grain boundary plane orientation to the grain boundary plane distribution for Ni, [57] MgO [58] and others materials. The grain boundary energy and grain boundary plane distribution were found to have an inverse relationship with lower energy planes occurring more frequently in the grain boundary plane distribution [44]. The identified low energy planes were correlated to low index, low energy planes found on the equilibrium crystal shape for the material studied. The high frequency of grain boundaries planes corresponding to the low index planes indicate that grain boundaries favor configurations that contain low index planes over higher boundary symmetry options, despite having higher energies. Possible grain boundary configurations and overall distribution, therefore, become dependent on the stable planes that exist on the equilibrium crystal shape.

The equilibrium crystal shape is the shape a crystal will take to minimize its energy for fixed volume. Studies have shown that the equilibrium crystal shape can be altered by changing the temperature and chemical potential of a material [54]. As different grain boundary configurations have different properties, altering the grain boundary plane distribution will alter the materials' microstructural evolution. Therefore, changing the equilibrium crystal shape offers insight into possible mechanisms to modify the grain boundary plane distribution, thereby controlling grain growth.

This paper focuses on experimental work in the NiO-MgO system to measure the effect that changing the equilibrium crystal shape has on grain growth. The NiO-MgO system was selected due to the equilibrium crystal shape for pure NiO being octahedral, while pure MgO is cubic, with alloys forming composite equilibrium crystal shapes [54]. NiO:MgO is an isovalent solution that can be made by chemical routes with high purity negating drag forces. Grain growth studies were carried out across multiple compositions and temperatures, and the resulting grain growth behavior was evaluated.

4.2 Experimental

4.2.1 NiO:MgO Alloy Production

Modifications were made to the process developed by Marcilly et al. [64] to produce NiO-MgO alloy powders. Powder mixtures containing $\text{Ni}(\text{NO}_3)_2 \cdot 6\text{H}_2\text{O}$ and $\text{Mg}(\text{NO}_3)_2 \cdot 6\text{H}_2\text{O}$ with the desired ratio of Ni and Mg were created. Citric acid was used as the polyfunctional organic acid with an equal molar concentration of the combined Ni and Mg metallic cations. The powder mixture was melted and dehydrated in a vacuum rotary evaporator at 70°C with a pressure of 0.7 kPa. Dehydration occurred over the period of 30 minutes and the melt was transferred to a MgO crucible and allowed to cool, forming the foam structure. Based on work developing NiO-MgO as a catalyst [65]–[67] a two-step calcination process was developed. The foam was heated with a heating rate of $5^\circ\text{C}/\text{min}$ and held at 170°C for 1 hour. This step completed the dehydration of the foam and activated the polyfunctional acid, causing it to expand with the formation of gasses. The foam was then heated to and held at 500°C for 3 hours to complete the calcination process. Base powders of each of the five compositions were then heated to 1000°C , 1250°C and 1500°C with no hold at a heating and cooling rate of $5^\circ\text{C}/\text{min}$. Samples were held at 1500°C for 0, 1, 5, 10, 50 and 100 hours allowing for grain growth to occur.

4.2.2 Characterization

Base powders were characterized using X-ray diffraction (XRD) (Cu-K α radiation) determining homogeneity and crystallite size using Scherrer's equation [69]. Grain growth was measured on large multigrain, multilayer agglomerates using scanning electron microscopy (SEM). Average grain size was measured and calculated using the line count method across multiple agglomerates for each sample.

4.3 Results

4.3.1 Base Powder Characterization

XRD analysis of the five base powders measured five distinct homogeneous patterns, Figure 4-1a. Peaks' 2θ position correspond to the ratio of Ni and Mg present. As base powders' ratio of Ni and Mg is varied from 100% Ni to 100% Mg peak position shifts to higher 2θ values

moving from a NiO peak to a MgO peak. Peak position for 75:25, 50:50 and 25:75 NiO:MgO powders corresponded to the expected 75%, 50% and 25% Ni 2θ values for a linear extrapolation between the NiO and MgO peaks, Figure 4-1b.

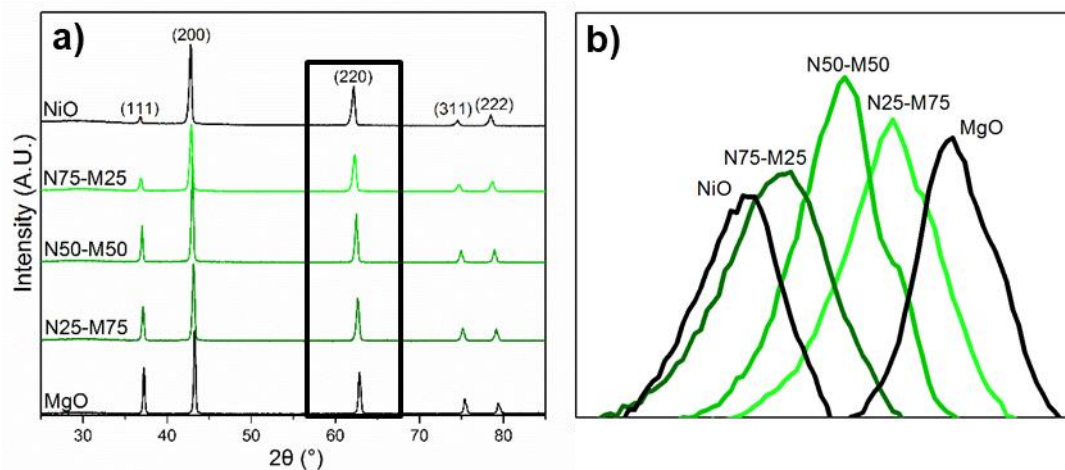


Figure 4-1: X-ray diffraction patterns (a) five compositions of NiO-MgO, (b) (220) peak highlighting formation of distinct peaks for each alloy ranging from pure NiO to pure MgO.

Powder crystallite size was calculated using Scherrer's equation, equation 14. λ is the wavelength of the Cu radiation, β is the full width half max, θ is the Bragg angle and K is the shape factor for which a value of 0.9 was used. Calculated values shown in Table 4-1 show an increasing crystallite size with increasing Ni content

$$\tau = \frac{K\lambda}{\beta \cos(\theta)} \quad (14)$$

Table 4-1: Calculated Scherrer Crystallite Size

Composition NiO-MgO	Crystallite Size (nm)
N0-M100	244
N25-M75	280
N50-M50	370
N75-M25	350
N100-M0	396

4.3.2 Grain Growth Agglomerate Selection

NiO:MgO powders produced following the amorphous citrate method resulted in the formation of hard agglomerates. Base powder crystallite size calculated from Scherrer equation ranged from 244-396 nm. Hard agglomerates in base powders ranged from 20-300 μm in size, Figure 4-2. The hard agglomerates were multigrain, fully dense made of multiple layers of grains initially, Figure 4-3. Grain growth studies reported in this paper were carried out on large agglomerates due to poor densification of green body compacts. Agglomerates selected for this study were selected to be larger than 50 μm in size. Agglomerates were required to be greater than 1 μm thick to ensure multiple grain layers were present at the start. Agglomerates needed a minimum of 50 interior grains.

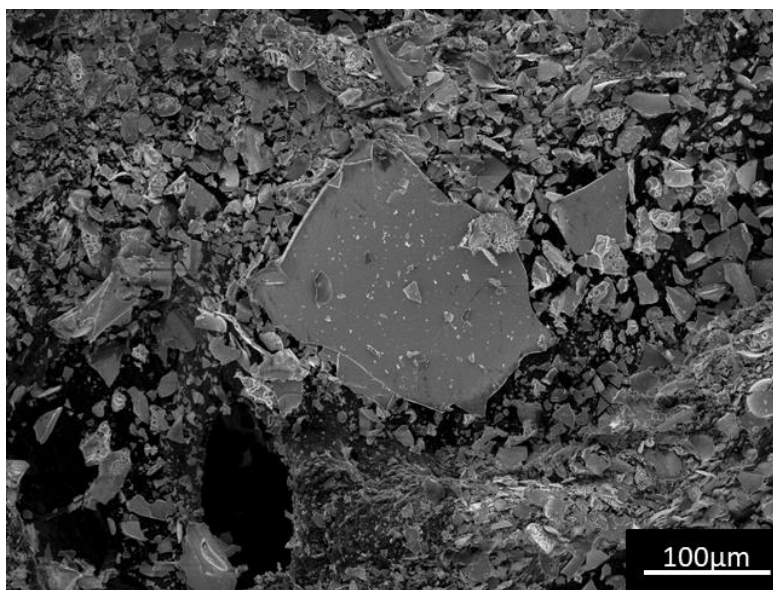


Figure 4-2: SEM micrograph of large agglomerates forming from amorphous citrate process with sizes greater than 100 μm.

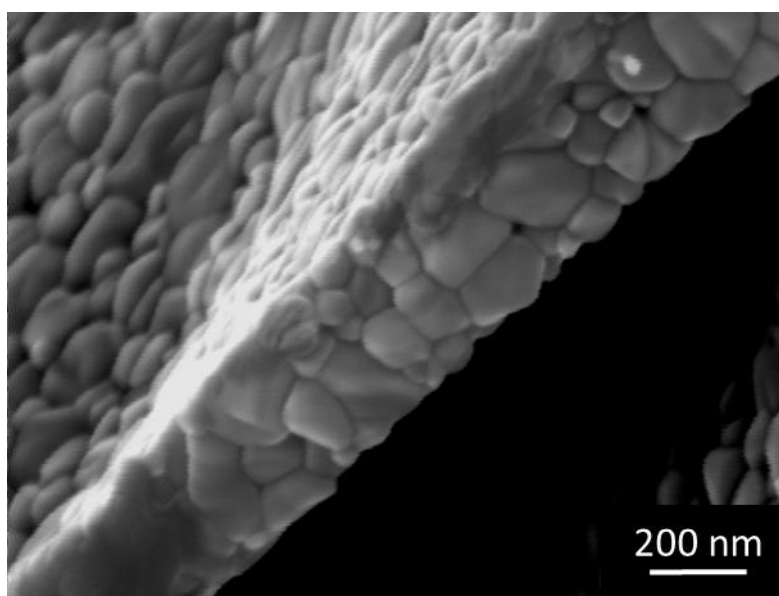


Figure 4-3: Sem micrograph of multigrain, multilayer agglomerate structures resulting from amorphous citrate process

4.3.3 Grain Growth

Average grain size was measured for five compositions at temperatures 1000°C, 1250°C, and 1500°C with no hold as shown in Figure 4-4. Average grain size measured at 1500°C for with multiple hold times, Figure 4-5. Initial crystallite size calculated from Scherrer's equation show larger crystallite sizes with increasing Ni content. Initial grain growth prior to 1500°C show significant grain growth occurring for all compositions. The grain growth prior to reaching 1500°C is seen to increase with increasing Ni content with a significant increase in samples with greater than 75% Ni. Samples held at 1500°C from 1-100 hours show continued growth with a diminishing growth rate as expected calculated assuming ideal grain growth, Equation 15.

$$G_f^2 - G_i^2 = kt \quad (15)$$

The rate of growth from 10-100 hours increased more rapidly with increasing Ni content, Table 4-2. At all times and temperatures, the average grain size for a sample increased with increasing Ni content of the sample, demonstrating the presence of a compositional effect.

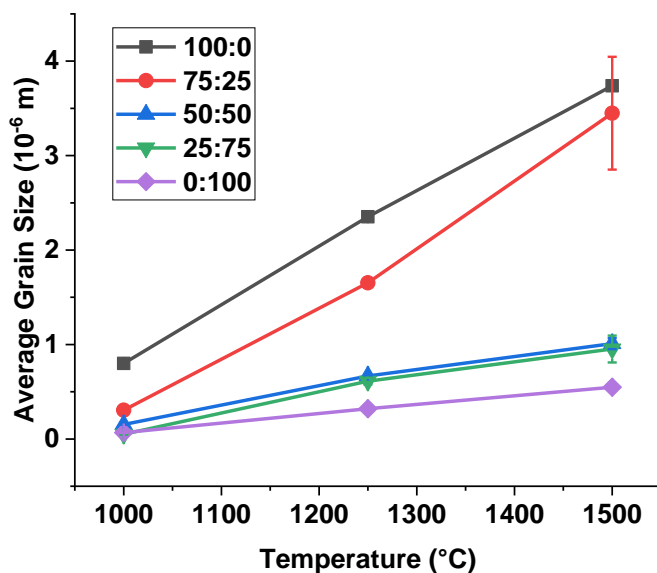


Figure 4-4: Temperature dependence of average grain size after zero hours annealing at temperatures from 1000°C to 1500°C.

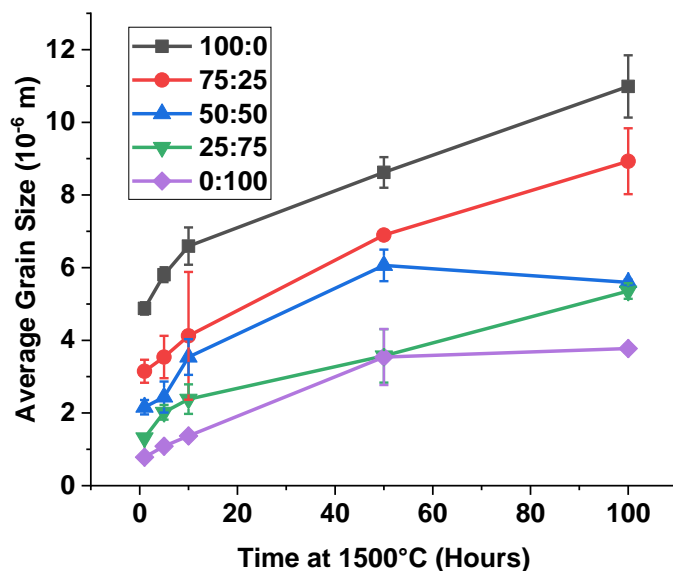


Figure 4-5: Dependence of average grain size on time held at 1500°C from 1-100 hours

Table 4-2: Grain Growth Rates for NiO-MgO Alloys

Composition	k ($\mu\text{m}^2/\text{s}$)
100:0	0.016324
75:25	0.011751
50:50	0.004485
25:75	0.00454
0:100	0.002294

Representative microstructures at different temperatures are shown in Figure 4-6. Samples that were held for 10-100 hours at 1500°C , which started out as multi-layered structures, had become monolayered agglomerates. The grains became large enough that the agglomerates were more representative of de-wetted thin films. The grain structure is columnar, having two solid-vapor interfaces. Therefore, the grain growth measured was the growth of surface grains. As temperatures increase and time passed surface grooving and surface faceting became more pronounced in the microstructures. A higher occurrence of sharp faceted grain surfaces was observed in samples that have higher Ni content. Low Ni content samples exhibited a higher occurrence of smoothly curved surfaces.

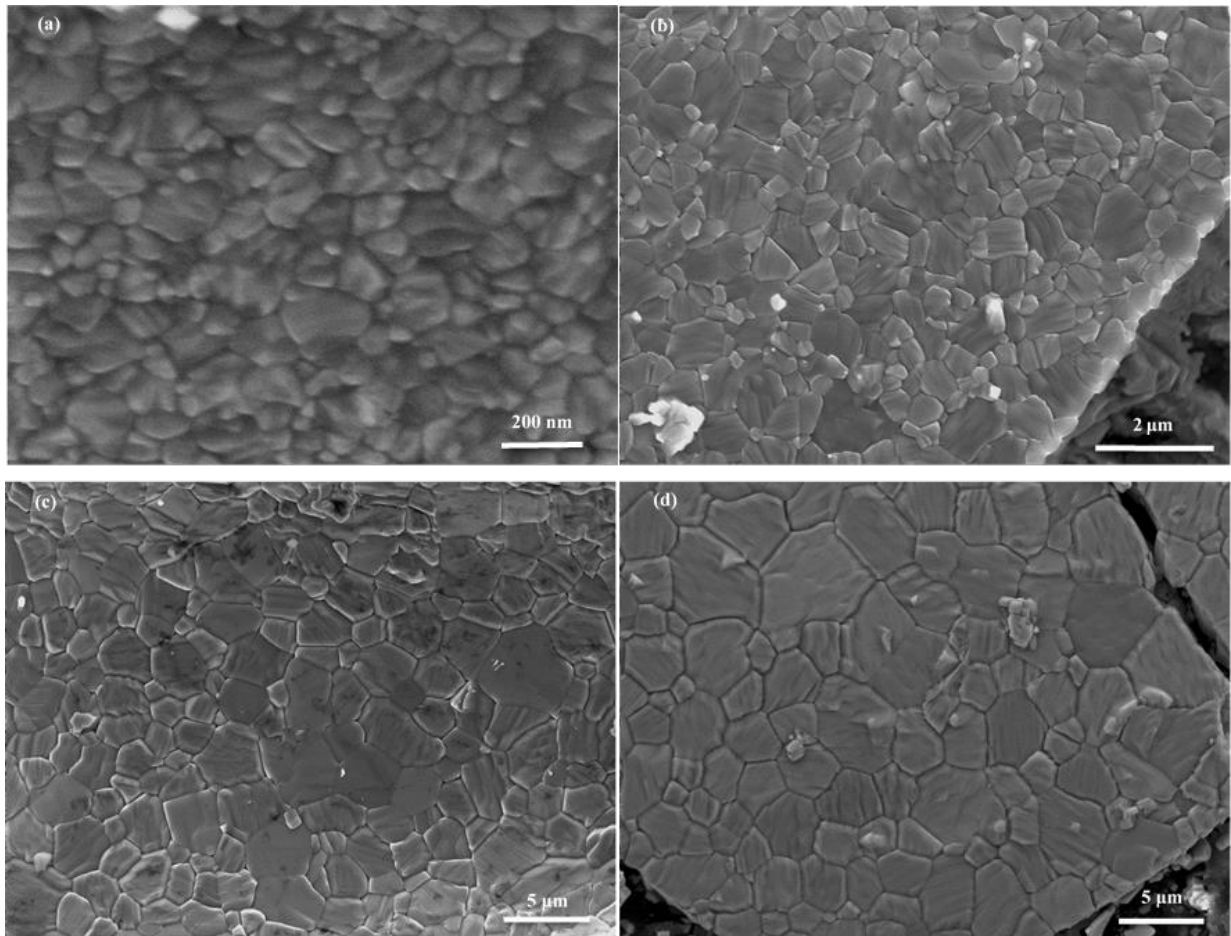


Figure 4-6: SEM micrographs of 75:25 NiO:MgO samples at (a) 750°C (b) 1000°C (c) 1250°C (d) 1500°C. Average grain size increased with increasing temperature

4.4 Discussion

The results show a change in the grain growth behavior as a function of composition in the NiO-MgO system. As the Ni content is increased, the average grain size and growth rate increased. Research by Handwerker et al. [54] indicated that, as the nickel content decreased, the equilibrium crystal shape had increasing amounts of smoothly curved surface area, resulting in lower Ni content alloys have more stable surface orientations available, that are seen as smoothly curved grain surfaces. Surface morphology results showed a transition from more smoothly curved grain surfaces to faceted with increasing Ni content. indicating a changing equilibrium crystal shape with composition. As all other variable effects are minimized, it is suggested that

changing the stable low energy planes and their surface area on the equilibrium crystal shape offers a method to control grain growth through the grain boundary plane distribution.

Pure NiO equilibrium crystal shape has {111} planes and pure MgO has {100} stable planes, with {110} planes possibly appearing in mixed alloys. Decreasing the Ni content decreases the surface area on the equilibrium crystal shape that corresponds to {111}, replacing it with other stable planes. The other stable planes, the {100} and {110}, change the grain boundary plan distribution. As the surface area for a given facet on the equilibrium shape increases more orientations incorporate the stable facet. When forming grain boundaries, the stable facet shows up at a higher frequency in the grain boundary plane distribution. A higher grain size when {111} grain boundaries are more prominent indicated that the {111} had a higher velocity grain boundary than that formed by the {100} and {110}. The change in velocity comes from a changing driving force or mobility of the boundary. The changing driving force results from how the grain boundary forms when including a {100} and {110} surface. Grain boundaries that form while maintaining a {111} surface may result in higher energy configurations compared to the others, therefore resulting in a higher driving force to minimize their surface area via grain growth. A change in mobility between {111} and {100} and {110} boundaries possibly results from changing activation energies for the nucleation of steps on the boundary.

It was observed that higher nickel concentrations resulted in a higher frequency of faceted grain surfaces. Therefore, the likelihood of a grain boundary being faceted increased as the surfaces forming the grain boundaries were faceted. So, the increasing average grain size and growth rate with higher nickel content is possible due to an increasing number of faceted grain boundaries. The faceted grain boundaries having a higher velocity matches the experimental observations made by Yoon et al[41].

4.4.1 Isolating the Effect of Changing Surface Anisotropy

Due to poor sintering properties, grain growth measured in this study was done on agglomerates and therefore is measuring surface grain growth. Surface grain growth introduces new variables not present in bulk grain growth studies. Surface grains have a solid-vapor interface. As grain growth occurs, a grain will be increasing the surface area of the solid-vapor interface while decreasing the grain boundary surface area. This introduces a bias in the system

selecting growing grains with a low surface energy and high grain boundary energy. As the equilibrium crystal shape of NiO:MgO changes as a function of composition, the low energy surface planes will change. Therefore, the strength of the bias will change with composition as the stable low energy planes change.

Surface grains as shown in the representative microstructures form thermal grooves during the heating process, unlike bulk grains. Thermal grooves form because of grain boundaries balancing their local energy. For grain growth to occur the grain boundary grooves move along with the boundaries by way of surface diffusion. The grooves may act as a drag force on the grain boundary and hinder grain growth. Grain boundary groove pinning will be present in all samples; however, as the composition changes the surface diffusion rate will change distorting the results.

As the drag from grain boundary grooves and bias from surface energies cannot be removed from this study, it is important to note that the effect on grain growth from changing the surface energy anisotropy cannot be completely isolated. It is noted that the strength of the effect from surface energies and grain boundary pinning is also influenced by changing composition in this system, as is the surface energy anisotropy.

4.5 Conclusion

The effect of a changing equilibrium crystal shape on grain growth was investigated. It was found that the average grain size and growth rate of the NiO-MgO system was altered when the equilibrium crystal shape was changed. It was suggested that changing the equilibrium crystal shape would alter the grain boundary plane distribution, changing the population density of specific grain boundaries. The grain boundaries formed from the {111}, {100} and {110} have different grain boundary mobility and driving forces, therefore different velocities. To confirm this hypothesis required the isolation of the effect of the changing equilibrium shape using the NiO-MgO system. System limitations resulting in surface grain growth measured on large agglomerates introduced possible error in the form of solid-vapor interfaces and thermal grooves, which effects could not be removed. Therefore, the research presented in this paper is a positive indicator that the equilibrium crystal shape could be used to alter grain growth but is not definitive. Further studies need to be done on polycrystalline samples that can be sintered to make fully dense samples.

5. LINKING SURFACE MICROSTRUCTURE AND EQUILIBRIUM CRYSTAL SHAPE WITH EBSD AND AFM

5.1 Equilibrium Crystal Shapes and N-Diagrams

As discussed previously in Chapter 1, the equilibrium crystal shape is the shape that an isolated and unconstrained volume of material will form to minimize its surface energy. The geometry of the equilibrium crystal shape can be determined from the polar plot of the surface energy as a function orientation through the Wulff construction [76]. The Wulff construction draws a line connecting the origin to the surface energy for each orientation and creates a tangent line to the surface energy. The tangent lines outline an inner shape around the origin, which is called the Wulff shape or equilibrium crystal shape. The surface energy as a function of orientation is known for very few materials; therefore, the equilibrium crystal shape is commonly measured from isolated pores and a minimum surface energy as a function of orientation plot can be calculated from the equilibrium crystal shape.

The original work presented in chapter 4 found alteration of the equilibrium crystal shape changed the grain growth behavior in the NiO-MgO alloy system. Therefore, the equilibrium crystal shape may be used as a mechanism to control the grain growth behavior of a system. Measurement of a materials equilibrium crystal shape, from pores is challenging and provides only qualitative information about the equilibrium crystal shape. To fully realize the ability to control grain growth via the equilibrium crystal shape a systematic and quantitative method for measuring the equilibrium crystal shape that could be applied to all materials was needed.

The n-diagram was proposed by Cahn et al.[54] as a method to display the missing orientations and faceting behavior of a system, analogous to phase diagrams. N-diagrams are thermodynamic slices similar to that of ternary phase diagrams where temperature and pressure are constant. The n-diagram takes the form of a stereographic projection with surface faceting information plotted. Rough regions on the equilibrium crystal shape, where all orientations are stable, appear as a single-phase region. Points on an n-diagram represent the normal to stable facet planes. Two facets meeting at an edge form a single tie line if there is a sharp edge between the two facets. If the edge between two facets contains a rough region, a fan of tie lines is shown similar to that of a phase diagram in the n-diagram representing the multiple possible faceting transitions between the multiple stable facets present. Corners are represented by tie-polygons.

N-diagrams can be read the same as phase diagrams however they provide information about the faceting behavior of the system. N-diagrams also allow for the construction of the equilibrium crystal shape from the information contained.

A simple example of an n-diagram is shown in Figure 5-1 for 4 equilibrium crystal shapes, all with sharp 2 facet transitions. In Figure 5-1 (a) the n-diagram for a simple cube has points representing the $\{100\}$ family of stable facets and tie lines connecting said facets. If we allow the formation of $\{111\}$ facets (b), we now see the inclusion of $\{111\}$ points on the n-diagram showing that the $\{111\}$ facets are stable and that they connect to 3 of the $\{100\}$ facets, with sharp edges as shown with tie lines. If the $\{111\}$ facets continue to grow until they touch each other (c), we see that there are 6 tie lines for each $\{111\}$ facet as it touches 3 $\{111\}$ and 3 $\{100\}$ facets. All the edges are sharp as we still only see single tie lines between the connected points. Finishing by allowing the $\{111\}$ facets, to dominate the equilibrium crystal shape we now see the removal of the $\{100\}$ facets as they no longer show up as points in the n-diagram, while the $\{111\}$ facets are still in contact with 3 other $\{111\}$ facets.

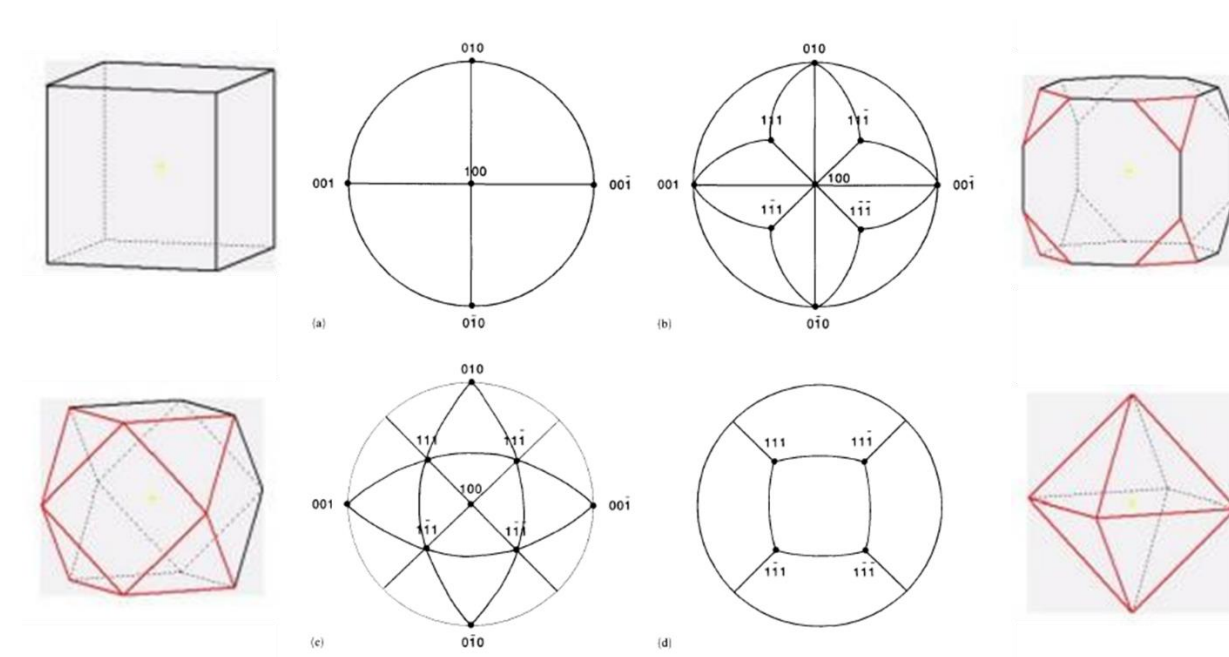


Figure 5-1: Four simple crystal shapes ranging from a cube to an octahedron with corresponding n-diagrams with sharp edges, showing how simple n-diagrams contain information which can be used to construct the equilibrium crystal shapes of materials. Recreated from [54].

While Figure 5-1 shows n-diagrams for simplistic equilibrium crystal shapes, real material examples are more complex. Shown in Figure 5-2 are two n-diagrams created from SEM images of NiO-MgO powder by Handwerker et al.[54], along with their 3D equilibrium crystal shapes. Part (a) shows a low Ni content sample with observed $\{100\}$ facets in the SEM image. The edges between the $\{100\}$ facets appear to be rough regions. Therefore, the n-diagram has points at the $\{100\}$ facets and the rest of the n-diagram is a single-phase regions representing all other orientations being stable. The $\{100\}$ facets are connected to the single-phase region by a fan of tie lines showing that edge between the two regions is curved and multiple transitions are possible. As the nickel content is increased, the equilibrium crystal shape and n-diagram is more complex, as shown in (b). From the SEM images, the presence of $\{100\}$ facets and $\{111\}$ facets are seen, and the corresponding points are on the n-diagram. There are also regions connecting the $\{100\}$ facets to each other and the $\{111\}$ facets to each other. From the SEM images, it was qualitatively estimated that these regions were rough regions, where all orientations were stable or a single-phase region on a n-diagram. In the n-diagram, we see the single-phase regions forming fan of tie lines between both the $\{100\}$ and $\{111\}$ points. The formation of 3-phase regions occurs at the corners where the rough region, the $\{100\}$ facet and the $\{111\}$ facet meet. While Figure 5-2 shows the formation of n-diagrams from SEM images, it highlights the qualitative nature of their construction. A more quantitative robust method for the creation of n-diagrams is needed if the equilibrium crystal shape is to be used to control grain growth.

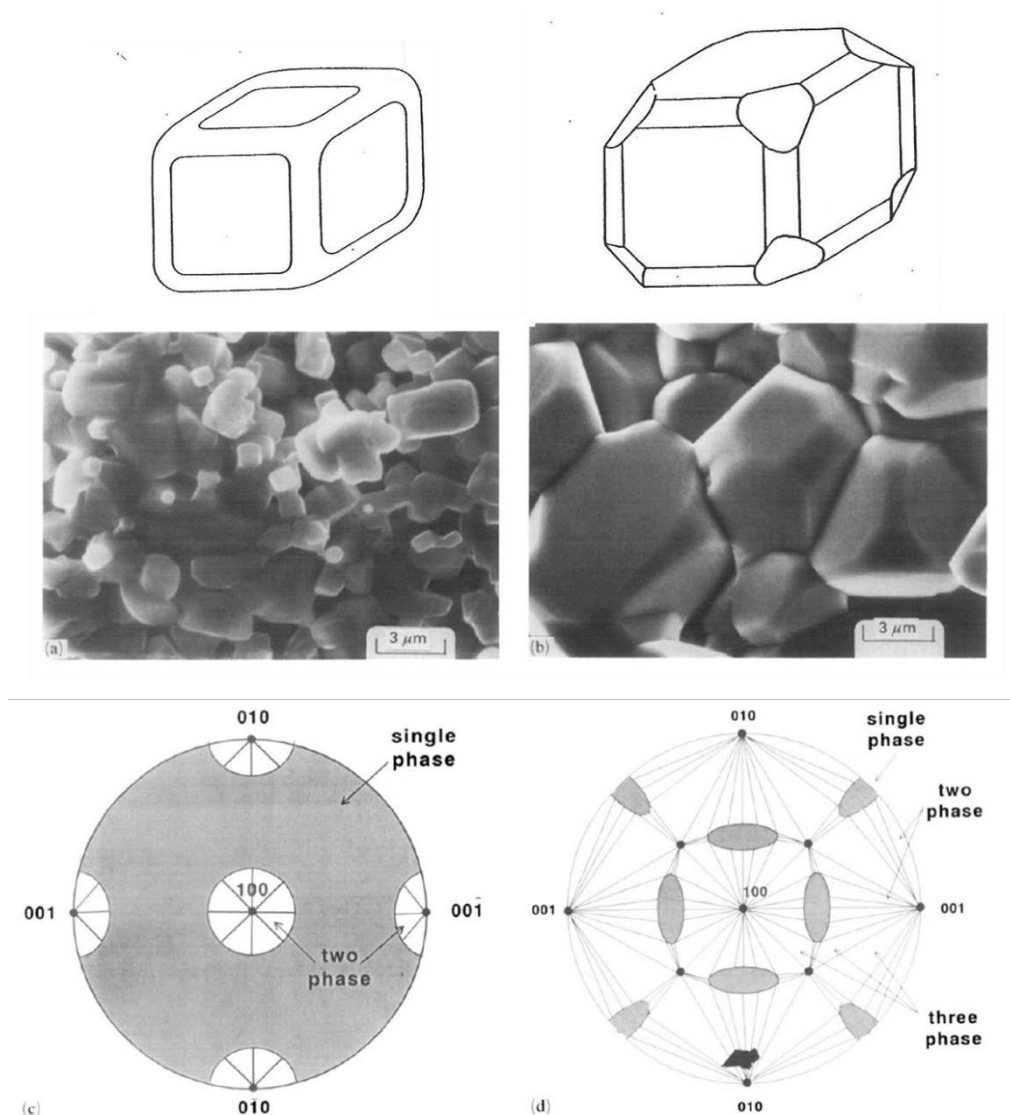


Figure 5-2: SEM images of low (a) and high (b) nickel content samples with corresponding equilibrium crystal shape determined from the image. N-diagrams for each equilibrium crystal shape is shown in (c) for low nickel concentrations and (d) for high concentrations[54].

5.2 Electron Back Scatter Diffraction and Atomic Force Microscopy Analysis

To produce n-diagrams for a material, the surface faceting behavior of a material as a function of orientation must be measured. The surface faceting behavior of a material can be measured using AFM. AFM provides a topographical scan of a materials surface in the laboratory frame of reference. The surface can be characterized measuring what grains form

faceted surfaces and what ones stay smoothly curved. AFM, however, does not provide information about the crystal structure of the material, and determining what facets form is not possible. Crystallographic information can be measured using EBSD. The EBSD technique provides the crystal orientation of each grain on a surface, as well as the Euler angles needed to rotate between the crystal reference frame and the laboratory reference frame.

Atomic force microscopy data comes in the form of (x,y,z) data. Each point on the surface has x and y coordinates, giving the location, and the z value gives the height of the surface at the specified location. To measure the surface faceting behavior, the AFM data needs to be converted into the crystal frame, and the normal direction of each AFM data point needs to be calculated. To accomplish this, a MATLAB script was created, seen in appendix A. The script binned each AFM data point and its 8 nearest neighbors into a square grid. Then, using least squares plane fit method, fitted a plane to the 9-point grid. The normal direction of the calculated plane was calculated. This process was completed for each point of AFM data.

Each surface normal was then rotated by the application of the EBSD Euler angles for the appropriate grain via a standard Bunge rotation matrix. The result was that each point of AFM height data was now a surface normal in the crystal reference frame, describing the surface orientation at a set of x and y coordinates. The data was then processed for quality of fit, setting R^2 value boundary conditions, commonly set to be above 90% to eliminate the peaks and valleys of the facets. The data set then contained surface orientation information for a grain. Each grain had a measured orientation from EBSD, and the surface behavior, such as what facets form or don't form, became known.

The data was plotted onto a stereographic projection and the surface facets or lack thereof were identified; examples will be shown later, in section 5.3. Therefore, by combining AFM and EBSD of a measured grain, the crystal orientation of the grain, as well as the surface faceting behavior of that orientation, could be determined. More detail on this code can be found in the appendix. This information was then used to produce n -diagrams for a system. A large sample of orientations was measured, and their corresponding surface faceting behavior identified; n -diagrams were constructed to reflect the measured behavior. This process can be performed over a range of temperatures, pressure, and chemical potentials, creating a series of n -diagrams for a material. The series of n -diagrams can then be used to predict the surface behavior of the sample and guide the processing to achieve a specific microstructure.

5.3 Surface Faceting Behavior Characterization Preliminary Work

Preliminary tests were carried out applying the developed EBSD and AFM combination scripts to determine the accuracy of the process. NiO-MgO alloys form a rock salt crystal structure with stable facets of $\{111\}$, $\{100\}$ and $\{110\}$ determined from previous work [77]. For reference, the three stable facets are plotted on a standard stereographic projection showing their locations, Figure 5-3. The $\{111\}$, $\{100\}$ and $\{110\}$ have three-fold symmetry, four-fold symmetry and two-fold symmetry, respectively, shown in Figure 5-4. Samples of 75:25 Ni:Mg were cross sectioned and polished then thermally etched at 1500°C for 1 hour prior to EBSD and AFM measurements.

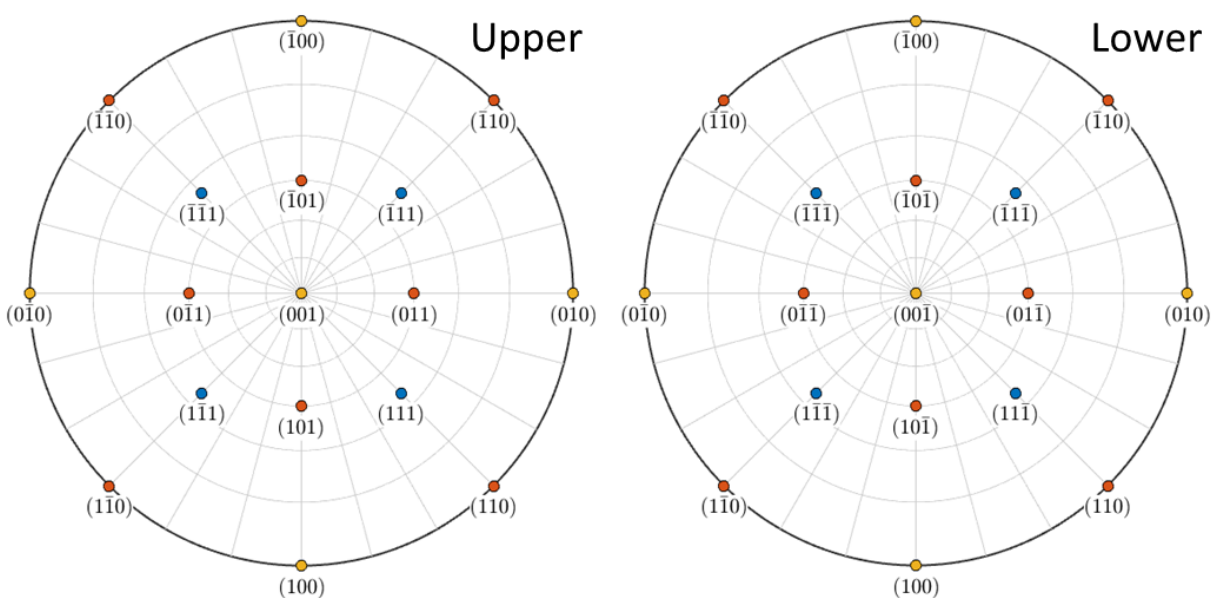


Figure 5-3: Stereographic projections for the upper and lower hemisphere for the rock salt crystal structure highlighting the position of the suspected stable facets in NiO-MgO the $\{111\}$, $\{100\}$ and $\{110\}$.

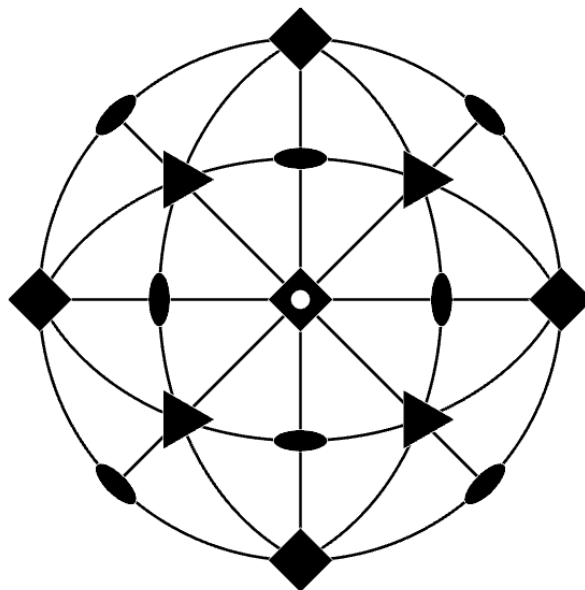


Figure 5-4: Stereographic projection for NiO-MgO showing the symmetry of the rock salt structure for $\{111\}$, $\{100\}$ and $\{110\}$ having three-fold symmetry, four-fold symmetry and two-fold symmetry respectively.

A random grain was selected, and the surface topography was measured in AFM. The grain was relocated in SEM and EBSD was performed. As the AFM and EBSD were not aligned, a rotation correction of 20° was measured for the sample aligning the reference frame axis for the AFM and EBSD. The data was then run through the MATLAB scripts. The orientation of the grain measured by EBSD was $[9, 2, 10]$ for the surface normal along the z-axis, the inverse pole figure for each laboratory axis is shown in Figure 5-5. The surface normals for the entire data set are plotted in a scatter plot and contour plot in Figure 5-6. The scatter plot shows a local cluster of points with a halo of scattered points around the center. The contour plot with overlaid stereographic projection and with high intensity being red and low blue, shows the cluster forming a single peak. This is the expected result, as the grain showed no significant signs of surface faceting having a stable surface orientation. The location of the peak in the contour plot approximates the orientation measured by the EBSD shown in Figure 5-5 for the z-axis laboratory frame. While the three stable facets were identified [77] as $\{111\}$, $\{100\}$ and $\{110\}$ for high nickel concentrations, the presence of the $\{110\}$ was in question, as the region may have been flat or smoothly curved on the equilibrium crystal shape. Therefore, the presence of a stable

surface with an orientation close to a $\{110\}$ support the presence of a smoothly curved region instead of a $\{110\}$ facet.

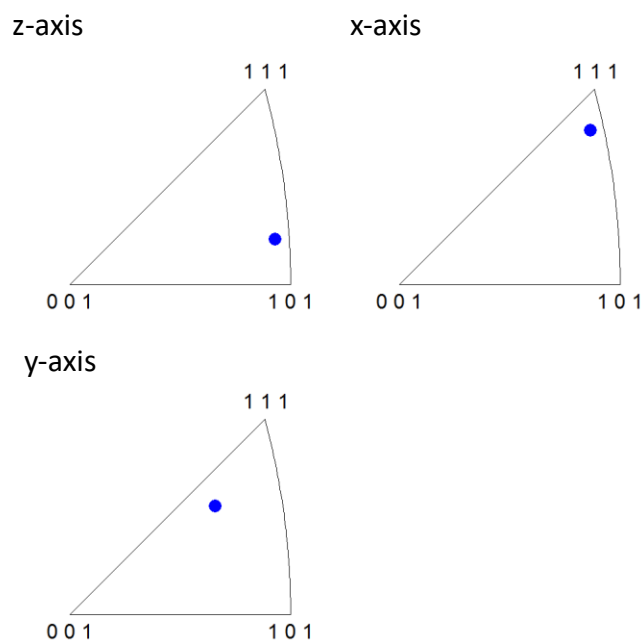


Figure 5-5: Inverse pole figures showing a randomly selected grain's orientation when view from the x, y, z laboratory axis frame of reference.

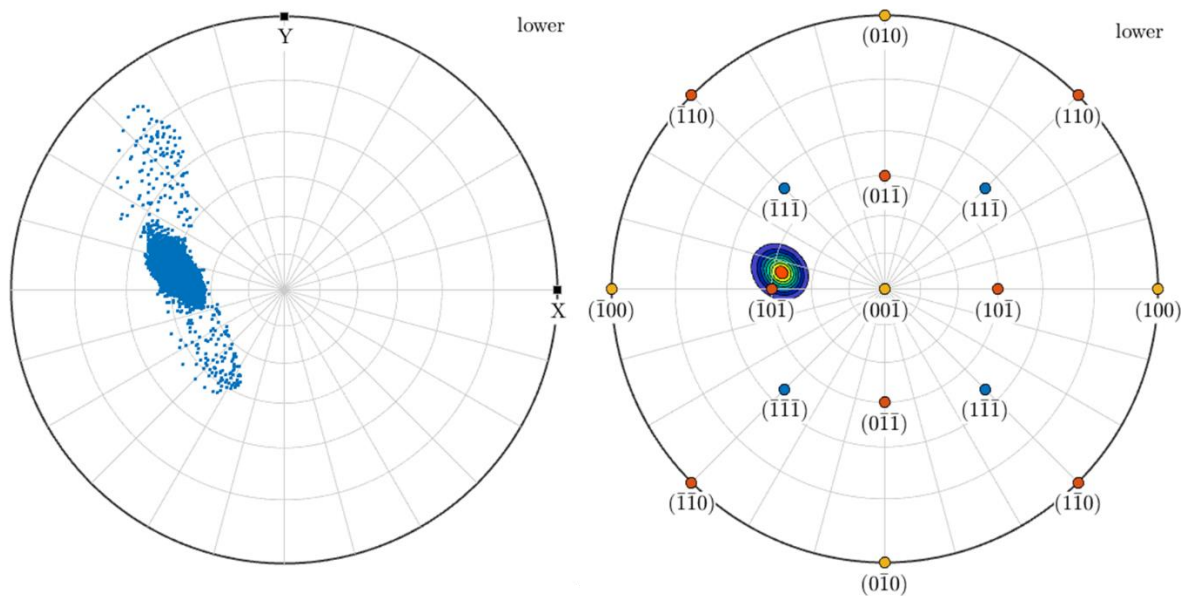


Figure 5-6: Scatter and contour plots showing the local crystallographic topography with an overlay of the stereographic projection. The plots show the formation of a single peak with an orientation closely corresponding to that of the grain measured with EBSD.

The characterization process was carried out for another randomly selected grain. EBSD measurements recorded an orientation of $[14, 8, 15]$ along the z axis of the reference frame shown in Figure 5-7. The scatter plot for all crystallographic surface data shows an elliptical cluster of orientations near the $[-1, 1, 1]$ confirmed to be a single peak by the contour plot, Figure 5-8. As for the previous grain, the peak location from the contour plot matches well with that for the orientation of the grain in Figure 5-7. The presence of a stable plane between the $[111]$ and $[101]$, as with the previously selected grain, indicate that the region believed to be the $[110]$ facet is likely a smoothly curved region with a range of stable orientations.

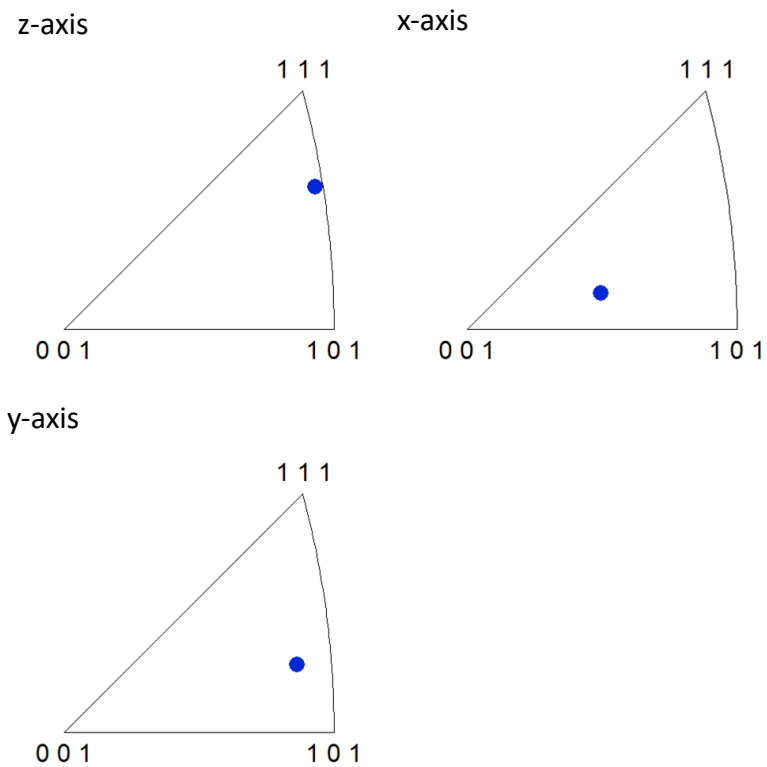


Figure 5-7: Inverse pole figures showing a randomly selected grain's orientation when view from the x, y, z laboratory axis frame of reference.

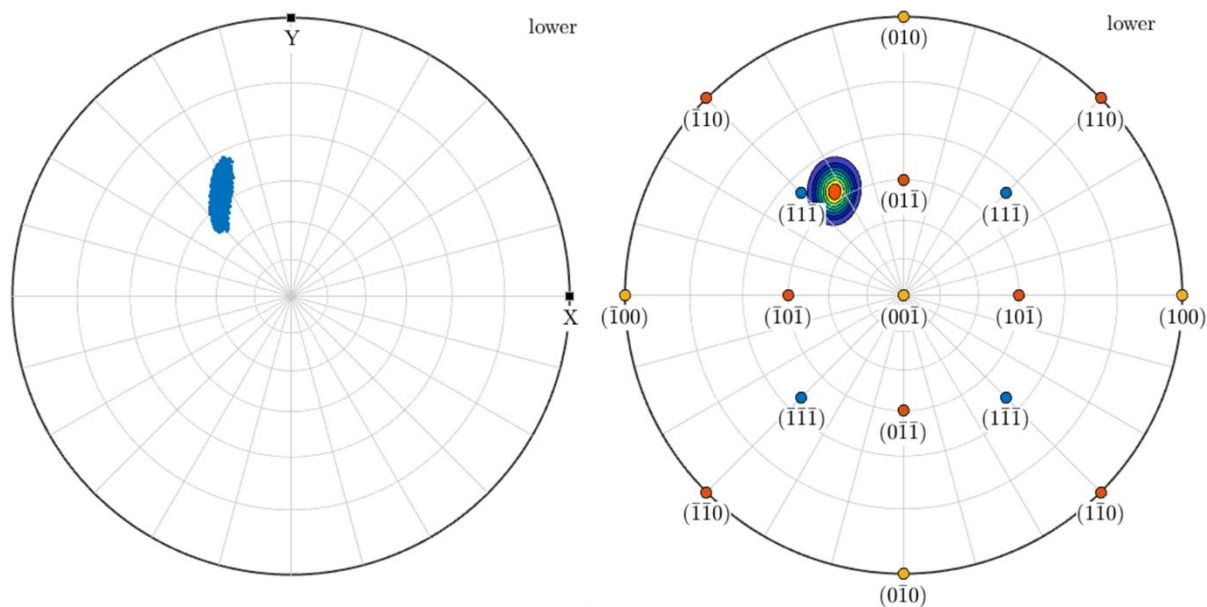


Figure 5-8: Scatter and contour plots showing the local crystallographic topography with an overlay of the stereographic projection. The plots show the formation of a single peak with an orientation closely corresponding to that of the grain measured with EBSD.

The number of grains the described methodology has been applied to is small due to time constraints and will be carried on by future students. The current number is too small to be applied to the production of a n -diagram yet. The discussed work does act as a proof of concept for this characterization technique. Characterization of the surface faceting behavior through AFM and EBSD provide information about what facets are stable and the transitions between the facets. The preliminary measurements indicate that the $[110]$ facet may not be stable and instead may be a smoothly curved region with multiple stable orientations. More data will need to be collected to determine if the transition between the $\{111\}$ and the $\{110\}$ is a continuous or discontinuous transition.

5.4 Final Comments and Future Work

At this stage, the process of combining AFM and EBSD data to characterize the surface behavior of a material as a function of its orientation using the created MATLAB script is possible. The script has been checked and achieves a reasonable preliminary accuracy in determining what facets, if any, are present on a grain surface. Sources of error in the calculations still exist and need to be corrected for manually. When scanning in AFM and EBSD,

a rotation correction is needed to align the axes of the two measuring techniques, which may differ due to sample loading. There are still issues in the plotting of the crystallographic topography, specifically with the application of symmetry artificially altering the intensity of the contour plots. It is likely that by applying initial symmetry, putting all raw data into one crystallographic triangle then applying full system symmetry, would correct the problem.

Further development of extracting information from the AFM data would be useful. Developing the ability to extract the facet angles in relation to the grain surface normal from the AFM data analysis program would allow for the automation of the facet identification without any manual data collection and analysis. The next step would be the collection of a large data set for materials. Just as phase diagrams had to be produced, so to do n-diagrams for materials. Materials surface microstructures need to be characterized with changing temperature, pressure and chemical potential. Once a full set of n-diagrams for a material has been made, it becomes possible to predict and control a materials grain growth and microstructural evolution using the equilibrium crystal shape.

APPENDIX A: EBSD-AFM SURFACE FACETING MICROSTRUCTURE ANALYSIS SCRIPT

EBS-DFM SURFACE FACETING MICROSTRUCTURE ANALYSIS SCRIPT

MOTIVATION

As discussed in chapters 1 and 5 the measurement of the equilibrium crystal shape of a material is commonly done by observations of isolated pores. This process is challenging and time consuming while only provides qualitative information about the equilibrium crystal structure. If the equilibrium crystal shape is to be used as a control mechanism for grain growth during processing accurate quantitative measurements of a materials equilibrium crystal shape is required. As discussed in chapter 5 a characterization technique combining AFM topography and EBSD crystallography was developed. The AFM and EBSD data were analyzed using a MATLAB script that was written. This section covers in detail the computational methodology used in the MATLAB script as well as a copy of the code for public use. The script was split into three sections of code each with their own objective.

LEAST SQUARES PLANE FIT AND ROTATION SCRIPT

The first segment of the script's objective is to extract the AFM data into a MATLAB matrix, plane fit the data and calculate the surface normal at each point and finally apply a rotation matrix the normal. The output is an array with a crystal normal for each xy data point and an array containing the R^2 value assessing the quality of fit for each xy coordinate.

First the script is designed to extract the AFM data from an ASCII file and convert the data into a xyz matrix. The ASCII file is generated by the program NanoScope created by Burker. The AFM raw data is opened in NanoScope and then reformatted into an ASCII text file. The ASCII text file is the input for the plane fit script. Initially the x and y data have the unit of steps while the z data or height data has a unit of microns. To standardize the units of the xyz data scaling information from the ASCII file header is extracted. The number of bins or steps used by the AFM and the physical length of the scan. This information provides a step to micron ratio. Using this ratio, the z data is converted to steps and now the xyz data are all in step units.

Each z or height data point and their nearest neighbors are grouped into 3x3 grids, with overlapping edges. Each 3x3 grid of 9 points had a plane fit to them. The plane fit was carried out using a least squares plane fit method built into MATLAB with a maximum iteration of 50. The normal to the best fit plan was calculated using simple cross products. The resulting plane normal and the R² valued were stored at the corresponding xy position. The result at this point is an array of surface plane normal identifying the local surface direction at a given xy coordinate in the laboratory reference frame and a corresponding R² value denoting the quality of the plane fit.

The laboratory reference frame is converted to the crystal frame through a rotation matrix. The output of the EBSD software is a series of Euler angles following the Bunge convention. Using the Euler angles corresponding to the correct grain of the AFM scan three rotation matrices were constructed following the Bunge convention of a z, x', z'' rotation. The rotation is applied to each surface normal converting the reference frame from the laboratory to the crystal. This concludes the least squares plane fit and rotation script. The final output is one array containing a surface normal for each xy coordinate from the AFM data and a corresponding array containing the R² value for the plane fit at each xy coordinate. The output has successfully characterized the AFM and EBSD data measuring the surface orientation. The following is the MATLAB code described:

```
function [Rval_array, crystal_normal_cell] = Plane_Fit_Main_Script_New(afm_text)
%This script is designed to crate a series 3x3 arrays from given data and
%run them through a plan fit script then output an array containing the
%best plane fit for each point in the form of a plane normal.

filename = afm_text; %sets text file name
delimiterIn = ','; %sets delimiter basis
data = importdata(filename,delimiterIn); %converts data from text to structure
data_array = data.data; %isolate data matrix from structure
header = data.textdata; %isolate header from structure

%confirm this will work dependig on text format
```

```

%extraction!!!!!!!!!!!!!!!!!!!!!!!!!!!!!!!!!!!!!!!!!!!!!!
[r,c] = size (data_array); % Measures row and column size
while c>1 %while loop removes all columes except c1
    data_array(:,2) = [];
    [r,c] = size (data_array); % Measures row and column size
end

%Header information extraction
line_count = char(header(130)); %isolate header line
Key = ""\Samps/line: '; %set search key
Index = strfind(line_count, Key); %find key in string
Value = sscanf(line_count(length(Key):end), '%g', 1); %set double to number following string

line_count = char(header(126)); %isolate header line
Key2 = ""\Scan size: '; %set search key
Index = strfind(line_count, Key2); %find key in string
Value2 = sscanf(line_count(length(Key2):end), '%g', 1); %set double to number following string

%Z reshaping and conversion
Mtx_1 = reshape(data_array, Value, []); % reshape matrix to correct dimensions
data_mtx = flip(Mtx_1); %flips matrix to match other formats
zcon = Value/Value2; % number of points divided by total length of x
data_mtx = data_mtx * zcon; %converting z height from nm to points

[data_array] = data_mtx;

%inputs
%-number of lines and points per line (assumed to be the same)
%-the z height data array
warning('off','curvefit:fit:iterationLimitReached') % Turns off Matlab warning
[r,c] = size (data_array); % Measures row and column size

```

```

crystal_normal_cell = cell(r,c); % Creates cell array matching input size
Rval_array = zeros(r,c); % Creates double array matching input size
x = 1:3; % Creates 1x3 vector
y = 1:3; % Creates 1x3 vector

u = 170; % EBSD angle 1
v = 122.1; % EBSD angle 2
w = 134.3; % EBSD angle 3
R1 = [cosd(u) sind(u) 0; -sind(u) cosd(u) 0; 0 0 1]; % Z rotation matrix
R2 = [1 0 0; 0 cosd(v) sind(v); 0 -sind(v) cosd(v)]; % X' rotation matrix
R3 = [cosd(w) sind(w) 0; -sind(w) cosd(w) 0; 0 0 1]; % Z'' rotation matrix
Rfull = R1*R2*R3; % Creates Euler angle rotation matrix

n=2;
m=2;
while n <= r-1
    while m <= c-1
        % Extracts data points and fits them to a plane cycles 50 times to get best fit
        point_array = [data_array(n-1,m-1) data_array(n-1,m) data_array(n-1,m+1);
            data_array(n,m-1) data_array(n,m) data_array(n,m+1); data_array(n+1,m-1) data_array(n+1,m)
            data_array(n+1,m+1)];
        [X, Y, Z] = prepareSurfaceData(x, y, point_array);
        [fitresult, gof] = createFit(X, Y, Z); %does the fitting for the plane ****
        % formula(fitresult);
        % Rval = gof.rsquare;
        Rval_array(n,m) = gof.rsquare;
        coe = coeffvalues(fitresult);
        % coeffnames(fitresult);
        if Rval_array(n,m) > 0.0
            % Creates 4 points on the calculated plane then 2 lines and solves the cross product

```

```

Z1 = (coe(1,1))+(coe(1,2)*1)+(coe(1,3)*1); % Calculates z-1
Z2 = (coe(1,1))+(coe(1,2)*3)+(coe(1,3)*3); % Calculates z-2
Z3 = (coe(1,1))+(coe(1,2)*3)+(coe(1,3)*1); % Calculates z-3
Z4 = (coe(1,1))+(coe(1,2)*1)+(coe(1,3)*3); % Calculates z-4
P1 = [1 1 Z1]; % Creates point using z-1
P2 = [3 3 Z2]; % Creates point using z-2
P3 = [3 1 Z3]; % Creates point using z-3
P4 = [1 3 Z4]; % Creates point using z-4
V1 = [P1(1)-P2(1), P1(2)-P2(2), P1(3)-P2(3)]; % Creates vector between point 1,2
V2 = [P3(1)-P4(1), P3(2)-P4(2), P3(3)-P4(3)]; % Creates vector between point 3,4
vec = cross(V1, V2); % Cross product of 2 vectors
% Normalizes the vector and applies the EBSD rotation using a rotation
% matrix
    normal = vec/norm(vec); % Normalizes vector
    normal = normal'; % Transposes vector
    crystal_normal = Rfull* normal; % Applies EBSD based rotation matrix
    crystal_normal = crystal_normal'; % Transposes vector
% Packages the vector as a cell and stores it in a cellarray
    normal_vector = {crystal_normal(1,1), crystal_normal(1,2), crystal_normal(1,3)};
    crystal_normal_cell(n, m) = {normal_vector};
else
% sets Rval and relative vector cell to zero making it a null result if it does
% not pass the quality control test
    Rval_array(n,m) = 0;
    normal_vector = {0, 0, 0};
    crystal_normal_cell(n, m) = {normal_vector};
end
    m = m+1; %column loop counter
end
m = 2; %Column loop counter reset at end of row
n = n+1 %Row loop counter

```

```
end
```

```
warning('on','curvefit:fit:iterationLimitReached') % Turns on Matlab warning
```

QUALITY CONTROL AND GRAPHICAL PLOTTING SCRIPT

The objective of this segment of code is to allow for quality control and plotting of the data produced by segment 1. The two arrays produced in segment one of the scripts and the desired R2 cutoff value are the input. The script searches each point and compares the list R2 values against the supplied cutoff value. If the fit quality lies above the cutoff limit the data point is transferred to a new array containing only passing data. The array of high-quality data is then reformatted into a text file readable by the MTEX MATLAB package for plotting.

The MTEX package for MATLAB is an extensive package for manipulating and plotting crystallographic data including EBSD data. The MTEX package was used to plot the surface normal vectors as a scatter plot and contour map on an equal angle projection. The projections were used as visual validation of the surface orientations calculated from the processed data.

```
function Data_Processing_Script(Rval_array, crystal_normal_cell)
```

```
[r,c] = size (Rval_array);
```

```
n=2;
```

```
m=2;
```

```
while n <= r-1
```

```
    while m <= c-1
```

```
        if Rval_array(n,m) > 0.9
```

```
            vector = [crystal_normal_cell{n,m}{1,1}, crystal_normal_cell{n,m}{1,2},
crystal_normal_cell{n,m}{1,3}];
```

```
            vector = vector * -1;
```

```
            fid = fopen('Vector_List.txt', 'a');
```

```
            fprintf(fid, '%f %f %f\r\n', vector);
```

```
            fclose(fid);
```

```
        end
```

```
        m = m+1;
```

```
end
m = 2;
n = n+1
end

figure;
fname = fullfile('Vector_List.txt');
v = loadVector3d(fname,'ColumnNames',{'x','y','z'});
contourf(v,'projection','eangle','grid')%change eangle to earea?
annotate([vector3d.X,vector3d.Y,vector3d.Z],'label',{'X','Y','Z'},'backgroundcolor','w')
%saveas(gcf,'1')

figure;
fname = fullfile('Vector_List.txt');
v = loadVector3d(fname,'ColumnNames',{'x','y','z'});
scatter(v,'MarkerSize', 2,'projection','eangle','grid')
annotate([vector3d.X,vector3d.Y,vector3d.Z],'label',{'X','Y','Z'},'backgroundcolor','w')
%saveas(gcf,'2')
delete Vector_List.txt
```

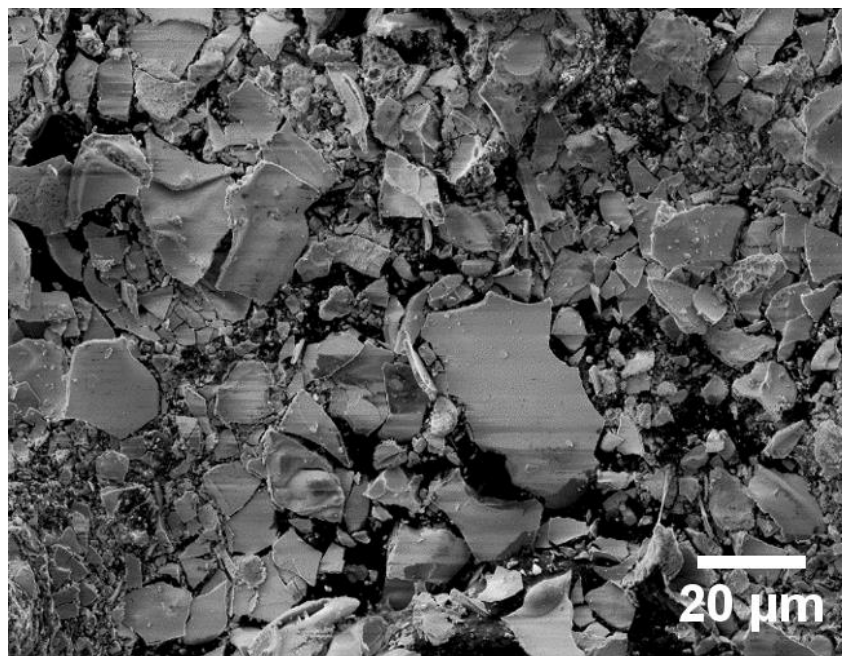
APPENDIX B: NiO-MgO PROCESSING DATA

Figure B. 1 SEM image of 50:50 NiO:MgO powder produced following the amorphous citrate method used for conventional sintering.

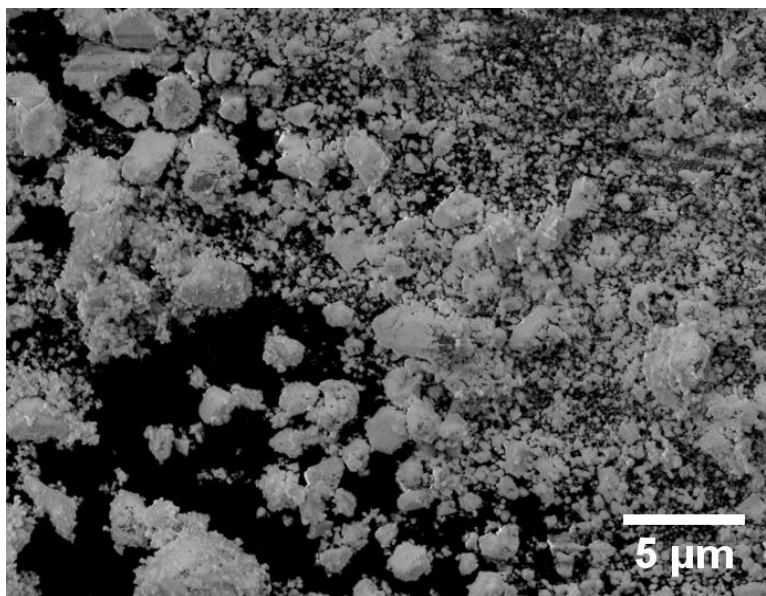


Figure B. 2 SEM image of 50:50 NiO:MgO powder produced following the amorphous citrate method and ball milled for 24 hours to reduce agglomerate size used for conventional sintering.

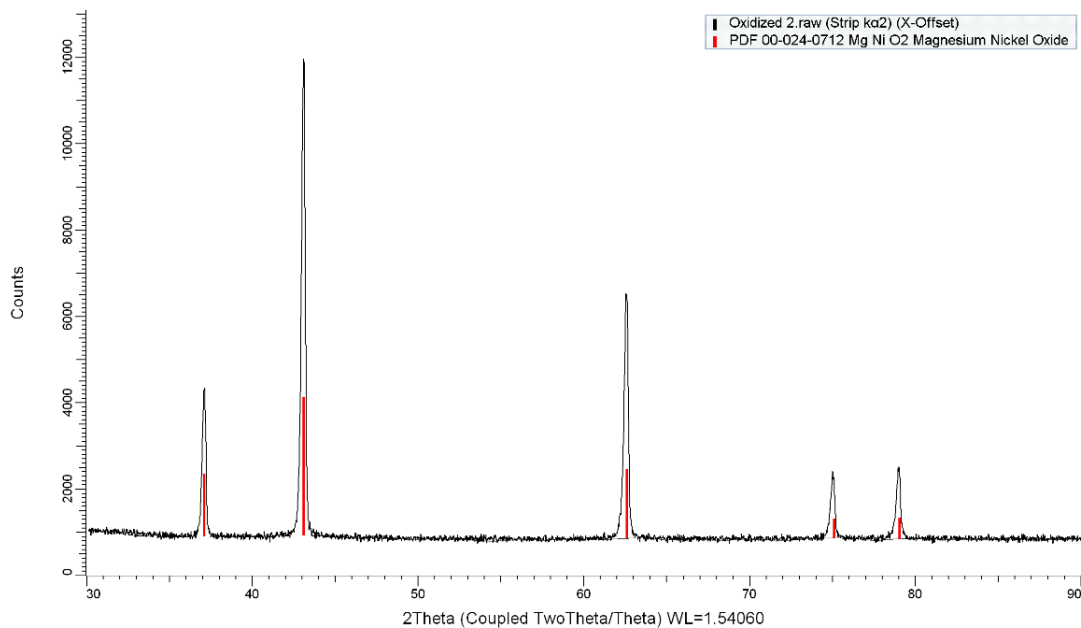


Figure B. 3 XRD pattern for green powder having the stoichiometric oxygen state and peak locations match the expected pattern for 50:50 NiO:MgO powder.

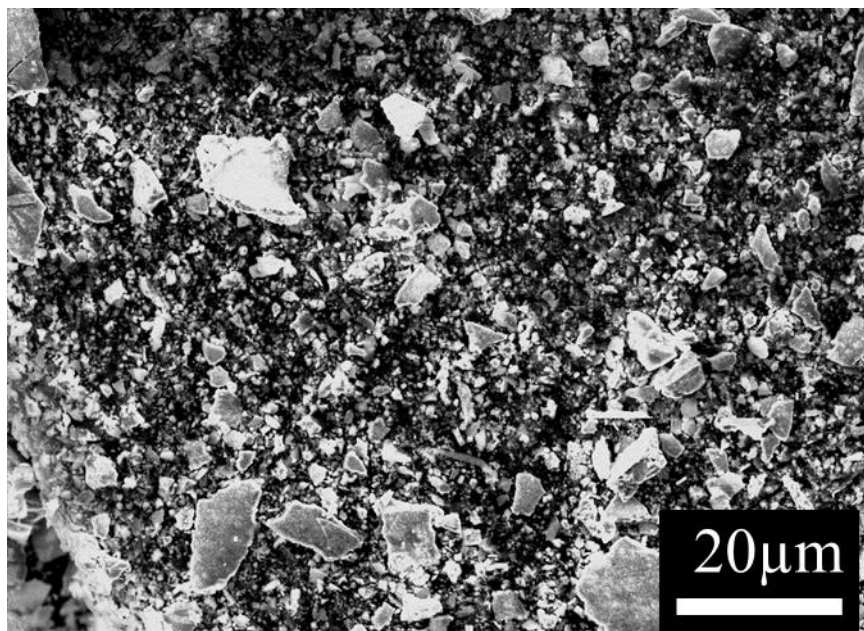


Figure B. 4 SEM image of 50:50 NiO:MgO powder having the correct stoichiometric oxygen ratio. Corresponding XRD measured in Figure B. 3.

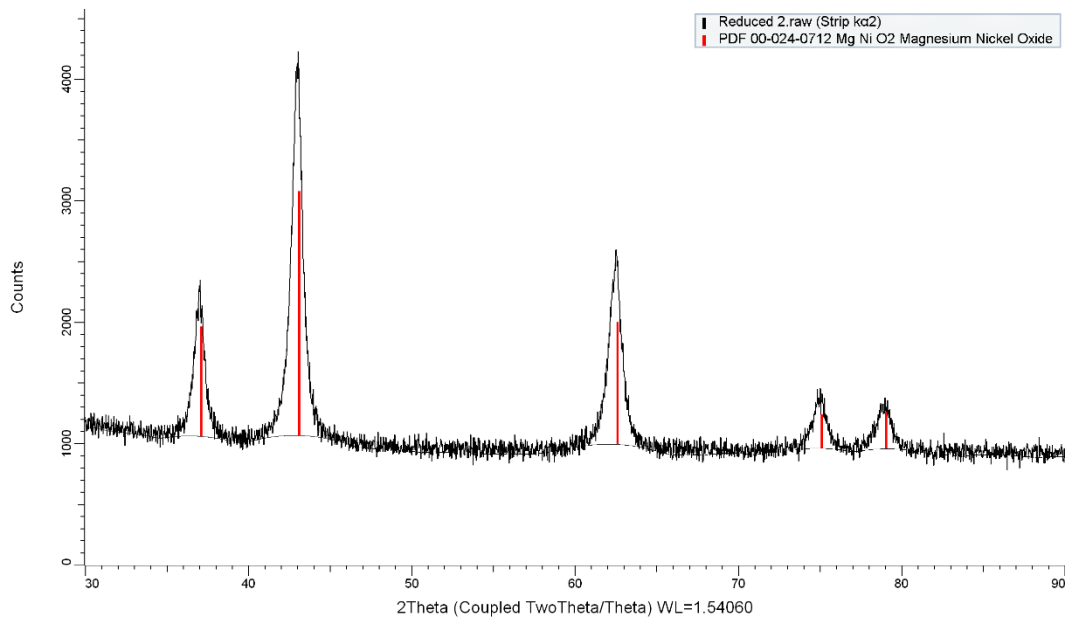


Figure B. 5 XRD pattern for black powder showing reduced or oxygen depleted state with peak location of the 50:50 NiO:MgO powder measuring a slight 2θ shift compared to Figure B. 3 the stoichiometric state.

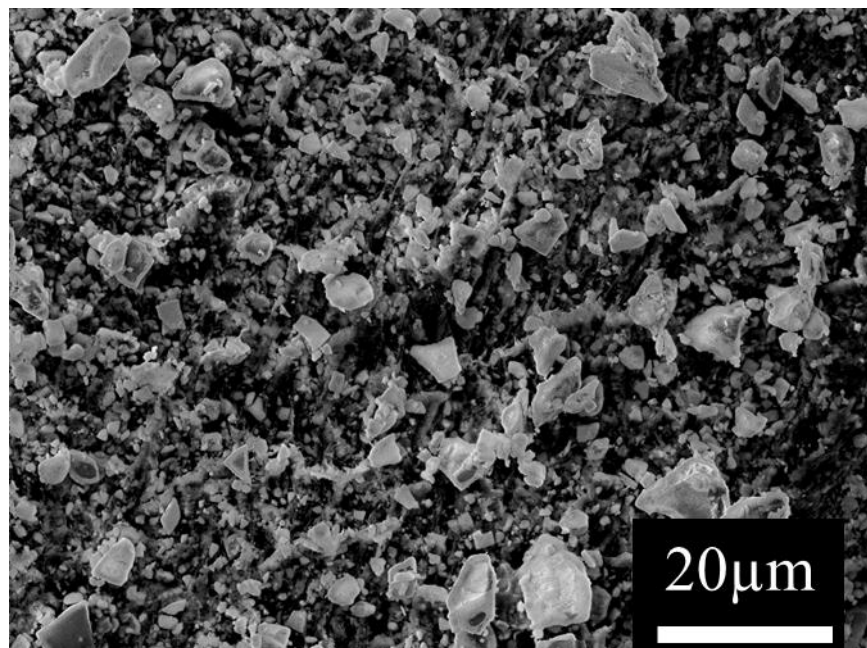


Figure B. 6 SEM image of 50:50 NiO:MgO powder in a reduced state exhibiting oxygen depletion. Corresponding XRD measured in Figure B. 5.

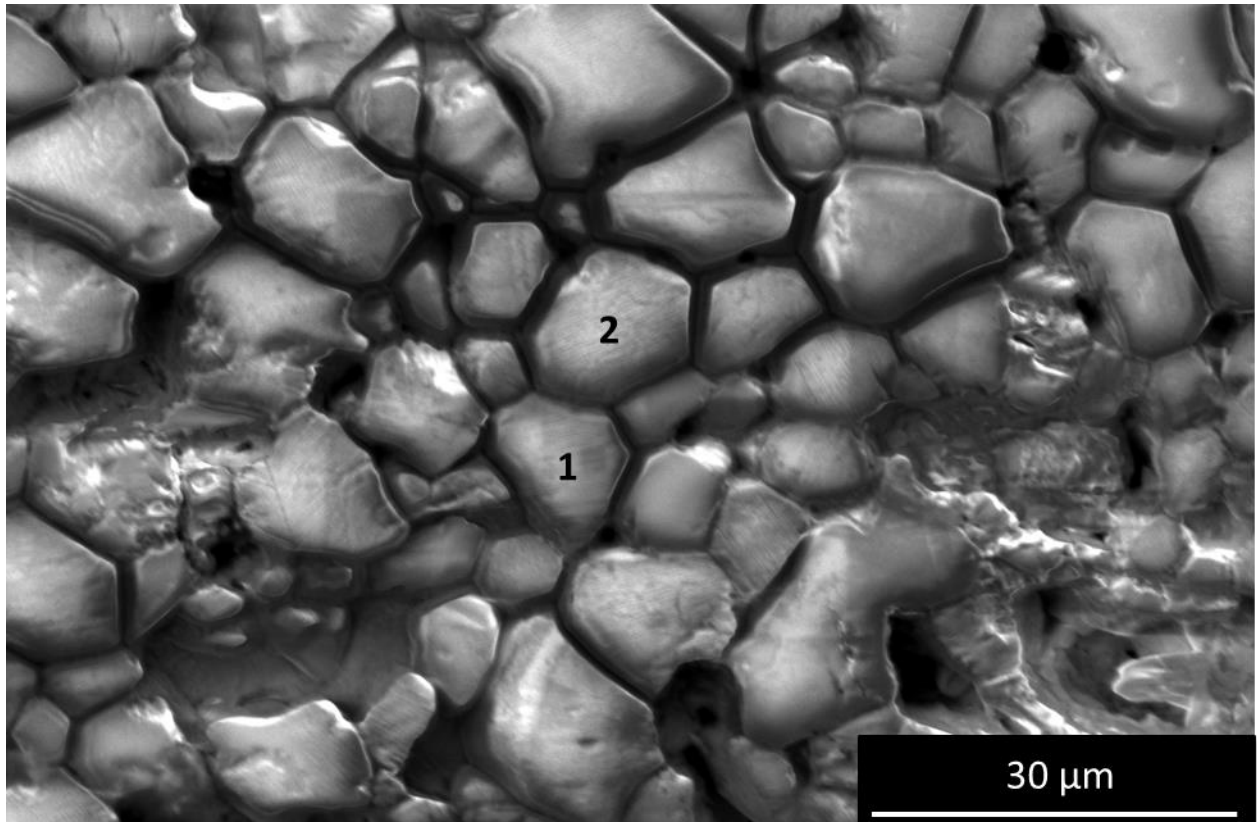


Figure B. 7 SEM image of 2 randomly selected grains discussed in Chapter 5 in relation to the determination of their crystallographic surface topography.

REFERENCES

- [1] Y. Chiang, D. P. Birnie, and W. D. Kingery, "Physical ceramics," New York: J. Wiley, 1997.
- [2] W. D. Callister, "(WCS)Materials Science and Engineering: An Introduction, 7th Edition Binder Ready Version," John Wiley & Sons Canada, Limited, 2007.
- [3] P. B. Vandiver, O. Soffer, B. Klima, and J. Svoboda, "The Origins of Ceramic Technology at Dolni Věstonice, Czechoslovakia," *Science* (80-.), vol. 246, no. 4933, pp. 1002–1008, 1989.
- [4] X. Wu, C. Zhang, P. Goldberg, D. Cohen, Y. Pan, T. Arpin, and O. Bar-Yosef, "Early pottery at 20,000 years ago in Xianrendong Cave, China," *Science*, vol. 336, no. 6089, 2012.
- [5] G. D. Hatton, A. J. Shortland, and M. S. Tite, "The production technology of Egyptian blue and green frits from second millennium BC Egypt and Mesopotamia," *J. Archaeol. Sci.*, vol. 35, no. 6, pp. 1591–1604, 2008.
- [6] S. PIERSON, "The Movement of Chinese Ceramics: Appropriation in Global History," *J. World Hist.*, vol. 23, no. 1, pp. 9–39, 2012.
- [7] K. Sugita, "Historical Overview of Refractory Technology in the Steel Industry," *Nippon Steel Tech. Rep.*, no. 98, pp. 8–17, 2008.
- [8] J. H. Tod, "A History of the Electrical Porcelain Industry in the United States," Tod, 1977.
- [9] "Brief History of Ceramics and Glass | The American Ceramic Society." [Online]. Available: <https://ceramics.org/about/what-are-engineered-ceramics-and-glass/brief-history-of-ceramics-and-glass>. [Accessed: 19-Nov-2018].
- [10] P. Yang and J.-M. Tarascon, "Towards systems materials engineering," *Nat. Mater.*, vol. 11, p. 560, Jun. 2012.
- [11] A. P. Sutton and R. W. Balluffi, "Interfaces in crystalline materials," Clarendon Press, 1995.
- [12] M. Bäurer, H. Störmer, D. Gerthsen, and M. J. Hoffmann, "Linking Grain Boundaries and Grain Growth in Ceramics," *Adv. Eng. Mater.*, vol. 12, no. 12, pp. 1230–1234, 2010.
- [13] E. Rabkin, "Effect of grain boundary faceting on kinetics of grain growth and microstructure evolution," *J. Mater. Sci.*, vol. 40, no. 4, pp. 875–879, Feb. 2005.

- [14] "Raw Materials of Ceramics," in *Advanced Ceramic Technologies & Products*, Tokyo: Springer Japan, 2012, pp. 15–16.
- [15] G. Huebner, "Natural and synthetic raw materials for technical ceramics," *Eur. J. Mineral.*, vol. 3, no. 4, pp. 651–665, Aug. 1991.
- [16] U. S. B. of Standards, "Fire-clay brick: their manufacture, properties, uses and specifications," Government Printing Office, 1926.
- [17] V. Orbovic and Z. Huang, "Kaolinite: Occurrences, Characteristics, and Applications," Nova Science Publishers, 2012.
- [18] H. H. Sortwell, "American and English ball clays," Govt. Print. Off., 1923.
- [19] M. Bengisu, "Engineering Ceramics. Springer," 2001.
- [20] "Dry Pressing Method." [Online]. Available: <http://www.capa-ceramic.com/dry.asp>. [Accessed: 19-Nov-2018].
- [21] B. C. Mutsuddy and R. G. Ford, "Ceramic Injection Molding," Springer US, 1994.
- [22] "Methods of shape forming ceramic powders [SubsTech]." [Online]. Available: http://www.substech.com/dokuwiki/doku.php?id=methods_of_shape_forming_ceramic_powers. [Accessed: 19-Nov-2018].
- [23] S. Wardell, "Slipcasting," University of Pennsylvania Press, Incorporated, 2007.
- [24] R. E. Mistler and E. R. Twiname, "Tape Casting: Theory and Practice," Wiley, 2000.
- [25] C. Suciú and A. Vik, "B0315 Tape Casting of Lanthanum Chromite," no. July, 2016.
- [26] T. A. Ring, "Fundamentals of Ceramic Powder Processing and Synthesis," Elsevier Science, 1996.
- [27] "1: Injection & Extrusion | School of Materials Science and Engineering." [Online]. Available: <http://www.materials.unsw.edu.au/tutorials/online-tutorials/1-injection-extrusion>. [Accessed: 19-Nov-2018].
- [28] S. J. L. Kang, "Sintering: Densification, Grain Growth and Microstructure," Elsevier Science, 2004.
- [29] M. N. Rahaman, "Ceramic Processing and Sintering," Taylor & Francis, 2003.
- [30] P. C. Angelo and R. Subramanian, "Powder metallurgy: science, technology and applications," PHI Learning, 2008.
- [31] R. German, "Sintering: From Empirical Observations to Scientific Principles," Elsevier Science, 2014.

- [32] V. A. Invenso, "Densification of Metal Powders During Sintering," Springer US, 2012.
- [33] I. Gibson and D. Shi, "Material properties and fabrication parameters in selective laser sintering process," *Rapid Prototyp. journal.*, vol. 3, no. 4, pp. 129–136, 1997.
- [34] H. Masuda, K. Higashitani, and H. Yoshida, *Powder Technology Handbook*. CRC Press, 2006.
- [35] W. B. Pietsch, "Agglomeration Processes: Phenomena, Technologies, Equipment," Wiley, 2008.
- [36] H. Mehrer, "Diffusion in Solids: Fundamentals, Methods, Materials, Diffusion-Controlled Processes," Springer Berlin Heidelberg, 2007.
- [37] *Sintering Technology*. Taylor & Francis, 1996.
- [38] A. Vondrous, "Grain growth behavior and efficient large scale simulations of recrystallization with the phase-field method," KIT Scientific Publishing, 2014.
- [39] M. Shirdel, H. Mirzadeh, and M. H. Parsa, "Abnormal grain growth in AISI 304L stainless steel," *Mater. Charact.*, vol. 97, pp. 11–17, 2014.
- [40] P. R. Cantwell, M. Tang, S. J. Dillon, J. Luo, G. S. Rohrer, and M. P. Harmer, "Grain boundary complexions," *Acta Mater.*, vol. 62, pp. 1–48, Jan. 2014.
- [41] S. M. An, B. K. Yoon, S. Y. Chung, and S. J. L. Kang, "Nonlinear driving force-velocity relationship for the migration of faceted boundaries," *Acta Mater.*, vol. 60, no. 11, pp. 4531–4539, 2012.
- [42] G. Anand and P. P. Chattopadhyay, "Computational Design of Microstructure," no. June. 2016.
- [43] E. J. Mittemeijer, "Fundamentals of Materials Science: The Microstructure–Property Relationship Using Metals as Model Systems," Springer Berlin Heidelberg, 2010.
- [44] G. S. Rohrer, "Grain boundary energy anisotropy: A review," *J. Mater. Sci.*, vol. 46, no. 18, pp. 5881–5895, 2011.
- [45] P. M. Anderson, J. P. Hirth, and J. Lothe, "Theory of Dislocations," Cambridge University Press, 2017.
- [46] R. W. Cahn and P. Haasen, *Physical Metallurgy*, no. v. 1. Elsevier Science, 1996.
- [47] D. Turnbull, "Theory of grain boundary migration rates," *J. Met.*, vol. 3, 1951.
- [48] J. W. Cahn, "The impurity-drag effect in grain boundary motion," *Acta Metall.*, vol. 10, no. 9, pp. 789–798, 1962.

- [49] J. D. Powers and A. M. Glaeser, "Grain Boundary Migration in Ceramics," *Interface Sci.*, vol. 6, no. 1, pp. 23–39, Feb. 1998.
- [50] C. H. Hsueh, A. G. Evans, and R. L. Coble, "Microstructure development during final/intermediate stage sintering—I. Pore/grain boundary separation," *Acta Metall.*, vol. 30, no. 7, pp. 1269–1279, Jul. 1982.
- [51] H. Sternlicht, W. Rheinheimer, M. J. Hoffmann, and W. D. Kaplan, "The mechanism of grain boundary motion in SrTiO₃," *J. Mater. Sci.*, vol. 51, no. 1, pp. 467–475, 2015.
- [52] B. Lee and S. Chung, "Grain boundary faceting and abnormal grain growth in BaTiO₃," vol. 48, pp. 1575–1580, 2000.
- [53] W. Rheinheimer, M. B??urer, C. A. Handwerker, J. E. Blendell, and M. J. Hoffmann, "Growth of single crystalline seeds into polycrystalline strontium titanate: Anisotropy of the mobility, intrinsic drag effects and kinetic shape of grain boundaries," *Acta Mater.*, vol. 95, pp. 111–123, 2015.
- [54] J. W. Cahn and C. A. Handwerker, "Equilibrium geometries of anisotropic surfaces and interfaces," *Mater. Sci. Eng. A*, vol. 162, no. 1–2, pp. 83–95, 1993.
- [55] J. E. Blendell, W. C. Carter, and C. a Handwerker, "Faceting and wetting transitions of anisotropic interfaces and grain boundaries," *J. Am. Ceram. Soc.*, vol. 82, no. 7, pp. 1889–1900, 1999.
- [56] B. B. Straumal, O. A. Kogtenkova, A. S. Gornakova, V. G. Sursaeva, and B. Baretzky, "Review: grain boundary faceting–roughening phenomena," *J. Mater. Sci.*, vol. 51, no. 1, pp. 382–404, 2015.
- [57] J. Li, S. J. Dillon, and G. S. Rohrer, "Relative grain boundary area and energy distributions in nickel," *Acta Mater.*, vol. 57, no. 14, pp. 4304–4311, Aug. 2009.
- [58] D. M. Saylor and G. S. Rohrer, "Evaluating Anisotropic Surface Energies Using the Capillarity Vector Reconstruction Method," *Interface Sci.*, vol. 9, no. 1, pp. 35–42, Apr. 2001.
- [59] G. S. Rohrer and V. Randle, "Measurement of the five-parameter grain boundary distribution from planar sections," *Electron Backscatter Diffr. Mater. Sci.*, pp. 215–229, 2009.

- [60] C. Handwerker, M. Vaudin, and J. Blendell, "Equilibrium Crystal Shapes and Surface Phase Diagrams at Surfaces in Ceramics," *Interface Sci. Eng. '87; Lake Placid, New York; USA; 13-16 July 1987*, 1987.
- [61] D. R. Dinger and J. E. Funk, "Particle-Packing Phenomena and Their Application in Materials Processing," *MRS Bull.*, vol. 22, no. 12, pp. 19–23, Dec. 1997.
- [62] C. Suryanarayana, "Mechanical alloying and milling," *Mater. Sci.*, vol. 46, pp. 1–184, 2001.
- [63] C. Suryanarayana, *Mechanical alloying and milling*. Marcel Dekker, 2004.
- [64] C. Marcilly, P. Cqurty, and B. Delmqn, "Preparation of Highly Dispersed Mixed Oxides and Oxide Solid Solutions by Pyrolysis of Amorphous Organic Precursors," vol. 53, no. 1, pp. 56–57, 2000.
- [65] M. Serra, P. Salagre, Y. Cesteros, F. Medina, and J. E. Sueiras, "Study of preparation conditions of NiO – MgO systems to control the morphology and particle size of the NiO phase," vol. 134, pp. 229–239, 2000.
- [66] R. Zanganeh, M. Rezaei, and A. Zamaniyan, "Preparation of nanocrystalline NiO-MgO solid solution powders as catalyst for methane reforming with carbon dioxide: Effect of preparation conditions," *Adv. Powder Technol.*, vol. 25, no. 3, pp. 1111–1117, 2014.
- [67] M. Serra, P. Salagre, and Y. Cesteros, "Design of NiO–MgO materials with different properties," *Pccp*, no. 3, pp. 858–864, 2004.
- [68] A. Renaud, B. Chavillon, L. Cario, L. Le Pleux, N. Szuwarski, Y. Pellegrin, E. Blart, E. Gautron, F. Odobel, and S. Jobic, "Origin of the black color of NiO used as photocathode in p-type dye-sensitized solar cells," *J. Phys. Chem. C*, vol. 117, no. 44, pp. 22478–22483, 2013.
- [69] A. L. Patterson, "The Scherrer Formula for X-Ray Particle Size Determination," vol. 56, pp. 978–982, 1939.
- [70] T. Chiba, "A : Ni-MgO catalyst prepared by using a melt of the nitrates and citric acid," pp. 2–5, 1996.
- [71] T. Nakayama, N. Ichikuni, S. Sato, and F. Nozaki, "Ni/Mgo catalyst prepared using citric acid for hydrogenation of carbon dioxide," *Appl. Catal. A Gen.*, vol. 158, no. 1–2, pp. 185–199, 1997.

- [72] R. Chaim, M. Levin, a. Shlayer, and C. Estournes, "Sintering and densification of nanocrystalline ceramic oxide powders: a review," *Adv. Appl. Ceram.*, vol. 107, no. 3, pp. 159–169, 2008.
- [73] J. Ma and L. C. Lim, "Effect of particle size distribution on sintering of agglomerate-free submicron alumina powder compacts," *J. Eur. Ceram. Soc.*, vol. 22, no. 13, pp. 2197–2208, Dec. 2002.
- [74] M. J. Mayo, "Processing of nanocrystalline ceramics from ultrafine particles," *Int. Mater. Rev.*, vol. 41, no. 3, pp. 85–115, Jan. 1996.
- [75] N. Saheb, Z. Iqbal, A. Khalil, A. S. Hakeem, N. Al Aqeeli, T. Laoui, A. Al-Qutub, and R. Kirchner, "Spark Plasma Sintering of Metals and Metal Matrix Nanocomposites: A Review," *J. Nanomater.*, vol. 2012, pp. 1–13, 2012.
- [76] J. Cahn and W. Carter, "Crystal shapes and phase equilibria: A common mathematical basis," *Metall. Mater. Trans. A*, vol. 27, no. 6, pp. 1431–1440, 1996.
- [77] "Handwerker Blendell Vaudin J Physique.pdf." .